Assembly and phospho-regulatory mechanisms of the budding yeast outer kinetochore KMN complex

Noah N. Turner[1,2,3], Ziguo Zhang[1], Kyle W. Muir[1,2], Stephen H. McLaughlin[1], Tomos Morgan[1] and David Barford[1,3]

[1]MRC Laboratory of Molecular Biology, Francis Crick Avenue, Cambridge, CB2 0QH, UK.

[2]Present address: Noah N. Turner: John Innes Centre, Norwich, UK; Kyle W. Muir: Institute of Cell Biology, University of Edinburgh, Edinburgh, EH9 3BF, UK.

[3]Corresponding authors: nturner@lmb-mrc.cam.ac.uk, dbarford@mrc-lmb.cam.ac.uk

Running title: Cryo-EM structure of the budding yeast KMN complex

40 word summary: Kinetochore-localised KMN complexes mediate chromosome segregation by attaching chromosomes to spindle microtubules. Cryo-EM, biochemical and genetic experiments reveal conserved underlying mechanisms of complex assembly, auto-inhibition and phospho-regulation that ensure precise control of KMN assembly onto centromeres to enable genome division.

Abstract

During mitosis and meiosis kinetochores mediate interactions between chromosomes and spindle microtubules. Kinetochores are multi-megadalton protein complexes essential for chromosome segregation in all eukaryotes, however recent structural, functional, and evolutionary studies have revealed divergent mechanisms of kinetochore assembly. In this study, we use cryo-EM to understand the structural mechanisms by which the budding yeast microtubule-binding outer kinetochore KMN complex assembles, and how its interactions with the centromere-binding inner kinetochore are regulated. The ten-subunit KMN complex comprises three subcomplexes: Knl1c, Mis12c^{Mtw1c} and Ndc80c. We show that α-helical motifs in the C-termini of the Mis12c^{Mtw1c} subunits Dsn1, Mis12^{Mtw1} and Pmf1^{Nnf1} bind Knl1c and Ndc80c. At the opposite end of the Mis12c^{Mtw1c} stalk, an N-terminal auto-inhibitory segment of Dsn1 (Dsn1^{AI}) folds into two α-helices that engage its head 1 domain, thereby occluding binding sites for the inner kinetochore subunits CENP-C^{Mif2} and CENP-U^{Ame1}, reducing their affinity for Mis12c^{Mtw1}. Our structure reveals how Aurora B^{Ipl1}

phosphorylation of Dsn1^{AI} would release this auto-inhibition to substantially strengthen pre-existing connections between the inner and outer kinetochore.

Introduction

Eukaryotes have evolved kinetochores, multi-megadalton nucleoprotein complexes, to mediate faithful chromosome segregation during cell division (Ariyoshi and Fukagawa, 2023; McAinsh and Marston, 2022; Musacchio and Desai, 2017). Kinetochores assemble at centromeres to create an essential load-bearing linkage between chromosomes and microtubules of the mitotic spindle (Akiyoshi et al., 2010; Lang et al., 2018). The budding yeast *Saccharomyces cerevisiae* is a model organism with genetically defined point centromeres. *CEN* sequences of ~118 bp define centromeric identity through three centromere DNA elements (CDEI-III) (Clarke and Carbon, 1980; Clarke and Carbon, 1983; Fitzgerald-Hayes et al., 1982; Hyman and Sorger, 1995). The *CEN* sequence and CENP-A^{Cse4} nucleosome together provide a foundation upon which the rest of the kinetochore assembles (Lang et al., 2018). The CENP-C^{Mif2} protein mediates specific interactions between the CENP-A nucleosome and the inner kinetochore constitutive centromere associated network (CCAN) complex, and also interacts with the outer kinetochore KMN complex (Ariyoshi et al., 2021; Dimitrova et al., 2016; Hornung et al., 2014; Kato et al., 2013; Przewloka et al., 2011; Screpanti et al., 2011; Xiao et al., 2017; Yan et al., 2019). CCAN complexes entrap centromeric DNA within topological chambers (Dendooven et al., 2023; Yatskevich et al., 2022).

The outer kinetochore KMN complex bridges the inner kinetochore with the microtubule (Cheeseman et al., 2006; Deluca et al., 2006). Mis12c/Mis12c^{Mtw1c} (human/budding yeast) interacts with Knl1c and Ndc80c to assemble the KMN complex (Figure S1A) and mediates recruitment of the entire complex to kinetochores (Dimitrova et al., 2016; Ghodgaonkar-Steger et al., 2020; Petrovic et al., 2014; Petrovic et al., 2010; Polley et al., 2024; Yatskevich et al., 2024). Ndc80c also associates with CENP-T independently of Mis12c^{Mtw1c} and Knl1c (Malvezzi et al., 2013; Nishino et al., 2013). Mis12c engages Knl1c and Ndc80c at the apex of a central α-helical stalk (Petrovic et al., 2014). The base of the stalk bifurcates to form the head 1 and head 2 domains that mediate Aurora B^{Ipl1}-dependent interactions with the inner kinetochore (Akiyoshi et al., 2013; Dimitrova et al., 2016; Emanuele et al., 2008; Kim and Yu, 2015; Petrovic et al., 2016; Rago et al., 2015; Walstein et al., 2021). Head 1 interacts with N-terminal motifs of CENP-C^{Mif2} and CENP-U^{Ame1} in budding yeast, and CENP-C^{Mif2} and

CENP-T in vertebrates (Dimitrova et al., 2016; Hornung et al., 2014; Huis In 'T Veld et al., 2016; Killinger et al., 2020; Petrovic et al., 2016). The mutually exclusive competitive binding of inner kinetochore subunits to Mis12c^{Mtw1c} (Huis In 'T Veld et al., 2016; Killinger et al., 2020) recruits multiple copies of KMN to the inner kinetochore (Cieslinski et al., 2023; Dhatchinamoorthy et al., 2017; Joglekar et al., 2006; Johnston et al., 2010). These interactions are auto-inhibited by a region within the intrinsically disordered N-terminal region of the Mis12c^{Mtw1c} subunit Dsn1 in a manner that is relieved by Aurora B^{Ipl1} phosphorylation at mitotic kinetochores (Dimitrova et al., 2016; Petrovic et al., 2016; Polley et al., 2024; Takenoshita et al., 2024; Walstein et al., 2021; Yatskevich et al., 2024).

Ndc80c interacts with the microtubule lattice through N-terminal domains of its constituent Ndc80 and Nuf2 subunits (Alushin et al., 2012; Alushin et al., 2010; Ciferri et al., 2008; Lampert et al., 2013; Muir et al., 2023; Wei et al., 2007). Ndc80c-mediated attachments to microtubule tips are augmented through interactions with the evolutionarily unrelated Astrin/SKAP and Ska complexes in human and the Dam1 complex in budding yeast (Helgeson et al., 2018; Huis In 'T Veld et al., 2019; Kern et al., 2017; Lampert et al., 2010; Muir et al., 2023; Tien et al., 2010; Van Hooff et al., 2017). The Ndc80 and Nuf2 microtubule-binding calponin homology (CH) domains are at the opposite end of the 570 Å-long Ndc80 complex to RWD domains in the C-termini of the Spc24 and Spc25 subunits (Spc24^{RWD}:Spc25^{RWD}) that interact with Mis12c^{Mtw1c} (Wang et al., 2008; Wei et al., 2006; Wei et al., 2005). The long Ndc80c is formed by the end on interactions of the Ndc80:Nuf2 and Spc24:Spc25 coiled-coils (Ciferri et al., 2005; Valverde et al., 2016). Kinetochore-associated Knl1c contributes to spindle assembly checkpoint (SAC) and error correction (EC) signalling through motifs that are arrayed throughout the Knl1^{Spc105} N-terminal region. MELT motifs in Knl1^{Spc105} phosphorylated by Mps1 kinase interact directly with Bub1:Bub3 of the SAC machinery. This controls chromosome alignment, chromosome biorientation and SAC signalling (reviewed in (Fischer, 2023; McAinsh and Kops, 2023)).

Although the general mechanisms of KMN complex assembly and regulation are conserved from budding yeast to human, specific details of how Mis12c^{Mtw1c} interacts with both Ndc80c and Knl1c differ. The Spc24:Spc25 RWD domains of Ndc80c interact with α-helical motifs in C-terminal extensions of the rod-like stalk domain of human Mis12c and budding yeast Mis12c^{Mtw1c}. These include a conserved α-helix in the Dsn1 subunit (Dimitrova et al., 2016; Polley et al., 2024; Yatskevich et al., 2024), and, additionally in humans, an α-helix in the Mis12c subunit Nsl1 (Polley et al., 2024; Yatskevich et al., 2024). No equivalent motif exists

96 in budding yeast Nsl1 (Dimitrova et al., 2016). Instead, an α-helix in the budding yeast
97 Mis12c^{Mtw1c} subunit Mis12^{Mtw1} binds to the Spc24 and Spc25 RWD domains cooperatively
98 with the Dsn1 α-helix (Ghodgaonkar-Steger et al., 2020). In humans, a motif at the extreme
99 C-terminus of Nsl1 mediates binding of Mis12c to the tandem C-terminal RWD domains of
100 the human Knl1c subunit Knl1 (Kiyomitsu et al., 2007; Petrovic et al., 2016; Petrovic et al.,
101 2014; Polley et al., 2024; Yatskevich et al., 2024). The orthologous budding yeast protein
102 Knl1^{Spc105} also uses tandem C-terminal RWD domains to interact with Mis12c^{Mtw1c} (Maskell
103 et al., 2010), although the regions of Mis12c^{Mtw1c} that interact with yeast Knl1c are largely
104 uncharacterised. Likewise, due to sequence differences between human and budding yeast
105 Dsn1, the structural basis of Mis12c^{Mtw1c} auto-inhibition by an N-terminal region of Dsn1,
106 and its relief by Aurora B^{Ipl1} phosphorylation (Akiyoshi et al., 2013; Kim and Yu, 2015; Yang
107 et al., 2008) is unclear. To understand these differences, we determined cryo-EM structures of
108 the *S. cerevisiae* KMN complex. The structure reveals that interactions between the three
109 KMN sub-complexes are mediated by α-helical motifs in the C-termini of the Mis12c^{Mtw1c}
110 subunits Dsn1, Mis12^{Mtw1} and Pmf1^{Nnf1}, which engage interfaces on Knl1c and Ndc80c. Our
111 work shows that a combination of conserved and plastic interfaces, divergent at the sequence
112 and subunit level, underpin a nevertheless comparable overall KMN complex architecture
113 between point and regional centromeres. Furthermore, our work reveals that Aurora B^{Ipl1}
114 overcomes auto-inhibition of human Mis12c and budding yeast Mis12c^{Mtw1c} through similar
115 structural mechanisms.

116 **Results**

117 Structural features of the budding yeast KMN complex

118 To determine the cryo-EM structure of the *S. cerevisiae* KMN complex, we purified Ndc80c
119 and a Knl1c:Mis12c^{Mtw1c} complex (K^{HB-RWD}M) from insect cells (Figure S1A, B). K^{HB-RWD}M
120 comprised a truncated Knl1^{Spc105} subunit (Knl1$^{Spc105_HB-RWD}$) that incorporated its helical
121 bundle and tandem RWD domains but had a deleted N-terminal disordered region (retaining
122 residues 445-917). Protein band intensities on SDS-PAGE gels (Figure S1B) and SEC-MALS
123 analysis (data not shown) showed that the purified K^{HB-RWD}M contained one subunit of each
124 of Knl1$^{Spc105_HB-RWD}$ and ZWINT^{Kre28}. A previous study suggested a stoichiometry for Knl1c
125 of one Knl1^{Spc105} subunit and two ZWINT^{Kre28} subunits on the basis of analytical
126 ultracentrifugation and immunoprecipitation experiments (Pagliuca et al., 2009). However,
127 the stoichiometry of our recombinant Knl1c is consistent with the number of Knl1^{Spc105} and

ZWINT^{Kre28} proteins counted at kinetochores in cells, using intensity measurements of fluorescently tagged proteins (Roy et al., 2022).

We pursued numerous strategies to reconstitute and stabilise KMN on cryo-EM grids, with the best results obtained using the GraFix methodology (Stark, 2010). A ten-subunit KMN complex (Figure 1A) was reconstituted by incubating K^{HB-RWD}M and Ndc80c (Figure S1C, D) at an equimolar ratio. K^{HB-RWD}MN complex formation was indicated by the co-migration in a glycerol gradient of its ten subunits in a stoichiometric ratio, separate from K^{HB-RWD}M and Ndc80c (Figure S1E). The reconstituted K^{HB-RWD}MN (henceforth KMN) was crosslinked and purified using a 10-30% glycerol gradient with 0.0-0.2% glutaraldehyde (Figure S1F). We prepared grids and collected a large cryo-EM dataset on this sample. Cryo-electron micrographs and 2D class averages revealed elongated particles (Figure S2A, B) that corresponded closely with the previously observed structures of isolated Mis12c^{Mtw1c}, Mis12c and Ndc80c, the entire human KMN complex, and negative-staining EM of the budding yeast KMN complex (Ciferri et al., 2008; Dudziak et al., 2024; Hornung et al., 2011; Maskell et al., 2010; Petrovic et al., 2014; Petrovic et al., 2010; Polley et al., 2024; Wang et al., 2008; Wei et al., 2005; Yatskevich et al., 2024). We determined medium-resolution cryo-EM maps of a KMN junction complex that contained the stalk and head 1 domains of Mis12c^{Mtw1c}, and the RWD domains of Knl1c and Ndc80c (Figure S2Di and Table S1).

The limited resolution (6.5 Å) of the consensus structure of the KMN junction complex was likely caused by heterogeneity at either end of the Mis12c^{Mtw1c} stalk domain (Figure S2Di) that we were unable to resolve with extensive 2D and 3D classification and 3D variability analyses. To obtain a higher-resolution structure of subdomains, we subtracted the signal arising from the poorly resolved Mis12c^{Mtw1c} head 2 domain (Figure S2Dii) and subjected the subtracted particles to multibody refinement using masks encompassing the two domains forming the apex and base of the Mis12c^{Mtw1c} stalk domain (Figure S2Diii). This yielded reconstructions showing the Knl1c and Spc24:Spc25 RWD domains at the apex of the Mis12c^{Mtw1c} stalk, and head 1 at the base of the Mis12c^{Mtw1c} stalk, at global resolutions of 4.8 Å and 4.9 Å, respectively (Figure S2Diii). The local resolutions of the reconstructions reached 4.2 Å and 4.5 Å in the central regions of the apex and base density maps, respectively (Figure S2E, F), which were sufficient to interpret with an AlphaFold2 (AF2)-predicted model (Jumper et al., 2021). To obtain a composite map of the KMN junction complex, we docked the cryo-EM maps of the apex and base multi-bodies into the consensus cryo-EM map (Figure 1B). This composite map was used to build a model of the *S. cerevisiae*

KMN junction complex using AF2 structure predictions and Isolde model refinement, as detailed in Methods (Croll, 2018; Jumper et al., 2021).

Overall, the *S. cerevisiae* KMN junction complex architecture (Figure 1B, C and Video S1) (schematic in Figure 1D) resembles the human KMN complex (Polley et al., 2024; Yatskevich et al., 2024). The Mis12c^{Mtw1c} structure is dominated by an α-helical bundle assembled from its four subunits that form a central stalk. This Mis12c^{Mtw1c} stalk domain comprises three coiled-coil (CC) regions (CC1, CC2 and CC3) (Dimitrova et al., 2016). Similar to human KMN, the Knl1c and Spc24:Spc25 RWD domains are bound at the apex of the Mis12c^{Mtw1c} stalk, and although in close proximity, are not in direct contact. The Mis12c^{Mtw1c} head 1 domain, comprising a short four α-helical bundle formed from the Mis12^{Mtw1} and Pmf1^{Nnf1} subunits, is attached to the base of the stalk domain through loops, docking against Dsn1 and Nsl1 of the CC1 region (Figure 1B, C). In the composite cryo-EM map of the *S. cerevisiae* KMN junction complex, no density was observed for portions of Ndc80c comprising the Spc24:Spc25 coiled-coils and the entire Ndc80:Nuf2 subcomplex. Likewise, for Knl1c, all regions preceding the C-terminal RWD domains of Knl1^{Spc105} and ZWINT^{Kre28} were not visible. Disorder of both the Ndc80c and Knl1c subcomplexes in *S. cerevisiae* KMN, indicative of their conformational flexibility, was also observed in the human KMN structure (Polley et al., 2024; Yatskevich et al., 2024).

Our structure of *S. cerevisiae* KMN also revealed important differences with the human KMN complex, specifically in how Mis12c^{Mtw1c} interacts with both Knl1c and Ndc80c, and the presence of a C-terminal RWD domain in ZWINT^{Kre28} (ZWINT^{Kre28_RWD}) that is absent from the human ortholog (Figure 1B, C). An RWD domain in *S. cerevisiae* ZWINT^{Kre28} had previously been predicted on the basis of phylogenetic analyses and AF2 models (Polley et al., 2024; Tromer et al., 2019). In *S. cerevisiae* KMN, ZWINT^{Kre28_RWD} interacts with the N-terminal RWD domain of Knl1^{Spc105}, a role played by the ZWINT C-terminal α-helix in human Knl1 (Yatskevich et al., 2024). Lastly, in this reconstruction of the *S. cerevisiae* KMN junction complex, cryo-EM density for the Mis12c^{Mtw1c} head 2 domain is not visible due to the subtraction of head 2 cryo-EM density for cryo-EM data processing.

<u>Interactions of Mis12c^{Mtw1c} with Knl1c and Ndc80c and comparison with human KMN</u>

Mis12c^{Mtw1c} contacts Knl1c through the Dsn1:Pmf1^{Nnf1} CC3 coiled-coil and a peptidic extension of Mis12^{Mtw1}

192 The Dsn1, Mis12^{Mtw1} and Pmf1^{Nnf1} subunits mediate Mis12c^{Mtw1c} interactions at two contact
193 sites on Knl1c. First, conserved aliphatic residues in Dsn1 and the C-terminal α-helix of
194 Pmf1^{Nnf1} (Pmf1$^{Nnf1_Cterm\text{-}helix}$), part of the Mis12c^{Mtw1c} CC3 region, engage a hydrophobic
195 patch on the C-terminal RWD domain of Knl1^{Spc105} (Knl1$^{Spc105_RWD\text{-}C}$) (Figures 1C, D and
196 2A-C and S3A and Video S1). In general, this *S. cerevisiae* Mis12c^{Mtw1c} – Knl1c interface
197 resembles its counterpart in human KMN (Polley et al., 2024; Yatskevich et al., 2024).

198 At the second Mis12c^{Mtw1c} – Knl1c contact site, which differs from human KMN (Polley et
199 al., 2024; Yatskevich et al., 2024), the extreme C-terminal α-helix of Mis12^{Mtw1} (residues
200 282-289: Mis12$^{Mtw1_Cterm\text{-}helix}$) engages a channel formed at the interface of the Knl1^{Spc105}
201 RWD-N domain (Knl1$^{Spc105_RWD\text{-}N}$) and an α-helix of ZWINT^{Kre28_RWD} (ZWINT$^{Kre28_\alpha1\text{-}helix}$)
202 (Figures 1C, D and 2A, B, D and S3B). The ZWINT$^{Kre28_\alpha1\text{-}helix}$ combines with
203 Knl1$^{Spc105_RWD\text{-}N}$ to create a hydrophobic channel that is ideally suited to bind the mixed
204 hydrophobic and acidic Mis12$^{Mtw1_Cterm\text{-}helix}$ (Figure 2D). Immediately preceding
205 Mis12$^{Mtw1_Cterm\text{-}helix}$, a β-strand from Mis12^{Mtw1} augments the β-sheet of Knl1$^{Spc105_RWD\text{-}N}$
206 (Figure 2B). In human KMN, ZWINT lacks an RWD domain, and Mis12 does not contact
207 Knl1c. Instead, the extreme C-terminus of Nsl1 contacts the Knl1$^{RWD\text{-}N}$:ZWINT interface and
208 ,additionally, a shallow groove on Knl1$^{RWD\text{-}N}$ (Petrovic et al., 2014; Polley et al., 2024;
209 Yatskevich et al., 2024). The latter interaction is not observed in *S. cerevisiae* KMN (Figure
210 2B). Our experimental structure of the Mis12^{Mtw1} – Knl1c interface is in strong agreement
211 with AF2 predictions of the Knl1c:Mis12c^{Mtw1c} complex (Figure S3C-E), supporting our
212 assignment of cryo-EM densities to Mis12$^{Mtw1_Cterm\text{-}helix}$ and Pmf1$^{Nnf1_Cterm\text{-}helix}$ (Figure S3A,
213 B).

214 Consistent with our structure, deletion of residues comprising and surrounding
215 Mis12$^{Mtw1_Cterm\text{-}helix}$ mildly reduced levels of Knl1^{Spc105} and ZWINT^{Kre28} that co-purified with
216 Mis12c^{Mtw1c} isolated from yeast (Ghodgaonkar-Steger et al., 2020). Indeed, we found that
217 deletion of either Mis12$^{Mtw1_Cterm\text{-}helix}$ or Pmf1$^{Nnf1_Cterm\text{-}helix}$ reduced the co-purification of
218 Mis12c^{Mtw1c} with Knl1c (C-terminal tag on ZWINT^{Kre28}) from insect cells (Figure 2E). These
219 deletions did not affect the stability nor assembly of Mis12c^{Mtw1c} (Figure S4A, B) nor its
220 interaction with Ndc80c (Figure S4C, D), suggesting that the specific functions of
221 Mis12$^{Mtw1_Cterm\text{-}helix}$ and Pmf1$^{Nnf1_Cterm\text{-}helix}$ are to mediate the interaction between Mis12c^{Mtw1c}
222 and Knl1c.

To investigate the function of Mis12$^{Mtw1_Cterm\text{-}helix}$ and Pmf1$^{Nnf1_Cterm\text{-}helix}$ *in vivo* we used the auxin inducible degron (AID) system (Tanaka et al., 2015). We constructed *S. cerevisiae* strains encoding the *Os*Tir1 ubiquitin ligase at the *URA3* locus and a mAID$_3$-FLAG$_5$ C-terminal tag at either the endogenous *NNF1* (encoding Pmf1^{Nnf1}) or *MTW1* (encoding Mis12^{Mtw1}) loci. This enabled depletion of the endogenous gene products by addition of indole acetic acid (IAA). We then tested the ability of the gene products encoded by wildtype *MTW1* and *NNF1* and mutant *mtw1* and *nnf1* alleles with their C-terminal α-helices deleted (*mtw1$^{\Delta C}$* and *nnf1$^{\Delta C}$*, respectively), integrated at an ectopic locus, to rescue the lethality conferred by depleting the endogenous gene product. Western blotting confirmed that the mAID$_3$-FLAG$_5$ tagged gene products of the endogenous *MTW1* and *NNF1* loci were depleted after addition of IAA (Figure S5A, B), and that the rescue alleles were expressed from the exogenous loci (Figure S5C, D). All strains grew well on YEPD plates in the absence of IAA, showing that the incorporation of the mAID$_3$-FLAG$_5$ tag at the endogenous *MTW1* and *NNF1* loci, and rescue alleles at the exogenous loci, did not adversely affect cell growth (Figure 2F). Consistent with the essentiality of the Mis12^{Mtw1} and Pmf1^{Nnf1} gene products (Euskirchen, 2002), strains that had an empty cassette incorporated at the exogenous locus were unable to grow on plates containing IAA (Figure 2F). The expression of wild type *MTW1* and *NNF1* rescue alleles rescued this lethality (Figure 2F). We also found that the *mtw1$^{\Delta C}$* and *nnf1$^{\Delta C}$* alleles rescued lethality caused by depletion of endogenous *MTW1* and *NNF1* at 30°C (Figure 2F), 37°C, and in the presence of various concentrations of the spindle poison benomyl (data not shown). Whilst unexpected given the essentiality of *SPC105* and *KRE28* genes (Nekrasov et al., 2003; Pagliuca et al., 2009; Wigge et al., 1998), these data are consistent with our own *in vitro* results which showed that deletion of either Mis12$^{Mtw1_Cterm\text{-}helix}$ or Pmf1$^{Nnf1_Cterm\text{-}helix}$ helices alone reduces, but does not abolish, co-purification of Mis12c^{Mtw1c} with Knl1c (Figure 2E).

Mis12c^{Mtw1c} contacts Ndc80c through the Dsn1:Nsl1 CC3 coiled-coil and peptidic extensions of Dsn1 and Mis12^{Mtw1}

In the *S. cerevisiae* KMN junction complex, Mis12c^{Mtw1c} engages Ndc80c through multiple contacts involving the RWD domains of Spc24 and Spc25 (Spc24^{RWD} and Spc25^{RWD}). These interactions comprise the CC3 region of the Mis12c^{Mtw1c} stalk, and peptidic C-terminal extensions of Dsn1 and Mis12^{Mtw1} (Figures 1C, D and 3A-D and S6A, B and Video S1). First, as similarly observed in human KMN (Polley et al., 2024; Yatskevich et al., 2024), the hydrophobic patch of the Spc24^{RWD} β-sheet interacts with hydrophobic residues of Dsn1 and

Nsl1 in CC3 (Figure 1C,D and 3A, B, C and S6A). Second, differing from human KMN, an α-helical segment of Mis12^{Mtw1} (Mis12$^{Mtw1_Spc24\text{-}helix}$) buttresses Spc24^{RWD} and the Spc24:Spc25 coiled-coil (Figures 1C, D and 3A, B, D and S6B), before Mis12^{Mtw1} crosses to contact Knl1c through Mis12$^{Mtw1_Cterm\text{-}helix}$. The interaction of Mis12$^{Mtw1_Spc24\text{-}helix}$ residues Tyr236 and Arg240 with Spc24^{RWD} and Spc25^{RWD} is supported by well-resolved cryo-EM density (Figures 3D and S6B). These interactions likely rationalise why Asp substitution of Mis12^{Mtw1} residues Arg233 and Tyr236 reduced levels of Spc24:Spc25 associated with Mis12c^{Mtw1c} in an *in vitro* assay, and sensitises yeast to benomyl (Ghodgaonkar-Steger et al., 2020). In human KMN, *S. cerevisiae* Mis12$^{Mtw1_Spc24\text{-}helix}$ is functionally replaced by a short α-helix of Nsl1 (Nsl1$^{Spc24\text{-}helix}$) that buttresses Spc24^{RWD} and the Spc24:Spc25 coiled-coil, before Nsl1 also crosses to contact Knl1c (Nsl1^{Cterm}) (Polley et al., 2024; Yatskevich et al., 2024).

Thirdly, in another interaction that is conserved with human KMN (Polley et al., 2024; Yatskevich et al., 2024) the C-terminal Dsn1 α-helix (residues 560-574: Dsn1$^{Cterm\text{-}helix}$) docks into a deep channel at the interface of Spc24^{RWD} and Spc25^{RWD} (Figures 1C, D, 3B, D and S6B). However, the budding yeast KMN complex differs from human in that the Mis12$^{Mtw1_Spc24\text{-}helix}$ stabilises this interaction. The four-turn Mis12$^{Mtw1_Spc24\text{-}helix}$ bridges both Dsn1$^{Cterm\text{-}helix}$ and Spc24^{RWD} through interactions mediated by Val244 and Leu245 of Mis12$^{Mtw1_Spc24\text{-}helix}$ (Figures 3D and S6B). The shorter human Nsl1$^{Spc24\text{-}helix}$ does not extend to contact the Dsn1$^{Cterm\text{-}helix}$ (Polley et al., 2024; Yatskevich et al., 2024). This interaction of budding yeast Dsn1$^{Cterm\text{-}helix}$ with Mis12$^{Mtw1_Spc24\text{-}helix}$ might be the basis by which Dsn1$^{Cterm\text{-}helix}$ and Mis12$^{Mtw1_Spc24\text{-}helix}$ bind to Spc24:Spc25 cooperatively. This interface could explain how Asp substitutions of Mis12^{Mtw1} Val244, together with Leu248, a residue not resolved in our structure, strongly impaired binding of Spc24:Spc25 and Mis12c^{Mtw1c} *in vitro*, and confers benomyl sensitivity *in vivo* (Ghodgaonkar-Steger et al., 2020).

Lastly, our structure of Mis12$^{Mtw1_Spc24\text{-}helix}$ and Dsn1$^{Cterm\text{-}helix}$ bound to Spc24^{RWD}:Spc25^{RWD} agrees with crystal structures of the Spc24^{RWD}:Spc25^{RWD}:Dsn1$^{Cterm\text{-}helix}$ complex (Figure S6C) (Dimitrova et al., 2016), and AF2 predictions of Mis12c^{Mtw1c} with Spc24 and Spc25 (Figure S6D, E).

Mechanism of Mis12c^{Mtw1c} auto-inhibition and activation by Aurora B^{Ipl1} kinase

An auto-inhibitory segment of Dsn1 engages the head 1 lobe of Mis12c^{Mtw1c}

287 The Dsn1 N-terminal intrinsically disordered region (N-IDR), situated immediately N-
288 terminal of head 2, auto-inhibits the interaction of Mis12c^{Mtw1c} with the inner kinetochore
289 (Dimitrova et al., 2016; Petrovic et al., 2016; Walstein et al., 2021; Yatskevich et al., 2024),
290 whereas Aurora B^{Ipl1} phosphorylation of this region strengthens inner and outer kinetochore
291 interactions (Akiyoshi et al., 2013; Kim and Yu, 2015; Yang et al., 2008). Due to signal
292 subtraction of the Mis12c^{Mtw1c} head 2 domain applied during cryo-EM processing, our model
293 of the KMN junction complex did not initially reveal the structural basis of Mis12c^{Mtw1c} auto-
294 inhibition. However, we observed cryo-EM density on the surface of head 1 not accounted
295 for in our model (Figure S2Dii). We reasoned this partial density might correspond to either a
296 region of head 2, and/or a region of Dsn1$^{N\text{-}IDR}$ involved in auto-inhibition (Dimitrova et al.,
297 2016). To investigate these possibilities, we performed focussed 3D classification of the non-
298 signal subtracted KMN particles using a mask encompassing the base of the Mis12c^{Mtw1c}
299 stalk, head 1 and putative head 2 domain (Figure S7A). Using this approach, we obtained a
300 subset of particles that gave rise to 3D reconstructions with defined cryo-EM density for the
301 Mis12c^{Mtw1c} head 1 and head 2 domains (Figure S7 and Table S1).

302 The small number of particles (18,160) exhibiting head 2 associated with head 1 limited the
303 global resolution of the reconstruction to 6.5 Å (Figure S7B), although the local resolution
304 rises to 6.0 Å in regions of the map closest to the head 1 central region (Figure S7C). The
305 overall conformation of head 1 and the Mis12c^{Mtw1c} stalk domain are unchanged compared to
306 the composite cryo-EM map of the KMN junction complex (Figure S8A, B). To interpret the
307 putative head 2 density (Figure S8A, B), we used an AF2 prediction of *S. cerevisiae*
308 Spc24:Spc25:Mis12c^{Mtw1c} (Figure S8C, D). This could account for the helical bundle of head
309 2 docked onto head 1, but not an additional α-helical-like density contacting head 1, nor
310 continuous density between CC1 of the Mtw1c stalk domain and the head 2 domain (Figure
311 S8A, B). Using crosslinking mass spectrometry (CL-MS) on the K$^{HB\text{-}RWD}$M complex, we
312 identified crosslinks between residues in head 1 and head 2 that are in agreement with the
313 docked configuration of head 2 (Figure 4A).

314 The AF2 model of *S. cerevisiae* Mis12c^{Mtw1c} (*Sc*Mis12c^{Mtw1c}) was not consistent with the
315 conformation of head 2 in the *Sc*Mis12c^{Mtw1c} cryo-EM map with improved head 2 density. By
316 contrast, an AF2 prediction of Mis12c^{Mtw1c} from the related budding yeast *Kluyveromyces*
317 *lactis* (*Kl*Mis12c^{Mtw1c}) better recapitulated the contacts between head 1 and 2 observed in the
318 density map. In the *Kl*Mis12c^{Mtw1c} model the head 2 domain is confidently predicted to
319 contact head 1 (Figure S8E, F) and matched our docking of *S. cerevisiae* head 2 into cryo-EM

density (Figure S8B, E). With this prediction of *Kl*Mis12c^{Mtw1c}, we built a model of *Sc*Mis12c^{Mtw1c} which, with only minor rigid body adjustments to the stalk, head 1 and head 2 domains, yielded a most excellent fit into the density map (Figure 4B, C). This model rationalises all cryo-EM density, including that which could not be assigned using AF2 predictions of *Sc*Mis12c^{Mtw1c} (grey density in Figure S8A). A linker within Nsl1 connecting CC1 and head 2 docks into the continuous density between CC1 and head 2 (Figure 4B, C), consistent with observed CL-MS crosslinks between the Nsl1 linker and CC1 residues Dsn1^{K436}, Nsl1^{K105} and Nsl1^{Y106} (Figure 4D). Within the N-IDR of *K. lactis* Dsn1, residues 201-230 (*Kl*Dsn1$^{201-230}$) are predicted to fold as two α-helices joined by a short linker (Figure S8E, F) and dock into the α-helical-like density contacting head 1 and head 2. Indeed, this region of *Kl*Dsn1 mediates association of the *Kl*Mis12c^{Mtw1c} head 1 and head 2 domains *in vitro* and auto-inhibits the interaction of *Kl*Mis12c^{Mtw1c} with *Kl*CENP-C^{Mif2} and *Kl*CENP-U^{Ame1} (Dimitrova et al., 2016). We therefore refer to this region as the Dsn1 auto-inhibitory segment (Dsn1^{AI}). Based on the high sequence similarity of *Sc*Dsn1$^{228-257}$ and *Kl*Dsn1$^{201-230}$ (Figure S8G), we built Dsn1^{AI} of *Sc*Mis12c^{Mtw1c} into the α-helical-like density as *Sc*Dsn1$^{229-255}$ (Figure 4B, C, E) using the *Kl*Mis12^{Mtw1c} AF2 model. This assignment is supported by a CL-MS crosslink between *Sc*Mis12^{Mtw1} Glu84 in head 1 and *Sc*Dsn1$^{229-255}$ Ser240 (Figure 4E). Importantly, *Sc*Dsn1$^{229-255}$ incorporates the Aurora B^{Ipl1} consensus sites Ser240 and Ser250 whose replacement with Asp enhanced the association of *Sc*Dsn1 with inner kinetochore proteins (Akiyoshi et al., 2013). In agreement with this, and as discussed below, phospho-mimetic mutants of the equivalent residues in *Kl*Dsn1$^{201-230}$ (Ser213 and Ser223) substantially increased the affinity of *Kl*Mis12c^{Mtw1c} for N-terminal fragments of CENP-C^{Mif2} and CENP-U^{Ame1} (Dimitrova et al., 2016).

Consistent with our structure, an isothermal titration calorimetry (ITC) experiment showed that a peptide corresponding to Dsn1 residues 228-254 (Dsn1$^{228-254}$) bound to the K^{HB-RWD}M complex with the entire Dsn1^{N-IDR} (residues 1-257) deleted (K^{HB-RWD}M$^{Dsn1\Delta257}$) with a K_D of 1.3 μM (Figure 4Fi). By contrast, the Dsn1$^{228-254}$ peptide did not bind to K^{HB-RWD}M with both the Dsn1^{N-IDR} and head 1 deleted (K^{HB-RWD}M$^{Dsn1\Delta257_\Delta head1}$) (Figure 4Fii). Dsn1$^{229-255}$ is highly basic and projects Lys238, Arg245 and Arg248 towards a large cluster of negatively-charged residues in head 1 (Figure 4E). That the Dsn1$^{228-254}$ peptide-binding site corresponds to the site on head 1 associated with the α-helical-like density was also consistent with a threefold increased K_D for its association with the K^{HB-RWD}M$^{Dsn1\Delta257_Mis12-3A}$ mutant, which has a

disrupted negatively-charged patch on head 1 (Ala substitutions of Mis12^{Mtw1} Glu69, Glu73 and Asp77) (Figure 4E, Fiii).

Phosphoregulation of CENP-C^{Mif2} and CENP-U^{Ame1} binding to Mis12c^{Mtw1c}

K. lactis Dsn1 residues, equivalent to those of *S. cerevisiae* Dsn1 that form the negatively-charged patch of head 1 (Figure 4E), have been implicated in binding the N-termini of CENP-C^{Mif2} and CENP-U^{Ame1} (Dimitrova et al., 2016; Killinger et al., 2020). To understand the mechanism of Mis12c^{Mtw1c} auto-inhibition, we superimposed the crystal structure of the *Kl*Mis12c^{Mtw1c} head 1 bound to CENP-C^{Mif2} (Dimitrova et al., 2016) onto our model of the KMN junction complex. This indicated that the α-helical-like density corresponding to Dsn1^{AI} (Dsn1$^{229-255}$) overlaps with CENP-C^{Mif2} (Figure 5A and S9A, B) bound to head 1, supporting a mechanism for Mis12c^{Mtw1c} auto-inhibition in which Dsn1^{AI} partially occludes the binding site of CENP-C^{Mif2}.

Phosphomimetic mutants of Aurora B^{Ipl1} consensus sites in *Sc*Dsn1$^{229-255}$ and *Kl*Dsn1$^{201-230}$ relieve Mis12c^{Mtw1c} auto-inhibition and enable CENP-C^{Mif2} and CENP-U^{Ame1} to bind the complex with higher affinity (Dimitrova et al., 2016; Lang et al., 2018). *Sc*Dsn1^{S250}, an Aurora B^{Ipl1} kinase substrate (Maskell et al., 2010; Westermann et al., 2003), projects towards the negatively-charged patch of Mis12c^{Mtw1c} head 1 (Figure 4E). Phosphorylation of *Sc*Dsn1^{S250}, and the equivalent residue in *Kl*Dsn1 (Ser223), would cause electrostatic repulsion between the phosphoserine and this negatively-charged patch, and also likely clash with Dsn1 residues of head 2. This might relieve Mis12c^{Mtw1c} auto-inhibition by reducing the binding affinity of the second α-helix in Dsn1^{AI} for head 1, releasing it from the CENP-C^{Mif2} binding site. Although *Sc*Dsn1^{S240} and its equivalent residue, *Kl*Dsn1^{S213}, conform to the Aurora B^{Ipl1} substrate consensus sequence, they have not been shown to be phosphorylated by Aurora B^{Ipl1}. In contrast to *Sc*Dsn1^{S250}, *Sc*Dsn1^{S240} projects away from head 1 (Figure 4E). Nevertheless, if *Sc*Dsn1^{S240} and *Kl*Dsn1^{S213} are phosphorylated, they could establish intramolecular salt bridge interactions with nearby solvent exposed, positively charged residues, such as *Sc*Dsn1^{R237} and *Sc*Dsn1^{R247} (conserved in *K. lactis*, Figure S8G) to relieve Mis12c^{Mtw1c} auto-inhibition by destabilising the Dsn1^{AI} α-helices. Consistent with these proposals, an ITC experiment demonstrated that an *S. cerevisiae* Dsn1$^{228-254}$ peptide with phosphomimetic mutations at the Dsn1^{S240} and Dsn1^{S250} Aurora B^{Ipl1} sites bound to K^{HB-RWD}M$^{Dsn1\Delta257}$ with a K_D of 6.0 μM (Figure 5B), a seven-fold lower affinity than the wildtype peptide (Figure 4Fi).

To test the model that Dsn1^{AI} mediates auto-inhibition of *Sc*Mis12c^{Mtw1c}, we used analytical SEC to assess binding of an N-terminal fragment of CENP-C^{Mif2} comprising residues 1-63 (CENP-C$^{Mif2_1\text{-}63}$) to K$^{HB\text{-}RWD}$M complexes containing Dsn1 N-terminal truncations. CENP-C$^{Mif2_1\text{-}63}$ did not bind K$^{HB\text{-}RWD}$M containing full length Dsn1 (Figure 5C and 5Dii) but did interact with K$^{HB\text{-}RWD}$M$^{Dsn1\Delta257}$ (Figure 5C and 5Diii), similar to previous reports for *Kl*Mis12c^{Mtw1c} (Dimitrova et al., 2016). This indicated that the region mediating Mis12c^{Mtw1c} auto-inhibition is within Dsn1$^{N\text{-}IDR}$. CENP-C$^{Mif2_1\text{-}63}$ did not bind K$^{HB\text{-}RWD}$M$^{Dsn1\Delta226}$ which lacked the N-terminal 226 amino acids of Dsn1 (Figure 5C and 5Div), demonstrating that the reintroduction of only residues 227-257 of Dsn1, corresponding to Dsn1^{AI}, was sufficient to restore Mis12c^{Mtw1c} auto-inhibition. Aurora B^{Ipl1} Dsn1^{S240E} and Dsn1^{S250E} phosphomimetic mutants within Dsn1^{AI} in either full-length Dsn1 (Figure 5C and 5Dv) or Dsn1$^{\Delta1\text{-}226}$ (Figure 5C and 5Dvi) were sufficient to abolish Mis12c^{Mtw1c} auto-inhibition. Together, these results indicate that Dsn1^{AI} auto-inhibits Mis12c^{Mtw1c} by binding to head 1, and that either Aurora B^{Ipl1} phosphorylation of Ser240 and Ser250 or deletion of the N-terminal 257 amino acids of Dsn1 relieves Mis12c^{Mtw1c} auto-inhibition. Thus, Aurora B^{Ipl1} phosphorylation of Dsn1^{AI} is likely to antagonise its auto-inhibitory function by reducing its affinity for head 1, thereby exposing the CENP-C^{Mif2} binding site.

We further investigated the effect of Dsn1^{AI} on the interaction between K$^{HB\text{-}RWD}$M and CENP-C$^{Mif2_1\text{-}63}$ using surface plasmon resonance (SPR). SPR showed that the interaction between K$^{HB\text{-}RWD}$M, which has wild-type Dsn1^{AI}, and CENP-C$^{Mif2_1\text{-}63}$ immobilised on an SPR sensor chip by fusion to a twin-strep tag, had a dissociation constant (K^{kin}_{d}) of 401 nM (Figure 5Ei and 5Eiii). In contrast, the predominant binding mode of K$^{HB\text{-}RWD}$M^{2E} (incorporating Dsn1^{S240E} and Dsn1^{S250E} phosphomimetic mutants) with CENP-C$^{Mif2_1\text{-}63}$ had a dissociation constant (K^{kin}_{d1}) of 262 nM (Figure 5Eii and 5Eiii), an affinity similar to CENP-C$^{Mif2_1\text{-}41}$ binding to *Kl*Mis12c^{Mtw1c} with Dsn1^{AI} deleted (Dimitrova et al., 2016). A minor binding mode of K$^{HB\text{-}RWD}$M^{2E} for CENP-C$^{Mif2_1\text{-}63}$, which had an affinity constant (K^{kin}_{d2}) of 655 nM, was approximately the same as K$^{HB\text{-}RWD}$M for CENP-C$^{Mif2_1\text{-}63}$ (Figure 5Eii and 5Eiii). Therefore, consistent with Aurora B^{Ipl1} phosphorylation of Dsn1 overcoming auto-inhibition of Mis12c^{Mtw1c}, SPR shows that introducing phosphomimetic mutations into Dsn1^{AI} results in K$^{HB\text{-}RWD}$M^{2E} having a 1.5-fold stronger binding affinity for CENP-C$^{Mif2_1\text{-}63}$ than K$^{HB\text{-}RWD}$M (Figure 5Eiii). The absence of an interaction between K$^{HB\text{-}RWD}$M and CENP-C$^{Mif2_1\text{-}63}$ in our analytical SEC experiment is likely due to the concentrations of these

416 components being below their dissociation constant after dilution on the chromatography
417 column.

418 Budding yeast Mis12c^{Mtw1c} binds an N-terminal segment of CENP-U^{Ame1}, however there are
419 conflicting data concerning whether Mis12c^{Mtw1c} auto-inhibition affects this interaction
420 (Dimitrova et al., 2016; Hornung et al., 2014). A complex of *S. cerevisiae* CENP-U^{Ame1} and
421 CENP-Q^{Okp1} (CENP-QU) binds to *Sc*Mis12c^{Mtw1c} with wildtype Dsn1^{AI} (*Sc*Dsn1$^{229-255}$) when
422 both are at micromolar concentrations, as assessed by analytic SEC (Hornung et al., 2014).
423 However, another study using fluorescence polarisation showed that, at lower concentrations
424 (50 nM), the N-terminal 25 amino acids of *K. lactis* CENP-U^{Ame1} did not interact with
425 *Kl*Mis12c^{Mtw1c} containing an intact Dsn1^{AI} (Dimitrova et al., 2016). To investigate these
426 discrepancies and to understand how Dsn1^{AI} regulates Mis12c^{Mtw1c} – CENP-U^{Ame1}
427 interactions, we superimposed an AF2 structure prediction of *S. cerevisiae* head 1 bound to
428 the CENP-U^{Ame1} N-terminus (Figure 6A and Figure S9D) onto our model of the KMN
429 junction complex (Figure 6B). The AF2-predicted structure of CENP-U^{Ame1} residues 1-24
430 (CENP-U$^{Ame1_1-24}$) bound to head 1 clashed with the cryo-EM density for the Dsn1^{AI} α-
431 helical-like density (Figure 6B) more extensively than CENP-C^{Mif2} bound to the Mis12c^{Mtw1c}
432 head 1 domain (Figure 5A). The mode of CENP-U^{Ame1} binding to head 1, involving a basic
433 α-helix lying along the acidic patch of head 1, is strikingly similar to how Dsn1^{AI} interacts
434 with head 1 (Figure 6C and S9A, C). This suggests that Dsn1^{AI} also inhibits the interaction
435 between Mis12c^{Mtw1c} and CENP-U^{Ame1} by occluding the CENP-U^{Ame1}-binding site on head 1.
436 The AF2 model predicts that CENP-U^{Ame1} binds to a site on head 1 that is mainly distinct
437 from the CENP-C^{Mif2}-binding site (Dimitrova et al., 2016), but that both ligands nevertheless
438 share a modest common binding surface. This may explain why CENP-C^{Mif2} and CENP-
439 U^{Ame1} associate with Mis12c^{Mtw1c} mutually exclusively (Killinger et al., 2020).

440 Despite the structure-based prediction that Dsn1^{AI} obstructs the CENP-U^{Ame1} binding site on
441 Mis12c^{Mtw1c}, analytical SEC showed that CENP-QU bound to K^{HB-RWD}M with full-length
442 wild-type Dsn1 (Figure 6D and 6E), consistent with previous results (Hornung et al., 2014).
443 SPR experiments revealed that this finding is likely explained by the tight binding affinity of
444 soluble K^{HB-RWD}M for CENP-QU immobilised on an SPR sensor chip by fusion to a twin-
445 strep tag (K^{kin}_{d1} of 10.9 nM) (Figure 6Fi and 6Fiii). We showed earlier that Dsn1^{S240E} and
446 Dsn1^{S250E} phosphomimetic mutations reduce the binding affinity of the Dsn1$^{228-254}$ peptide to
447 K^{HB-RWD}M$^{Dsn1\Delta257}$ (Figure 5B). We therefore hypothesised that if Dsn1^{AI} auto-inhibits the
448 interaction of Mis12c^{Mtw1c} with CENP-U^{Ame1}, K^{HB-RWD}M^{2E} containing the Dsn1^{S240E} and

449 Dsn1^{S250E} mutations should have a higher binding affinity than K^{HB-RWD}M for CENP-QU.
450 Indeed, the binding affinity (K^{kin}_{d1}) of K^{HB-RWD}M^{2E} for CENP-QU measured 0.59 nM, 18-fold
451 higher than the affinity of K^{HB-RWD}M for CENP-QU (Figure 6Fii and 6Fiii). Notably, minor
452 modes of binding (approximately 20% contribution) of both K^{HB-RWD}M and K^{HB-RWD}M^{2E} for
453 CENP-QU had similar dissociation constants (K^{kin}_{d2} of 23.8 nM and 52.6 nM, respectively)
454 (Figure 6Fi–Fiii). Our results show that Aurora B^{Ipl1} phosphomimetic mutations introduced
455 into Dsn1^{AI} have a much greater effect on the binding affinity of Mis12c^{Mtw1c} for CENP-QU
456 (18-fold increase; Figure 6Fiii) compared to CENP-C^{Mif2} (1.5-fold increase; Figure 5Eiii).
457 This is consistent with the direct steric clash between Dsn1^{AI} and the predicted structure of
458 CENP-U^{Ame1} bound to Mis12c^{Mtw1c} head 1 (Figure 6B), which does not occur for CENP-C^{Mif2}
459 (Figure 5A). Thus, relief of Mis12c^{Mtw1c} auto-inhibition by Aurora B^{Ipl1} phosphorylation has a
460 greater effect on the strength of the CENP-U^{Ame1}-mediated connection between the inner and
461 outer kinetochore than it does for the CENP-C^{Mif2}-mediated connection.

462 The tight binding affinity of *S. cerevisiae* K^{HB-RWD}M for CENP-QU we measured by SPR
463 (K^{kin}_{d1} = 10.9 nM) contrasts with the lack of observed interaction between residues 1-25 of *K.*
464 *lactis* CENP-U^{Ame1} (*Kl*CENP-U$^{Ame1_1-25}$) and *Kl*Mis12c^{Mtw1c} with intact Dsn1^{AI} (Dimitrova et
465 al., 2016). Furthermore, residues 1-25 of *K. lactis* CENP-U$^{Ame1_1-25}$ bound to *Kl*Mis12c^{Mtw1c}
466 containing *Kl*Dsn1^{S213D} and *Kl*Dsn1^{S223D} phosphomimetic mutations with a K_D of 1.48 μM.
467 This is a 2,500-fold lower binding affinity than *S. cerevisiae* K^{HB-RWD}M^{2E} for *S. cerevisiae*
468 CENP-QU (K^{kin}_{d1} of 0.59 nM) (Figure 6Fii and 6Fiii). Since the AF2 model predicts
469 extensive interactions of CENP-U^{Ame1} residues 28-35 with Mis12c^{Mtw1c} head 1 (Figure S9C,
470 F), the use of full-length *S. cerevisiae* CENP-QU in our study is a plausible explanation for
471 these differences.

472 <u>Model for Aurora B^{Ipl1}-dependent activation mediated by conformational changes of head 2</u>

473 The structural elements of the AF2 *Sc*Mis12c^{Mtw1c} model whose conformation did not initially
474 match the cryo-EM map of the KMN junction complex were head 2, the Nsl1 linker and
475 Dsn1^{AI} (Figure 7A, B). Relative to our cryo-EM structure, head 2 in the AF2 *Sc*Mis12c^{Mtw1c}
476 model is rotated 180° about two orthogonal axes and displaced from head 1, with Dsn1^{AI}
477 adopting an extended conformation (Figure 7C, D). The separated configuration of head 1
478 and head 2 in the AF2 *Sc*Mis12c^{Mtw1c} model is reminiscent of crystal structures of human
479 Mis12c bound to CENP-C (Petrovic et al., 2016) and *Kl*Mis12c^{Mtw1c} from which the auto-
480 inhibitory segment was absent (Dimitrova et al., 2016) (Figure 7E, F). Additionally, the

481 orientation of head 2 in the *Kl*Mis12c^{Mtw1c} crystal structure closely matches that of the AF2
482 *Sc*Mis12c^{Mtw1c} model (Figure 7D, E). This suggests that the AF2 *Sc*Mis12c^{Mtw1c} model
483 represents a plausible prediction of the Aurora B^{Ipl1}-phosphorylated, activated state of
484 *Sc*Mis12c^{Mtw1c}. Consistent with this proposal, binding sites for CENP-C^{Mif2} and CENP-U^{Ame1}
485 on head 1 are also not occluded by Dsn1^{AI} in this conformation (Figure S9B, C and Video
486 S2).

487 Dsn1^{AI}-mediated auto-inhibition of *Sc*Mis12c^{Mtw1c} resembles mechanisms proposed for
488 human Mis12c (Yatskevich et al., 2024) (Figure 7C, G). In the auto-inhibited structure of
489 human Mis12c, Dsn1^{AI} functions as a lynchpin by inter-connecting head 1 and head 2. This
490 allows Dsn1^{AI} to sterically block Mis12c association with CENP-C and CENP-T, a contact
491 provided by CENP-U in budding yeast, through direct overlap of their binding sites, and by
492 stabilising the conformation of head 2 that also partially overlaps these sites. Reminiscent of
493 human Mis12c, Dsn1^{AI} bridges the two head domains in auto-inhibited *Sc*Mis12c^{Mtw1c}, and,
494 together with head 2, occludes the inner kinetochore-binding sites on head 1.

495 Model of the entire *S. cerevisiae* KMN complex

496 We were unable to identify particles in our cryo-EM datasets that contained signal for the
497 predicted Knl1c helical bundle domain (Figures S1A, and S10A, B), nor for the Spc24:Spc25
498 and Ndc80:Nuf2 coiled-coils and Ndc80c microtubule-binding elements (Figures S1A, and
499 S10C, D). AF2 generated a predicted structure for the Knl1c helical bundle (residues 492 to
500 632 of Knl1^{Spc105} and 7 to 194 of ZWINT^{Kre28}) with high confidence (Figure S10A and
501 S10B). However, the helical bundle is connected to the Knl1c RWD domains by two
502 segments in Knl1^{Spc105} and ZWINT^{Kre28} ('Knl1c linker 1' and 'Knl1c linker 2') that were
503 predicted to adopt extended conformations with lower pLDDT scores (Figure S10A and
504 S10B). Flexibility of linker 2 would explain why we were unable to resolve Knl1c domains
505 beyond linker 2. Indeed, the Knl1c helical bundle adopts various angles and positions relative
506 to the Knl1c RWD domains in different AF2 models. An equivalent linker does not interrupt
507 the coiled-coil of human Knl1c, possibly explaining why its cryo-EM density was visible in
508 the cryo-EM structure (Yatskevich et al., 2024). We also performed AF2 structure predictions
509 of Ndc80c. We observed a bent conformation that brings the Ndc80c microtubule binding
510 elements (Ndc80c CH domains and Ndc80 N-tail) into proximity with an intermediate section
511 of the Ndc80:Nuf2 coiled-coil (Figure S10C). Although isolated Ndc80c has been observed
512 to exhibit modest bending by negative stain electron microscopy (Wang et al., 2008), such a

513 highly bent conformation is unlikely to be adopted in the presence of microtubules or Dam1c
514 rings (Aravamudhan et al., 2014; Muir et al., 2023). In the structure predicted by AF2, the
515 Spc24:Spc25 coiled-coils are connected to their respective RWD domains by a linker
516 ('Spc24:Spc25 linker') analogous to Knl1c linker 1 and 2 (Figure S10C, D). We expect that
517 we were unable to resolve any domains beyond the Spc24:Spc25 linker in our cryo-EM
518 analysis because it flexibly tethers the Ndc80c coiled-coils and microtubule binding elements
519 to the KMN junction. FRET measurements performed in the absence of both microtubules
520 and Dam1c have shown that Ndc80c bending is dynamic, and that more tightly bent Ndc80c
521 conformations than those predicted by AF2 are possible (Scarborough et al., 2019). However,
522 these tightly bent conformations are adopted with low propensity when Mis12c^{Mtw1c} is bound,
523 which is the case for the KMN reconstitutions used in our structural analyses (Scarborough et
524 al., 2019).

525 We generated a hypothetical model of the entire *S. cerevisiae* KMN complex by
526 superimposing the AF2 predictions of Knl1c and Ndc80c (Figure S10) onto their
527 corresponding RWD domains in the KMN junction complex structure (Figure 8A). The close
528 proximity of the Knl1c helical bundle to the Spc24:Spc25 coiled-coils in the hypothetical
529 model is consistent with previous CL-MS analysis of the budding yeast KMN complex
530 (Ghodgaonkar-Steger et al., 2020), although the exact positions of the domains are probably
531 not correct. The Knl1c helical bundle is also close to the Ndc80c microtubule binding
532 elements, suggesting this is possible in some conformations of the complex. The flexible
533 tethering of other Knl1c and Ndc80c domains to the RWD domains of the KMN junction
534 could have important functional consequences for spindle assembly checkpoint (SAC)
535 signalling. Experiments in humans and budding yeast are consistent with a model in which
536 SAC signalling is activated at kinetochores that are not attached to microtubules (Rieder et
537 al., 1995; Wells and Murray, 1996), and that therefore do not incorporate Dam1c rings (Li et
538 al., 2002; Tanaka et al., 2007; Tanaka et al., 2005). Under these conditions, Ndc80c might
539 adopt a conformation in which its microtubule binding elements localise near the Knl1c
540 helical bundle domain and the N-terminal disordered region of Knl1^{Spc105}. This may facilitate
541 Mps1, bound proximal to the Ndc80c CH domains (Parnell et al., 2024; Pleuger et al., 2024;
542 Zahm and Harrison, 2024), in phosphorylating MELT motifs in the Knl1^{Spc105} N-terminal
543 disordered region to stimulate SAC signalling. In contrast, Ndc80c bound to a microtubule
544 and Dam1c ring does not adopt such a tightly bent conformation (Aravamudhan et al., 2014;
545 Muir et al., 2023). As this is a substrate for error correction signalling (EC) signalling (Muir

546 et al., 2023), close spatial proximity of the Knl1c helical bundle domain and Ndc80c
547 microtubule binding elements is unlikely to be relevant to the correction of erroneous
548 kinetochore-microtubule attachments.

549 **Discussion**

550 Our cryo-EM structure and biochemical data of the *S. cerevisiae* KMN junction complex
551 together with previous studies revealed both similarities and differences in how budding yeast
552 Mis12c^{Mtw1c} and human Mis12c interact with Knl1c and Ndc80c, and the mechanism of
553 Aurora B^{Ipl1}-mediated regulation of KMN assembly onto the inner kinetochore. For both
554 species, Mis12c^{Mtw1c}/Mis12c interacts with Knl1c and Ndc80c through two distinct
555 interaction modes. In a conserved mode of interaction, the coiled-coil (CC3) α-helices of the
556 Mis12c^{Mtw1c}/Mis12c stalk creates a rigid interface for the docking of Knl1c and Ndc80c
557 (Figure 8B, C). Specifically, Dsn1:Nsl1 contact Ndc80c, whereas Dsn1:Pmf1^{Nnf1}/Pmf1
558 contact Knl1c. The other mode of interaction is mediated by the C-terminal extensions of
559 Mis12c^{Mtw1c}/Mis12c subunits that interact with docking sites on Knl1c and Ndc80c.
560 Conserved in both human and budding yeast KMN is the interaction of the C-terminal α-
561 helix of Dsn1 (Dsn1$^{Cterm-helix}$) with a groove formed at the interface of the Spc24:Spc25 RWD
562 domains of Ndc80c (Figure 8B, C). The same site on the Spc24:Spc25 RWD domains binds
563 the Ndc80c-binding α-helix of CENP-T (Malvezzi et al., 2013; Nishino et al., 2013). The
564 most striking difference between budding yeast and human KMN is the contrasting functions
565 of the Mis12^{Mtw1} and Nsl1 subunits to contact Knl1c and Ndc80c. In the human KMN
566 complex, an α-helix of Nsl1 (Nsl1$^{Spc24-helix}$), immediately C-terminal to the Mis12c shaft,
567 contacts the Spc24:Spc25 RWD domains of Ndc80c (Figure 8B). The Nsl1 chain then
568 extends to engage Knl1c at both Knl1^{RWD-N} and at the Knl1^{RWD-N}:ZWINT interface using a
569 distinct segment, Nsl1^{Cterm} (Figure 8B). In budding yeast these roles of Nsl1 are substituted
570 by Mis12^{Mtw1}. Mis12$^{Mtw1_Spc24-helix}$ contacts the Spc24:Spc25 RWD domains, which also
571 stabilises the Dsn1$^{Cterm-helix}$:Spc24^{RWD}:Spc25^{RWD} interaction (Figure 8C). Analogously to Nsl1
572 in human KMN, the Mis12^{Mtw1} chain then interacts with the Knl1$^{Spc105_RWD-N}$:Kre28^{ZWINT}
573 interface of Knl1c (Figure 8C).

574 We determined a cryo-EM reconstruction of the KMN junction complex, at lower resolution,
575 in which head 2 of Mis12c^{Mtw1c} was resolved. This enabled us to propose mechanisms by
576 which assembly of the KMN complex onto the inner kinetochore is auto-inhibited, and by
577 which auto-inhibition is relieved by Aurora B^{Ipl1} phosphorylation. We interpreted the

578 conformation of head 2 in this cryo-EM density using an AF2 model and experimental
579 crosslinking mass-spectrometry. Notably, by interpreting the crosslinking mass-spectrometry
580 dataset collected on a $K^{HB\text{-}RWD}M$ complex, an AF2 model of $Mis12c^{Mtw1c}$ from *K. lactis*, and
581 isothermal titration calorimetry data, we assigned an α-helical-like density associated with
582 the $Mis12c^{Mtw1c}$ head 1 domain to an auto-inhibitory region within $Dsn1^{N\text{-}IDR}$ ($Dsn1^{AI}$)
583 containing key Aurora B^{Ipl1} sites. Analytical SEC and SPR experiments showed that $Dsn1^{AI}$
584 suppressed binding of $Mis12c^{Mtw1c}$ to the N-terminal segments of both CENP-C^{Mif2} and
585 CENP-QU, demonstrating its auto-inhibitory function. Introducing phosphomimetic
586 mutations into Aurora B^{Ipl1} sites within a peptide modelled on $Dsn1^{AI}$ reduced its affinity for
587 the $K^{HB\text{-}RWD}M^{Dsn1\Delta257}$ complex. Additionally, Knl1c:$Mis12c^{Mtw1c}$ containing the same
588 mutations in $Dsn1^{AI}$ bound both CENP-C^{Mif2} and CENP-QU with increased affinity. These
589 results suggest that the intra-molecular association of $Dsn1^{AI}$ with $Mis12c^{Mtw1c}$ head 1 is
590 responsible for $Mis12c^{Mtw1c}$ auto-inhibition, and that Aurora B^{Ipl1} phosphorylation of serine
591 residues within this region relieves $Mis12c^{Mtw1c}$ auto-inhibition by reducing the binding
592 affinity of $Dsn1^{AI}$ for head 1. Notably, our results show that regulation of the interaction
593 between $Dsn1^{AI}$ and head 1 by Aurora B^{Ipl1} strengthens the interaction between CENP-U^{Ame1}
594 and $Mis12c^{Mtw1c}$ to a greater extent than the interaction between CENP-C^{Mif2} and
595 $Mis12c^{Mtw1c}$. Cryo-EM structures and AF2 models suggest that this is because the $Dsn1^{AI}$ and
596 CENP-U^{Ame1} protein main chains would sterically clash if both bound to head 1 (Figure 6B).
597 Such a steric clash does not occur between CENP-C^{Mif2} and $Dsn1^{AI}$ when bound to head 1;
598 instead, the two elements appear to compete for contacts with the same amino side chains
599 within head 1 (Figure 5A). Aurora B^{Ipl1} localisation to CCAN is necessary for the correction
600 of erroneous kinetochore microtubule attachments (Fischböck-Halwachs et al., 2019; García-
601 Rodríguez et al., 2019; Li et al., 2023). As such, our findings suggest a mechanism by which
602 attachments of mitotic chromosomes to spindle microtubules, mediated by the connection of
603 KMN complexes to centromere-bound CCAN through either CENP-C^{Mif2} or CENP-U^{Ame1},
604 are strengthened at kinetochores that are able to correct errors in these attachments.

605 Our study allows a comparison of the mechanism of *S. cerevisiae* $Mis12c^{Mtw1c}$ auto-inhibition
606 with human Mis12c. Human Mis12c $Dsn1^{AI}$, also containing two Aurora B sites, forms an N-
607 terminal α-helix followed by an extended segment that docks against both head 1 and head 2,
608 stabilising the interaction of the two head domains (Figure 7F) (Yatskevich et al., 2024). This
609 occludes the binding sites for the human Mis12c-binding inner kinetochore subunits CENP-C
610 and CENP-T, inhibiting their interactions with Mis12c (Petrovic et al., 2016; Walstein et al.,

611 2021; Yatskevich et al., 2024). The first Aurora B phosphorylation site in human Dsn1,
612 Ser100, is within the Dsn1^{AI} α-helix, and projects towards the Mis12c head 1 domain. The
613 Ser100 hydroxyl group forms a hydrogen bond with the main chain amide group of Arg98,
614 capping and stabilising the N-terminal α-helix. The second Aurora B phosphorylation site,
615 Ser109, is embedded in the extended segment, with its side chain forming a hydrogen bond
616 with a residue in Mis12c head 2 that is flanked by negatively charged residue, analogous to
617 how Ser250 of budding yeast Dsn1^{AI} projects towards a negatively charged patch in
618 Mis12c^{Mtw1c} head 1 (Figure 6C). Similar to budding yeast, introduction of phosphomimetic
619 mutations into Ser100 and Ser109 reduces the binding affinity of Dsn1^{AI} to Mis12c, and
620 relieves Mis12c auto-inhibition to allow interaction with CENP-C and CENP-T (Petrovic et
621 al., 2016; Walstein et al., 2021; Yatskevich et al., 2024). This probably recapitulates the
622 effects proposed to accompany Ser100 and Ser109 phosphorylation, namely destabilisation of
623 the N-terminal α-helix (Ser100 phosphorylation), and establishment of repulsive electrostatic
624 forces with the negatively-charged patch in Mis12c head 2 (Ser109 phosphorylation).
625 Comparison of our model of budding yeast Dsn1 Ser240 and Ser250 with that of human
626 Ser100 and Ser109, suggests conceptually related phosphorylation-dependent mechanisms
627 are responsible for relieving human Mis12c and budding yeast Mis12c^{Mtw1c} auto-inhibition.

628 In summary, our work has revealed that the mechanisms mediating assembly and auto-
629 inhibition of the KMN complex are conserved at the structural level in humans and budding
630 yeast. Our work shows that a combination of conserved and more plastic interfaces, divergent
631 at the sequence and subunit level, underpin a nevertheless comparable overall KMN complex
632 architecture between point and regional centromeres. Furthermore, our work reveals that
633 Aurora B^{Ipl1}-mediated phosphorylation overcomes auto-inhibition of human Mis12c and
634 budding yeast Mis12c^{Mtw1c} through similar structural mechanisms. In humans, Aurora B
635 regulation of Mis12c auto-inhibition probably restricts KMN complex recruitment to mitotic
636 kinetochores that are competent to correct erroneous kinetochore-microtubule attachments
637 through error correction (EC) signalling (Yatskevich et al., 2024). Our work reveals that, in
638 budding yeast, the inner kinetochore subunits CENP-C^{Mif2} and CENP-U^{Ame1} bind with
639 appreciable affinity to unphosphorylated Mis12c^{Mtw1c}. As such, kinetochore function is
640 probably affected more modestly by Aurora B^{Ipl1} regulation of Mis12c^{Mtw1c} auto-inhibition
641 than in humans. In contrast to humans, the KMN complex is attached to the centromere
642 throughout almost the entire cell cycle in budding yeast, with only transient disassembly of
643 kinetochores during S-phase (Kitamura et al., 2007). Furthermore, Aurora B^{Ipl1} is recruited to

644 kinetochores from G1 to metaphase, being depleted from centromeres under tension at
645 metaphase and relocalising to the spindle midzone (Buvelot et al., 2003; Campbell and Desai,
646 2013; Edgerton et al., 2023; Nerusheva et al., 2014; Shimogawa et al., 2009). Consequently,
647 relief of Mis12c^{Mtw1c} auto-inhibition from G1-phase to metaphase through phosphorylation
648 by Aurora B^{Ipl1} most likely strengthens the pre-existing connections between the inner and
649 outer kinetochore, allowing bioriented kinetochores to withstand the pulling and pushing
650 forces exerted by spindle microtubules. However, the slightly diminished, but not abolished,
651 affinity of both CENP-U^{Ame1} and CENP-C^{Mif2} for unphosphorylated Mis12c^{Mtw1c} is possibly
652 still able to support kinetochore-microtubule attachment during anaphase after Aurora B^{Ipl1}
653 has localised away from kinetochores.

654 **Materials and methods**

655 Cloning of *S. cerevisiae* CENP-C^{Mif2} and *S. cerevisiae* KMN complex proteins

656 Genes encoding *S. cerevisiae* Ndc80, Nuf2, Spc24, Spc25, Dsn1, Mis12^{Mtw1}, Pmf1^{Nnf1}, Nsl1,
657 residues 1-444 of Knl1^{Spc105}, and ZWINT^{Kre28} were each amplified by Polymerase chain
658 reaction (PCR) from *S. cerevisiae* strain S288c genomic DNA (Zhang et al., 2016). Genes
659 encoding Ndc80 and Nuf2 were cloned into the same *pU1* plasmid (Zhang et al., 2016).
660 Genes encoding Spc24 and Spc25 were cloned into the same *pF1* plasmid (Zhang et al.,
661 2016). Genes encoding Knl1^{Spc105} residues 445-917 (Knl1$^{Spc105_HB\text{-}RWD}$) and ZWINT^{Kre28} were
662 cloned into the same modified *pF1* plasmid. Genes encoding Knl1^{Spc105} residues 710–917
663 (Knl1^{Spc105_RWD}) and ZWINT^{Kre28} residues 268-385 (ZWINT^{Kre28_RWD}) were cloned into the
664 same modified *pF1* plasmid. TEV and HRV-3C cleavable twin-strep-tag II (TS) tags were
665 introduced into the C-termini of Nuf2 and ZWINT^{Kre28}, respectively, and a tandem tag
666 comprising maltose binding protein (MBP) fused to monomeric enhanced green fluorescent
667 protein (mEGFP) was introduced into the N-terminus of Knl1^{Spc105_RWD}. Genes encoding
668 Dsn1, Mis12^{Mtw1}, Nsl1, and Pmf1^{Nnf1} were cloned into the same modified *pF1* plasmid for
669 coexpression with Knl1^{Spc105} and ZWINT^{Kre28}. For expression of Mis12c^{Mtw1c} and
670 Mis12c^{Mtw1c} mutants, Dsn1 and Nsl1 were cloned into the same modified *pF1* plasmid and
671 twin-strep-tag II was introduced into the N-terminus of Dsn1. This plasmid was used to
672 generate a virus for coexpression with a second virus generated from a another modified *pF1*
673 plasmid containing a Mis12^{Mtw1}-Pmf1^{Nnf1} pair. Constructs for Dsn1$^{\Delta 1\text{-}226}$, Dsn1$^{\Delta 1\text{-}}$
674 ^{226,S240E,S250E}, Dsn1$^{\Delta 1\text{-}257}$, Dsn1^{S240E,S250E}, Mis12^{Mtw1_E69A,E73A,E77A}, Mis12$^{Mtw1_\Delta 272\text{-}C}$, and
675 Pmf1$^{Nnf1_\Delta 180\text{-}C}$ were created using primers supplied from Merck and the KLD reaction kit

676 supplied by New England Biolabs and cloned into plasmids containing all other Mtw1c
677 subunits for coexpression with Knl1$^{Spc105_HB\text{-}RWD}$ and ZWINT^{Kre28}. Constructs for
678 Mis12$^{Mtw1_\Delta 272\text{-}C}$ and Pmf1$^{Nnf1\Delta_180\text{-}C}$ were additionally cloned into the plasmid containing the
679 Mis12^{Mtw1}-Pmf1^{Nnf1} pair and expressed together with a virus made from the plasmid
680 containing a Dsn1-Nsl1 pair. To express Knl1c:Mis12c^{Mtw1c} with the Mis12c head 1 domain
681 deleted, constructs for Mis12$^{Mtw1_\Delta 1-106}$ and Pmf1$^{Nnf1_\Delta 1\text{-}104}$ were cloned with Dsn1$^{\Delta 1\text{-}257}$ and
682 wildtype Nsl1 into the same modified *pF1* plasmid and coexpressed with Knl1^{Spc105} and
683 ZWINT^{Kre28}. To express Knl1c:Mis12c^{Mtw1c} with mutated Dsn1, constructs for Mis12^{Mtw1},
684 Pmf1^{Nnf1}, Nsl1, and mutant Dsn1 were cloned into the same modified *pF1* plasmid and
685 coexpressed with Knl1^{Spc105} and ZWINT^{Kre28}.

686 The gene encoding *S. cerevisiae* CENP-C^{Mif2} residues 1-63 (CENP-C$^{Mif2_1\text{-}63}$) was amplified
687 from *S. cerevisiae* strain S288c genomic DNA and cloned into a pET28 plasmid carrying a
688 Kanamycin selectable marker. A 6xHis-SUMO- tag was introduced into the N-terminus of the
689 protein. A construct to express protein for surface plasmon resonance (SPR) was assembled
690 by introducing a 6xHis-SUMO- tag was introduced into the N-terminus of the protein and a
691 glycine-serine-glycine linker followed by a twin-strep-tag II (TS) tag into the C-terminus of
692 the protein.

693 To construct plasmids for yeast strain construction, the promoter, coding regions, and
694 terminator regions defined previously for the *MTW1* and *NNF1* genes in the yeast genome
695 (Euskirchen, 2002) were amplified from *S. cerevisiae* strain S288c genomic DNA. The
696 *MTW1* fragments were cloned into a modified *pRS304* plasmid (Frigola et al., 2013) and a
697 HA_3 tag was introduced into the N-terminus of the protein in a single step using NEBuilder
698 HiFi DNA assembly reaction kit supplied by New England Biolabs. The *NNF1* fragments
699 were cloned into a modified *pRS305* plasmid (Frigola et al., 2013) and a $V5_3$ tag was
700 introduced into the N-terminus of the protein in a single step using NEBuilder HiFi DNA
701 assembly reaction kit. A *pRS304* series plasmid and a *pRS305* series plasmid encoding HA_3-
702 Mis12$^{Mtw1_\Delta 272\text{-}C}$ and $V5_3$-Pmf1$^{Nnf1_\Delta 180\text{-}C}$ were constructed from the plasmids described above
703 using PCR with primers supplied by Merck followed by processing with the KLD reaction kit
704 supplied by New England Biolabs.

705 <u>Expression and purification of KMN subcomplexes, and CENP-C$^{Mif2_1\text{-}63}$ and CENP-QU</u>
706 <u>complexes</u>

707 Baculoviruses for expression of KMN subcomplexes were generated from the plasmids
708 described above using methods described previously (Zhang et al., 2016). Ndc80c was
709 expressed from two baculoviruses encoding a Ndc80-Nuf2 gene pair and a Spc24-Spc25 gene
710 pair in High-5 insect cells. Six-subunit Knl1c:Mis12c^{Mtw1c} complexes were expressed from
711 two baculoviruses encoding a Knl1$^{Spc105_HB\text{-}RWD}$-ZWINT^{Kre28} gene pair and a Dsn1- Nsl1-
712 Mis12^{Mtw1}-Pmf1^{Nnf1} gene quartet in High-5 insect cells. Isolated Mis12c^{Mtw1c} was expressed
713 from two baculoviruses encoding Mis12^{Mtw1}-Pmf1^{Nnf1} and Dsn1-Nsl1 gene pairs. The Sf9 and
714 High-5 insect cell lines used for baculovirus generation and protein complex expression were
715 not tested for mycoplasma contamination or authenticated. 2 L roller bottles containing 500
716 mL suspension cultures of High-5 cells were typically infected with 2.5% vol/vol of P3 Sf9
717 suspension cell culture, and the High-5 expression cultures were subsequently harvested 42–
718 70 h after infection when the cell viability had dropped to 75–85%.

719 All purification steps were carried out at 4 ˚C or on ice. Cells expressing Ndc80c,
720 Knl1c:Mis12c^{Mtw1c}, or Mis12c^{Mtw1c} were lysed by sonication in lysis buffer (50 mM Tris.HCl
721 pH 8.5, 8 mM benzamidine, 1 mM EDTA, 1 mM TCEP, 0.2 mM PMSF, cOmplete EDTA-
722 free protease inhibitor tablets) containing benzonase and either 300 mM NaCl and 7.5%
723 glycerol (Ndc80c), 250 mM NaCl and 7.5% glycerol (Mis12c^{Mtw1c}), or 200 mM NaCl and 5%
724 glycerol (Knl1c:Mis12c^{Mtw1c}). Lysates were cleared by ultracentrifugation at 38,000 x *g* for
725 one h and loaded onto Strep-Tactin superflow plus cartridges (Qiagen). Immobilised
726 complexes were washed with lysis buffer after adjusting to pH 8.0. Immobilised
727 Knl1c:Mis12c^{Mtw1c} complexes were subjected to further washes with a buffer containing ATP
728 (50 mM Tris.HCl pH 8.0, 175 mM KCl, 10 mM $MgCl_2$, 2.5 mM ATP sodium salt, 1 mM
729 TCEP, 2.5% glycerol) followed by a buffer containing 50 mM Tris.HCl pH 8.0, 200 mM
730 NaCl, 2.5% glycerol. Bound complexes were then eluted using a buffer containing 50 mM
731 Tris.HCl pH 8.0, 2.5 mM d-desthiobiotin, 1 mM TCEP, and either 100 mM NaCl (Ndc80c,
732 Mis12c^{Mtw1c}, and Knl1c:Mis12c^{Mtw1c} used for SPR) or 200 mM NaCl (Knl1c:Mis12c^{Mtw1c} for
733 all applications other than SPR). Knl1c:Mis12c^{Mtw1c} used for SPR was incubated overnight
734 with TEV protease whilst rolling at 4 ˚C to remove the C-terminal twin-strep-tag II sequences
735 from Kre28.

736 Knl1c:Mis12c^{Mtw1c} used for SPR and Ndc80c were further purified by loading the TEV
737 protease cleavage reaction and Strep-Tactin eluate, respectively, onto a Resource Q anion
738 exchange column (Cytiva). Bound complexes were eluted with buffer containing 50 mM
739 Tris.HCl pH 8.0, 1 mM TCEP, 2.5% glycerol and a gradient from 100 mM to 1000 mM NaCl

740 over 15-20 column volumes. Peak fractions were pooled, and salt concentration in pooled
741 Knl1c:Mtw1c protein was reduced to 150 mM prior to incubation for 30 min whilst rolling at
742 4 °C. Pooled protein was further purified using a Superose 6 10/300 increase GL column
743 (Cytiva) equilibrated in KMN buffer (20 mM HEPES pH 7.5, 150 mM NaCl, 1 mM TCEP).
744 Peak Ndc80c fractions were pooled, concentrated, and flash frozen using liquid nitrogen.

745 Mis12c^{Mtw1c} complexes and Knl1c:Mis12c^{Mtw1c} complexes used for all applications other than
746 SPR were further purified by concentrating the Strep-Tactin eluate and applying it to a
747 Superose 6 increase 10/300 GL column equilibrated in KMN buffer. The peak protein
748 complex fractions were concentrated and flash frozen using liquid nitrogen.

749 CENP-C$^{Mif2_1\text{-}63}$ with a N-terminal 6xHis-SUMO- tag was expressed in *E. coli* BL-21
750 CodonPlus RIL cells by induction with 0.5 mM IPTG at a cell culture OD_{600nm} = 0.8 followed
751 by incubation of cells a further 18 h at 18 °C with shaking. Cells were harvested by
752 centrifugation and lysed by sonication in lysis buffer (30 mM Tris.HCl pH 8.0, 300 mM
753 NaCl, 1 mM EDTA, 1 mM TCEP, 0.2 mM PMSF) containing benzonase and 10 mM
754 imidazole. The lysate was cleared by ultracentrifugation at 38,000 x *g* in a JA25.50 rotor for
755 1 h, and the clarified lysate was applied to a HisTrap excel column (Cytiva). Immobilised
756 proteins were washed with lysis buffer and were eluted by successive applications of lysis
757 buffer containing 50 mM, 100 mM, 150 mM, 300 mM, and 500 mM imidazole. The eluates
758 obtained after application of 150 mM and 300 mM imidazole were pooled and applied to
759 HiPrep 26/10 desalting columns (Cytiva) that were equilibrated in buffer containing 20 mM
760 HEPES pH 7.5, 300 mM NaCl, 1 mM EDTA, 1 mM TCEP) to reduce the imidazole content.

761 CENP-C$^{Mif2_1\text{-}63}$ with a N-terminal 6xHis-SUMO- tag and a C-terminal twin-strep-tag II (TS)
762 tag (CENP-C$^{Mif2_1\text{-}63}$-TS) was expressed in *E. coli* BL-21 CodonPlus RIL cells by induction
763 with 0.5 mM IPTG at a cell culture OD_{600nm} = 0.7 followed by incubation of cells a further 14
764 h 30 min at 18 °C with shaking. Cells were harvested by centrifugation and lysed by
765 sonication in lysis buffer (30 mM Tris.HCl pH 8.0, 300 mM NaCl, 1 mM EDTA, 1 mM
766 TCEP, 0.2 mM PMSF) containing benzonase. The lysate was cleared by ultracentrifugation at
767 48,000 x *g* in a JA25.50 rotor for 45 min, and the clarified lysate was applied to Strep-Tactin
768 superflow plus cartridges (Qiagen). Immobilised proteins were washed with lysis buffer
769 followed by wash buffer 2 (20 mM HEPES pH 7.0, 150 mM NaCl, 1 mM TCEP) and were
770 eluted using wash buffer 2 containing 2.5 mM d-desthiobiotin.

771 The 6xHis-SUMO tag was removed from the CENP-C$^{Mif2_1-63}$ and CENP-C$^{Mif2_1-63}$-TS by
772 overnight incubation with recombinant Ulp1 protease carrying a 6xHis tag at 4 ˚C. Cleaved
773 protein was isolated from the protease by a reverse IMAC purification step. After diluting the
774 salt concentration to 100 mM, the reverse IMAC flow through was applied to a Resource S
775 cation exchange column (Cytiva) for further purification. CENP-C$^{Mif2_1-63}$ was eluted using
776 buffer containing 20 mM HEPES pH 7.5, 300 mM NaCl, 1 mM TCEP. CENP-C$^{Mif2_1-63}$-TS
777 was eluted using buffer containing 20 mM HEPES pH 7.5, 1 mM TCEP, and a gradient from
778 100 mM to 1000 mM NaCl over 15 column volumes. CENP-C$^{Mif2_1-63}$ and CENP-C$^{Mif2_1-63}$-
779 TS were concentrated and further purified by application to a Superdex 75 16/60 column
780 (Cytiva) equilibrated in KMN buffer. Peak CENP-C$^{Mif2_1-63}$ fractions were pooled,
781 concentrated, and flash frozen using liquid nitrogen.

782 CENP-QU was expressed and purified according to the method described for CENP-ΔQU
783 complex in (Dendooven et al., 2023).

784 Reconstitution and GraFix crosslinking the *S. cerevisiae* KMN complex for cryo-EM

785 The *S. cerevisiae* KMN complex was reconstituted and crosslinked for cryo-EM using a
786 GraFix protocol (Stark, 2010). Two buffers were used to prepare 10–30% continuous glycerol
787 gradients (4 mL total volume) with an additional 0.0–0.2% glutaraldehyde component using a
788 gradient master: buffer A contained 20 mM HEPES pH 7.5, 150 mM NaCl, 10% glycerol, 1
789 mM TCEP, and buffer B contained 20 mM HEPES pH 7.5, 150 mM NaCl, 30% glycerol, 1
790 mM TCEP, 0.2% glutaraldehyde. Stocks of Ndc80c and a Knl1c:Mis12c^{Mtw1c} complex that
791 contained Knl1$^{Spc105_HB-RWD}$ (K^{HB-RWD}M) were thawed on ice, and diluted and mixed at a 4
792 μM equimolar (1:1) ratio in KMN buffer. The mixture was incubated for 30 min at 4 ˚C to
793 reconstitute the KMN complex.

794 200 pmol (50 μL volume) of reconstituted K^{HB-RWD}MN complex was applied to each glycerol
795 gradient, and gradients were subsequently subjected to centrifugation at 50,000 rpm in a SW
796 60 Ti Swinging-Bucket Rotor (Beckman Coulter) for 16 h. Glycerol gradients were manually
797 fractionated into 250 μL fractions, and unreacted glutaraldehyde was quenched by pipetting
798 the fractions over a solution of 1 M Tris.HCl pH 7.5 such that the final concentration of
799 Tris.HCl in each fraction was 20 mM. Fractions encompassing the gradient volume 2.00–2.75
800 mL were pooled, glycerol content was reduced by application to Zeba spin desalting columns
801 equilibrated in KMN buffer, and the protein complex was concentrated to a final
802 concentration of 0.8 mg/mL.

803 Cryo-EM grid preparation

804 Cryo-EM grids were glow discharged in an Edwards S150B glow discharger for 60 s at
805 setting 6, 20–25 Ma, 1.2 kV and 0.2 mBar (0.15 Torr) immediately prior to application of
806 sample. 3 µL of reconstituted and crosslinked $K^{HB\text{-}RWD}$MN complex was applied to freshly
807 glow discharged UltrAuFoil 300 mesh gold R1.2/1.3 grids (Quantifoil Micro Tools). Grids
808 were mounted in a FEI Vitrobot mark III humidity chamber (maintained at 4 ˚C, 100%
809 humidity), blotted with Whatman filter paper I (2 s blotting time, -7 blotting force), and
810 vitrified in liquid ethane.

811 Cryo-EM data acquisition

812 Cryo-EM movies were collected on a Thermo Fisher Scientific Titan Krios 1 microscope
813 operating at 300 keV using a Gatan K3 camera equipped with a Gatan energy filter. Movies
814 were collected at x105,000 magnification (pixel size 0.825 Å px^{-1}) with a 1.75 s exposure and
815 15.6 e^-/px/s fluence, providing a total dose of 40 $e^-/Å^2$, and were split into 40 frames. A series
816 of movies were collected over a range of defoci from -1.4 µm to -3.0 µm, at an interval of 0.4
817 µm. Data acquisition was performed using aberration-free image shifts (AFIS) as employed
818 in the Thermo Fisher Scientific 'EPU' automated data acquisition software.

819 Cryo-EM data processing

820 Alignment of micrograph raw movie frames and correction to a single micrograph image was
821 performed using UCSF MotionCor2 as implemented in RELION (Kimanius et al., 2021;
822 Zheng et al., 2017). The contrast transfer function (CTF) of each motion corrected
823 micrograph was estimated using CTFFIND-4.1 as implemented in RELION (Kimanius et al.,
824 2021; Rohou and Grigorieff, 2015). Manual particle picking of 10 micrographs was used to
825 train a Topaz model that was used to pick the entire dataset of 26,390 micrographs (Bepler et
826 al., 2019) (Figure S2 and Table S1). The particles picked by the first Topaz model were
827 curated by two successive rounds of 2D classification in CryoSPARC (Punjani et al., 2017).
828 2D classification in CryoSPARC was always performed using batch sizes of 400 and 40
829 online-em iterations. Particles classified into class averages that resembled KMN were
830 selected and used to train a second Topaz model in RELION that was once again used to pick
831 all 26,390 micrographs.

832 Particles were separated into six distinct sets, based on the appearance of 2D class averages,
833 using two successive rounds of 2D classification in CryoSPARC. Each set of particles was

used to generate an *ab initio* model in CryoSPARC, yielding one KMN model, one additional protein model, and four decoy noise models. All six *ab initio* models were used as references for a noise decoy classification step using the heterogeneous refinement job type in CryoSPARC. Particles corresponding to the model that resembled the KMN complex were subjected two further successive rounds of 2D classification, yielding 321,078 particles that corresponded to 2D class averages that resembled KMN. This set of particles was further processed in RELION for all subsequent steps. All 3D refinement and 3D classification jobs in RELION used Blush regularization, as implemented in RELION 5.0 (Kimanius et al., 2021; Kimanius et al., 2024).

The particles were used to generate an *ab initio* model, against which they were refined (successive unmasked and masked refinements) to reconstruct a cryo-EM density map with a resolution of 7.5 Å and discontinuous density for the Spc24 and Spc25 RWD domains and the Mis12c^{Mtw1c} head 2 domain.

To better resolve the Spc24 and Spc25 RWD domains, particles were subjected to focussed 3D classification without alignment using a mask encompassing the CC3 region of the Mis12c^{Mtw1c} stalk domain, the Knl1c RWD domains, and the Spc24 and Spc25 RWD domains, and a *T* value of 25. A set of 113,688 particles corresponding to two 3D classes with improved continuity of the Spc24 and Spc25 RWD domain density were refined to reconstruct a cryo-EM density map with a resolution of 6.5 Å and discontinuous density for the Mis12c^{Mtw1c} head 2 domain. Signal corresponding to the Mis12c^{Mtw1c} head 2 domain was subtracted from the particle images, and the subtracted particles were refined to reconstruct a cryo-EM density map with a resolution of 6.0 Å. Two non-overlapping masks were generated for multibody refinement: one encompassed part of the CC2 region of the Mis12c^{Mtw1c} stalk domain, the CC3 region of the Mis12c^{Mtw1c} stalk domain, the Knl1c RWD domains, and the Spc24 and Spc25 RWD domains ('apex mask 1'), whilst the other encompassed the Mis12c^{Mtw1c} head 1 domains, the CC1 region of the Mis12c^{Mtw1c} stalk domain, and the remaining segment of the CC2 region of the Mis12c^{Mtw1c} stalk domain ('base mask 1'). Multibody refinement using these masks yielded two cryo-EM density maps with global resolutions (GS-FSC) of 4.8 Å ('apex body 1') and 4.9 Å ('base body 1'), respectively.

To better resolve the Mis12c^{Mtw1c} head 2 domain, particles were subjected to focussed 3D classification without alignment using a mask encompassing the Mis12c^{Mtw1c} head 1 and head 2 domains and the CC1 region of the Mis12c^{Mtw1c} stalk domain (Figure S7 and Table S1). A

set of 18,160 particles corresponding to a 3D class with continuous density for the Mis12c^{Mtw1c} head 2 domain were refined to reconstruct a cryo-EM density map with a resolution of 7.5 Å that retained discontinuous density for the Spc24 and Spc25 RWD domains. Signal corresponding to the Spc24 and Spc25 RWD domains was subtracted from the particle images, and the subtracted particle images were used to reconstruct a cryo-EM density map with a resolution of 7.2 Å. Two non-overlapping masks were generated for multibody refinement: one encompassed part of the CC2 region of the Mis12c^{Mtw1c} stalk domain, the CC3 region of the Mis12c^{Mtw1c} stalk domain, and the Knl1c RWD domains ('apex mask 2'), whilst the other encompassed the Mis12c^{Mtw1c} head 1 and head 2 domains, the CC1 region of the Mis12c^{Mtw1c} stalk domain, and the remaining segment of the CC2 region of the Mis12c^{Mtw1c} stalk domain ('base mask 2'). Multibody refinement using these masks reconstructed a cryo-EM density map for the Mis12c^{Mtw1c} head 1 and head 2 domains and relevant sections of the stalk domain with a global resolution (GS-FSC) of 6.5 Å ('base body 2').

Cryo-EM molecular model building

AF2 multimer structure predictions of Mis12c^{Mtw1c}:Spc24:Spc25 and Knl1c:Mis12c^{Mtw1c}, performed using full-length, wild type proteins apart from Knl1^{Spc105} (from which residues 1-444 were excluded) and Dsn1 (from which residues 1-278 were excluded), were used to build a model for the KMN junction complex. A composite map of the KMN junction complex was obtained by docking 'apex body 1' and 'base body 1' into the cryo-EM density map reconstructed by the preceding refinement and used for model building.

The AF2 structure predictions were divided into five regions for model building. 'Region one', corresponding to Spc24 and Spc25 RWD domains interacting with Mis12$^{Mtw1_Spc24\text{-}helix}$ and Dsn1$^{Cterm\text{-}helix}$ helical motifs, comprised Spc24$^{143\text{-}213}$, Spc25$^{124\text{-}221}$, Mis12$^{Mtw1_228\text{-}252}$, and Dsn1$^{556\text{-}576}$. 'Region two', corresponding to the RWD domains of ZWINT^{Kre28} and Knl1^{Spc105} interacting with the Mis12$^{Mtw1_Cterm\text{-}helix}$ and Pmf1$^{Nnf1_Cterm\text{-}helix}$ helical motifs, comprised Knl1$^{Spc105_719\text{-}917}$, ZWINT$^{Kre28_280\text{-}368}$, Mis12$^{Mtw1_274\text{-}289}$, and Pmf1$^{Nnf1_184\text{-}201}$. 'Region three', corresponding to all of the CC3 and most of the CC2 regions of the Mis12c^{Mtw1c} stalk domain, comprised Dsn1$^{483\text{-}547}$, Pmf1$^{Nnf1_139\text{-}180}$, Nsl1$^{143\text{-}216}$, and Mis12$^{Mtw1_132\text{-}222}$. 'Region four', corresponding to the remainder of the CC2 and all of the CC1 regions of the Mis12c^{Mtw1c} stalk domains, comprised Dsn1$^{431\text{-}482}$, Pmf1$^{Nnf1_115\text{-}138}$, Nsl1$^{97\text{-}142}$, and Mis12$^{Mtw1_116\text{-}131}$. 'Region 5', comprising the Mis12c^{Mtw1c} head 1 domain, comprised

898 Pmf1$^{Nnf1_1\text{-}114}$ and Mis12$^{Mtw1_1\text{-}115}$. Isolde, as implemented in Chimera X, was used to remodel
899 and refine these five regions of the AF2 structure predictions into the composite map of the
900 KMN junction complex (Croll, 2018; Goddard et al., 2018).

901 C-terminal residues of Pmf1^{Nnf1}, Mis12^{Mtw1}, Dsn1, and Nsl1 in 'region five' and 'region four'
902 were manually reconnected with the N-terminal residue of the corresponding chain in 'region
903 four' and 'region three', respectively, and refined into the density in Coot (Emsley et al.,
904 2010) to yield 'region tff'. The model comprising 'region one', 'region two', and 'region tff'
905 was subsequently refined and remodelled into the composite map using Isolde to yield the
906 final model of the KMN junction complex.

907 To build the experimental model of the *S. cerevisiae* KMN junction complex with head 2 we
908 docked the KMN junction complex (without head 2) and the AF2 prediction of the *S.*
909 *cerevisiae* Mtw1^{Mis12} head2 domain (Dsn1 residues 259-353 and Nsl1 residues 1-84), and the
910 AF2 prediction of *Kl*Mtw1^{Mis12c}, into the 6.5 Å KMN junction base body 2 cryo-EM map
911 (Figure S7C and Table S1). The *Kl*Mtw1^{Mis12c} model accounted for nearly all density in the
912 cryo-EM map (Figure 4B), whereas for the *S. cerevisiae* model of head 2, some density
913 regions were not assigned, mainly a helical-like density associated with Dsn1 head 1 (Dsn1^{AI},
914 *Sc* residues 229-255), the Dsn1 CC1-head2 linker (*Sc* residues 354-365) and the Nsl1 CC1-
915 head2 linker (*Sc* residues 85-96) (Figure S8C). We used the *Kl*Mtw1^{Mis12c} model to guide
916 complete building an experimental model of *Sc*Mtw1^{Mis12c} (Figure 4D).

917 Model refinement

918 Refinement was performed using the Phenix package (Liebschner et al., 2019) (Table S1).

919 AlphaFold2 structure predictions

920 Local installations of AlphaFold2 (Jumper et al., 2021) were used for all protein structure
921 predictions in this study. The Colabfold implementation AF2 (Mirdita et al., 2022) of AF2
922 was used for all structure predictions other than for the *Kluyveromyces lactis* Mis12c^{Mtw1c}
923 (*Kl*Mis12c^{Mtw1c}), which used the Colabfold 3 version. Unless otherwise stated, wild-type,
924 full-length protein sequences deposited in Uniprot were used for all protein structure
925 predictions.

926 Isothermal titration calorimetry experiments

927 Dsn1$^{228-254}$ and Dsn1$^{228-254,S240E,S250E}$ peptides were synthesised by Alta BioScience with N-
928 terminal acetylation and C-terminal GSAW extension and amidation. The final sequence of
929 Dsn1$^{228-254}$ was PHYIQRTRERKKSISHSQRGRRLSMLASGSAW; and Dsn1$^{228-254,S240E,S250E}$
930 was PHYIQRTRERKKSISHSQRGRRLEMLASGSAW. All protein complexes and peptides
931 used in a given experiment were dialysed for a minimum of 16 h and/or buffer exchanged by
932 size exclusion chromatography into the same batch of ITC buffer (25 mM HEPES pH 7.5,
933 100 mM NaCl, 1 mM TCEP). All experiments were performed using an Auto-iTC200
934 instrument (Malvern Instruments) at 25 ˚C. In each experiment, 360 µL of protein complex
935 was pipetted into the calorimeter cell. The protein complex loaded into the calorimeter cell
936 contained Knl1c:Mis12c^{Mtw1c} with Knl1$^{Spc105_HB-RWD}$ and Dsn1$^{\Delta 1-257}$ and either wildtype
937 Mis12^{Mtw1} (K^{HB-RWD}M$^{Dsn1\Delta 257}$) or Mis12^{Mtw1_E69A,E73A,E77A} mutant (K^{HB-RWD}M$^{Dsn1\Delta 257_Mis12-}$
938 ^{3A}). Wild-type constructs of all other Knl1c and Mis12c^{Mtw1c} subunits were included. Titration
939 of either the Dsn1$^{228-254}$ or Dsn1$^{228-254,S240E,S250E}$ peptide into the cell was then performed by
940 an additional injection of 0.5 µL, followed by 19 further injections of 2.0 µL each. Heat
941 arising from the initial injection was discarded, and the MicroCal PEAQ-ITC analysis
942 software 1.0.0.1258 (Malvern instruments) was subsequently used to fit the change in the
943 amount of heat released, integrated over the entire titration, to a single-site binding model.
944 Concentrations of the protein complex and peptide used for each experiment are provided in
945 the relevant figure panel. Titrations were performed in duplicate or triplicate and reported K_D
946 and n values were calculated as an average from all replicate results.

947 Investigation of the function of Mis12c^{Mtw1c} motifs that form interfaces with Knl1c

948 To test the effect of deleting the Mis12c^{Mtw1c} motifs that form interfaces with Knl1c on
949 Mis12c^{Mtw1c} assembly and interaction with Ndc80c, 4 µM concentration of wildtype
950 Mis12c^{Mtw1c} or one of the three Mtw1c mutants (Mis12c$^{Mtw1c_Mis12\Delta C}$, contained
951 Mis12$^{Mtw1_\Delta 272-C}$; Mis12c$^{Mtw1c_Pmf1\Delta C}$, contained Pmf1$^{Nnf1_\Delta 180-C}$; Mis12c$^{Mtw1c_Mis12\Delta C-Pmf1\Delta C}$:
952 contained Mis12$^{Mtw1_\Delta 272-C}$ and Pmf1$^{Nnf1_\Delta 180-C}$) were either individually diluted into KMN
953 buffer, or mixed with 4 µM concentration of wildtype Ndc80c in KMN buffer. Mixtures of
954 Ndc80c and wildtype or mutant Mis12c^{Mtw1c} were incubated on ice for 30 min to reconstitute
955 the complex. 100 µL of individual protein complexes or reconstitution mixtures were loaded
956 onto a Superose 6 3.2/300 size exclusion chromatography column (Cytiva) and 100 µL eluate
957 fractions were collected. Aliquots of each eluate fraction were mixed 1:1 (volume/volume)

958 with 2xLDS-PAGE loading buffer (Thermo Fisher Scientific), supplemented with DTT,
959 boiled for 3 min at 95 ˚C, and analysed by SDS-PAGE.

960 To test the effect of deleting the Mis12c^{Mtw1c} motifs that form interfaces with Knl1c on the
961 interaction between Knl1c and Mis12c^{Mtw1c}, suspension cultures of High-5 insect cells were
962 infected with one of two P3 suspension cultures, or two P3 cultures in combination, that were
963 amplifying one of two sets of viruses. The first virus encoded ZWINT^{Kre28_RWD} fused to a C-
964 terminal twin-strep-tag II and Knl1^{Spc105_RWD} fused to a N-terminal tag comprising tandem
965 maltose binding protein (MBP) and monomeric enhanced green fluorescent protein (mEGFP)
966 tags. The second set of viruses encoded either wildtype Mis12c^{Mtw1c}, or one of the
967 Mis12c$^{Mtw1c_Mis12\Delta C}$, Mis12c$^{Mtw1c_Pmf1\Delta C}$, or Mis12c$^{Mtw1c_Mis12\Delta C\text{-}Pmf1\Delta C}$ mutants. All viruses
968 encoding Mis12c^{Mtw1c} contained genes that expressed Dsn1$^{\Delta 1\text{-}278}$. The insect cell cultures
969 were harvested 48 h after infection, when cell viabilities had dropped to 70-75%.

970 All subsequent steps were performed at 4 ˚C or on ice. Cells were lysed by sonication in a
971 lysis buffer containing 50 mM HEPES pH 8.5, 200 mM NaCl, 8 mM benzamidine, 7.5%
972 glycerol, 1 mM TCEP, 0.5 mM EDTA, 0.2 mM PMSF that was supplemented with cOmplete
973 EDTA-free protease inhibitor tablets and benzonase. The lysate was cleared by
974 ultracentrifugation at 38,000 x *g* for one h in a JA-25.50 rotor. A sample of the cleared
975 supernatant was withdrawn and mixed 1:9 (volume/volume) with lysis buffer, mixed with 10
976 volume equivalents of 2xLDS-PAGE loading buffer (Thermo Fisher Scientific) supplemented
977 with DTT, and boiled for 5 min at 95 ˚C for analysis as an input sample by SDS-PAGE.
978 Cleared supernatants were subsequently filtered and incubated whilst rolling with 0.5 mL of a
979 50% slurry of Strep-Tactin Superflow plus resin (Qiagen) in a wash buffer containing 50 mM
980 HEPES pH 8.0, 200 mM NaCl, 5% glycerol, 0.5 mM EDTA, 1 mM TCEP for 90 min. Resin
981 was collected by centrifugation at 500 x *g* for 3 min and washed with 10 mL of wash buffer.
982 Resin washes were repeated, as above, a further four times. Resin was collected a final time
983 by centrifugation, as above, and bound complexes were eluted with wash buffer containing
984 2.5 mM d-desthiobiotin. The resin was collected by centrifugation, as above, and 10 µL of
985 eluate was withdrawn and mixed with an equal volume of 2xLDS-PAGE loading buffer
986 (Thermo Fisher Scientific) that was supplemented with DTT. This sample of eluate was then
987 boiled for 5 min and analysed by SDS-PAGE.

988 <u>Investigation of Dsn1 N-terminal intrinsically disordered domain function in Mis12c^{Mtw1c}</u>
989 <u>auto-inhibition</u>

990 To test the effect of deleting or mutating regions of the Dsn1 N-terminal disordered domain
991 on Mis12c^{Mtw1c} auto-inhibition, 4 μM concentrations of Knl1c:Mis12c^{Mtw1c} complexes
992 containing Knl1$^{Spc105_HB\text{-}RWD}$ and different Dsn1 constructs were mixed with 4 μM
993 concentrations of either CENP-C$^{Mif2_1\text{-}63}$ or CENP-QU in KMN buffer. Knl1c:Mis12c^{Mtw1c}
994 complexes used contained one of the following Dsn1 constructs: K^{HBRWD}M, contained full-
995 length and wildtype Dsn1; K$^{HB\text{-}RWD}$M^{S240E,S250E}, contained Dsn1^{S240E,250E}; K$^{HB\text{-}RWD}$M$^{Dsn1\Delta226}$,
996 contained Dsn1$^{\Delta1\text{-}226}$; K$^{HB\text{-}RWD}$M$^{Dsn1\Delta257}$, contained Dsn1$^{\Delta1\text{-}257}$; K$^{HB\text{-}RWD}$M$^{Dsn1\Delta226,S240E,S250E}$,
997 contained Dsn1$^{\Delta1\text{-}226,S240E,S250E}$. Protein mixtures were incubated together on ice for 30 min to
998 attempt to reconstitute a protein complex. 100 μL of individual proteins or protein complexes
999 or reconstitution mixtures were loaded onto a Superose 6 3.2/300 size exclusion
1000 chromatography column (Cytiva) and 100 μL eluate fractions were collected. Aliquots of
1001 each indicated eluate fraction was mixed 1:1 (volume/volume) with 2xLDS-PAGE loading
1002 buffer supplied by Thermo Fisher Scientific, supplemented with DTT, boiled for 3 min at 95
1003 °C, and analysed by SDS-PAGE.

1004 Yeast strain construction

1005 Yeast strains constructed for this study are listed in Table S2. To construct strains encoding
1006 Mis12^{Mtw1}-mAID$_3$-FLAG$_5$ or Pmf1^{Nnf1}-mAID$_3$-FLAG$_5$, a degron cassette encoding mAID$_3$-
1007 FLAG$_5$ and a KanMX gene that provided resistance to G418 were amplified from plasmid
1008 pST1933 (Tanaka et al., 2015) through a polymerase chain reaction (PCR) that used Q5
1009 polymerase and oligonucleotide primers containing 48 bp 5' extensions with homology to the
1010 relevant locus in the yeast genome. BY26972 strain yeast cells (Table S2) from an
1011 exponentially growing suspension culture were transformed with the cassette according to the
1012 previously detailed LiAc protocol (Gietz and Schiestl, 2007). In brief, cells were harvested by
1013 centrifugation, washed thrice with sterile Millipore water (MPW), and incubated with 360 μL
1014 transformation buffer (100 mM lithium acetate, 33% PEG 3350, 100 μg salmon sperm DNA)
1015 containing the degron cassette. Cells were transformed with the cassette through a 45 min
1016 heat shock at 42 °C, and allowed to recover by standing in 1 mL of YEPD medium for 3 h at
1017 22 °C. Transformants were then selected by plating yeast cells on YEPD agar containing 500
1018 μg/mL G418 (Sigma, A1720-5G) and grown at 30 °C for 3–4 days. Individual colonies were
1019 picked and restreaked on fresh YEPD agar containing 500 μg/mL G418 twice, successively.
1020 Integration of the cassette was then screened by PCR amplification using Q5 polymerase and
1021 two primers directed against the 3' end of the relevant gene and an internal region of the

1022 degron cassette. PCR products obtained by this method were sequenced to validate in-frame
1023 integration of the $mAID_3$-$FLAG_5$ tags at the 3' end of the relevant gene.

1024 Strains expressing $Mis12^{Mtw1}$-$mAID_3$-$FLAG_5$ or $Pmf1^{Nnf1}$-$mAID_3$-$FLAG_5$ and an allele to be
1025 tested for its ability to rescue cell death were constructed as follows. Yeast strains expressing
1026 $Mis12^{Mtw1}$-$mAID_3$-$FLAG_5$ or $Pmf1^{Nnf1}$-$mAID_3$-$FLAG_5$ were transformed, as above, with
1027 *pRS304* (encoding *MTW1* alleles) or *pRS305* (encoding *NNF1* alleles) plasmids that were
1028 cleaved with a restriction enzyme in a single site within the *LEU2* (*pRS304* plasmids) or
1029 *TRP1* (*pRS305* plasmids) selection marker. The plasmids contained the following alleles
1030 encoding the listed gene products: *MTW1*, full-length and wildtype $Mis12^{Mtw1}$; $mtw1^{\Delta C}$,
1031 $Mis12^{Mtw1_\Delta 272\text{-}C}$, *NNF1*, full-length and wildtype $Pmf1^{Nnf1}$; $nnf1^{\Delta C}$, $Pmf1^{Nnf1_\Delta 180\text{-}C}$.
1032 Transformants were selected for by plating yeast cells on leucine dropout (*MTW1* or $mtw1^{\Delta C}$
1033 transformants) or tryptophan dropout (*NNF1* or $nnf1^{\Delta C}$ transformants) agar media containing
1034 500 μg/mL G418. Integration of the cassette at the *LEU2* or *TRP1* locus was screened using
1035 two PCR reactions that amplified across the 5' and 3' recombination junctions. The first PCR
1036 used a pair of oligonucleotide primers targeted against a region of the genome 5' of *LEU2* or
1037 *TRP1* and against an internal region of the integrated cassette, and the second PCR used a
1038 pair of primers targeted against a region of the genome 3' of *LEU2* or *TRP1* and against
1039 another internal region of the cassette. Positive transformants were stored in 50% glycerol at -
1040 80 °C for later use.

1041 Auxin depletion assays

1042 10 mL suspension cultures of each yeast strain were grown overnight at 30 °C. The optical
1043 density at 600 nm of each suspension culture was measured in triplicate, yeast cells were
1044 subsequently diluted to $OD_{600nm} = 0.1$, and then serially diluted 1:9 (volume/volume) over 4
1045 further dilutions. 4 μL of each dilution was then applied to agar plates containing either
1046 YEPD medium, or YEPD medium and 0.5 mM indole-3-acetic acid (IAA). Cells were grown
1047 at 30 °C for 3 days and imaged.

1048 Western blotting

1049 To validate expression levels of the gene products of the $Mis12^{Mtw1}$ and $Pmf1^{Nnf1}$ alleles
1050 integrated at ectopic sites, 40 mL of each cell culture was grown in YEPD until the culture
1051 reached an OD_{600nm} between 0.7 and 2.0. At this point, $1x10^7$ ($Mis12^{Mtw1}$-$mAID_3$-$FLAG_5$

1052 strains) or $1.4x10^7$ ($Pmf1^{Nnf1}$-$mAID_3$-$FLAG_5$) cells were withdrawn from the culture and
1053 processed for western blotting as described below.

1054 Depletion of $Mis12^{Mtw1}$-$mAID_3$-$FLAG_5$ and $Pmf1^{Nnf1}$-$mAID_3$-$FLAG_5$ by addition of IAA was
1055 monitored and validated by growing 40 mL suspension cultures of each strain in YEPD
1056 medium until the culture attained an OD_{600nm} of between 0.7 and 2.0. This was followed by
1057 addition of either IAA to a final concentration of 0.5 mM, or of an equal volume of phosphate
1058 buffered saline (PBS) as a negative control. A volume of suspension culture containing $1x10^7$
1059 ($Mis12^{Mtw1}$-$mAID_3$-$FLAG_5$ strains) or $1.4x10^7$ ($Pmf1^{Nnf1}$-$mAID_3$-$FLAG_5$) cells was then
1060 withdrawn from each culture at the indicated time points and processed for western blotting
1061 as described below.

1062 All subsequent steps were performed at 22 ˚C, unless otherwise indicated. Yeast cells were
1063 collected by centrifugation at 3,000 x *g* for 3 min, resuspended in 1 mL of sterile Millipore
1064 water (MPW), and pelleted by centrifugation at 12,000 x *g* for 1 min. Whole cell extracts
1065 were then prepared by incubation of the cell pellets in 50 µL of 0.2 M NaOH for 5 min,
1066 centrifugation for 1 min at 12,000 x *g*, a wash of the cell pellet with 1 mL of MPW, and a
1067 final collection of the pellet by centrifugation as above. Pellets were then boiled for 3 min at
1068 95 ˚C in 50 µL of 1xLDS-PAGE loading buffer supplemented with DTT. The pellet was
1069 collected by centrifugation, and 10 µL of each supernatant was applied to an SDS-PAGE gel
1070 to separate proteins through application of a constant 210 V for 45 min. Proteins were
1071 transferred from the SDS-PAGE gel onto a TransBlot Turbo minigel membrane using a
1072 Trans-blot Turbo transfer system. Membranes were blocked with 3% milk suspension
1073 ($Pmf1^{Nnf1}$ blots) or 5% milk suspension ($Mis12^{Mtw1}$ blots) in PBS-T (Phosphate buffered
1074 saline containing 0.2% Tween-20) for 30 min at 22 ˚C. Membranes were then probed with the
1075 primary antibody detailed below overnight at 4 ˚C in PBS-T to detect the protein of interest.
1076 To detect $Mis12^{Mtw1}$-$mAID_3$-$FLAG_5$ and $Pmf1^{Nnf1}$-$mAID_3$-$FLAG_5$, a 1:1000
1077 (volume/volume) dilution of anti-FLAG antibody (Cell Signalling, D6W5B) was used. To
1078 detect $Pmf1^{Nnf1}$-$V5_3$ or $Mis12^{Mtw1}$-HA_3 expressed from the ectopically integrated loci, 1:3333
1079 dilutions of anti-V5 (Proteintech, 14440-1-AP) or anti-HA (Abcam, ab1424) antibodies,
1080 respectively, were used. To detect alpha tubulin as a loading control, anti-α-tubulin (Bio-Rad,
1081 MCA78G) antibody was used.

1082 Membranes were washed four times with PBS-T before incubation with a 1:3333
1083 (volume/volume) dilution of HRP-conjugated secondary antibody in PBS-T by rolling at 21

1084 °C for 1.5–2.5 h. Membranes were washed a further four times with PBS-T before
1085 visualisation of the secondary antibody using chemiluminescence using the ECL Prime
1086 Western blotting detection kit (Amersham) and imaging using a ChemiDoc imaging system
1087 (Bio-Rad).

1088 Surface Plasmon Resonance

1089 SPR was performed using a Biacore T200 using CM5-sensor chips (Cytiva). Both reference
1090 control and analyte channels were equilibrated HBS-P buffer (Cytiva) and Strep-TactinXT
1091 (IBA Lifesciences GmbH) was immobilised *via* amide coupling using the supplied kit
1092 (Cytiva) to a level of approximately 2350 RU. The chip was then primed in running buffer
1093 (20 mM HEPES pH 7.5, 150 mM NaCl, 1 mM TCEP). Either 10 ng/µL of CENP-QU or 2
1094 ng/µL of CENP-$C^{Mif2_1\text{-}63}$ was captured on the second flow cell during each cycle to level of
1095 approximately 1000 RU or 200 RU respectively. Analytes E2 and FL were then injected over
1096 both channels for 120 s followed by dissociation for 900 s for CENP-QU or 600s for CENP-
1097 $C^{Mif2_1\text{-}63}$ in a 1:2 dilution series with initial concentrations of 1 µM. The surface was
1098 regenerated by a 60 s injection of 3 M guanidinium chloride. After reference and buffer signal
1099 correction, sensorgram data were fitted using Biacore Evaluation Software Version 1.0
1100 (Cytiva) or Prism 10.4.1 (GraphPad Software Inc) using a single site or heterogenous ligand
1101 model.

1102 Multiple sequence alignment

1103 Multiple sequence alignments were performed with Clustal Omega using default settings and
1104 sequences full-length, wildtype protein sequences deposited in Uniprot unless otherwise
1105 indicated (Sievers et al., 2011). Sequence alignments were visualised using the Jalview
1106 workbench using a conservation score of 10 (Waterhouse et al., 2009).

1107 Crosslinking mass-spectrometry

1108 Protein cross linking reactions on the *S. cerevisiae* $K^{HB\text{-}RWD}M$ complex (100 µL at 0.5
1109 mg/mL) were carried out with sulfo-SDA (2 mM concentration). Sulfo-SDA and the protein
1110 complex were mixed and incubated on ice for 5 min before being cross linked for 10 sec with
1111 365 nm UV radiation from a home build UV LED setup. Crosslinking reactions were
1112 quenched with the addition of ammonium bicarbonate to a final concentration of 50 mM. The
1113 quenched solution was reduced with 5 mM DTT and alkylated with 20 mM iodoacetamide.
1114 The SP3 protocol, as described (Batth et al., 2019; Hughes et al., 2019), was used to clean-up

1115 and buffer exchange the reduced and alkylated protein. In brief, for the SP3 protocol; proteins
1116 are washed with ethanol using magnetic beads for protein capture and binding. The proteins
1117 were resuspended in 100 mM NH_4HCO_3 and were digested with trypsin (Promega, UK) at an
1118 enzyme-to-substrate ratio of 1:20, and protease max 0.1% (Promega, UK). Digestion was
1119 carried out overnight at 37 ˚C. Clean-up of peptide digests was carried out with HyperSep
1120 SpinTip P-20 (Thermo Fisher Scientific) C18 columns, using 60% Acetonitrile as the elution
1121 solvent. Peptides were then evaporated to dryness *via* Speed Vac Plus (Savant, USA).

1122 Dried peptides were resuspended in 30% acetonitrile and were fractionated *via* SEC using a
1123 Superdex 30 Increase 3.2/300 column (Cytiva) at a flow rate of 20 µL/min using 30% (v/v)
1124 ACN 0.1 % (v/v) TFA as a mobile phase. Fractions are taken every 5 min, and the 2nd to 7th
1125 fractions containing cross linked peptides are collected. Dried peptides were suspended in 3%
1126 (v/v) acetonitrile and 0.1 % (v/v) formic acid and analysed by nano-scale capillary LC-
1127 MS/MS using an Ultimate U3000 HPLC to deliver a flow of 300 nL/min. Peptides were
1128 trapped on a C18 Acclaim PepMap100 5 µm, 0.3 µm x 5 mm cartridge (Thermo Fisher
1129 Scientific) before separation on Aurora Ultimate C18, 1.7 µm, 75 µm x 25 cm (Ionopticks,
1130 Melbourne). Peptides were eluted on optimised gradients of 90 min and interfaced *via* an
1131 EasySpray ionisation source to a tribrid quadrupole Orbitrap mass spectrometer (Orbitrap
1132 Eclipse, Thermo Fisher Scientific) equipped with FAIMS. MS data were acquired in data
1133 dependent mode with a Top-25 method, high resolution scans full mass scans were carried
1134 out (R = 120,000, *m/z* 400 – 1550) followed by higher energy collision dissociation (HCD)
1135 with stepped collision energy range 21, 30, 34 % normalised collision energy. The tandem
1136 mass spectra were recorded (R=60,000, isolation window *m/z* 1, dynamic exclusion 50 s).
1137 Mass spectrometry measurements were cycled for 3 s durations between FAIMS CV -45, and
1138 -60 V.

1139 <u>Crosslinking mass-spectrometry data analysis</u>

1140 Xcalibur raw files were converted to MGF files using ProteoWizard and cross links were
1141 analysed by XiSearch (Chambers et al., 2012; Mendes et al., 2019). Search conditions used 3
1142 maximum missed cleavages with a minimum peptide length of 5. Variable modifications used
1143 were carbmidomethylation of cysteine (57.02146 Da) and methionine oxidation (15.99491
1144 Da). False discovery rate was set to 5%. Crosslinking mass-spectrometry data was visualised
1145 and analysed using XiVIEW (Combe et al., 2024).

1146 <u>Computational methods</u>

The UCSF Chimera-X package was used to visualise cryo-EM density maps, AF2 structure predictions, previously deposited structures retrieved from the protein data bank, and crosslinking mass-spectrometry data superimposed onto the structural models (Goddard et al., 2018; Pettersen et al., 2021).

Acknowledgments.

We are grateful to the LMB EM Facility for help with the EM data collection; J. Grimmett, T. Darling and I. Clayson for scientific computing; J. Shi and K. Turton for help with insect cell expression; and to T. Dendooven, D. Kimanius and S. Yatskevich for discussions. For the purpose of open access, the authors have applied a CC BY public copyright license to any Author Accepted Manuscript version arising.

Funding.

UKRI/Medical Research Council MC_UP_1201/6 (D.B.)

Cancer Research UK C576/A25675 (D.B.)

Cancer Research UK C576/A14109 (D.B.): CR-UK PhD studentship (N.N.T).

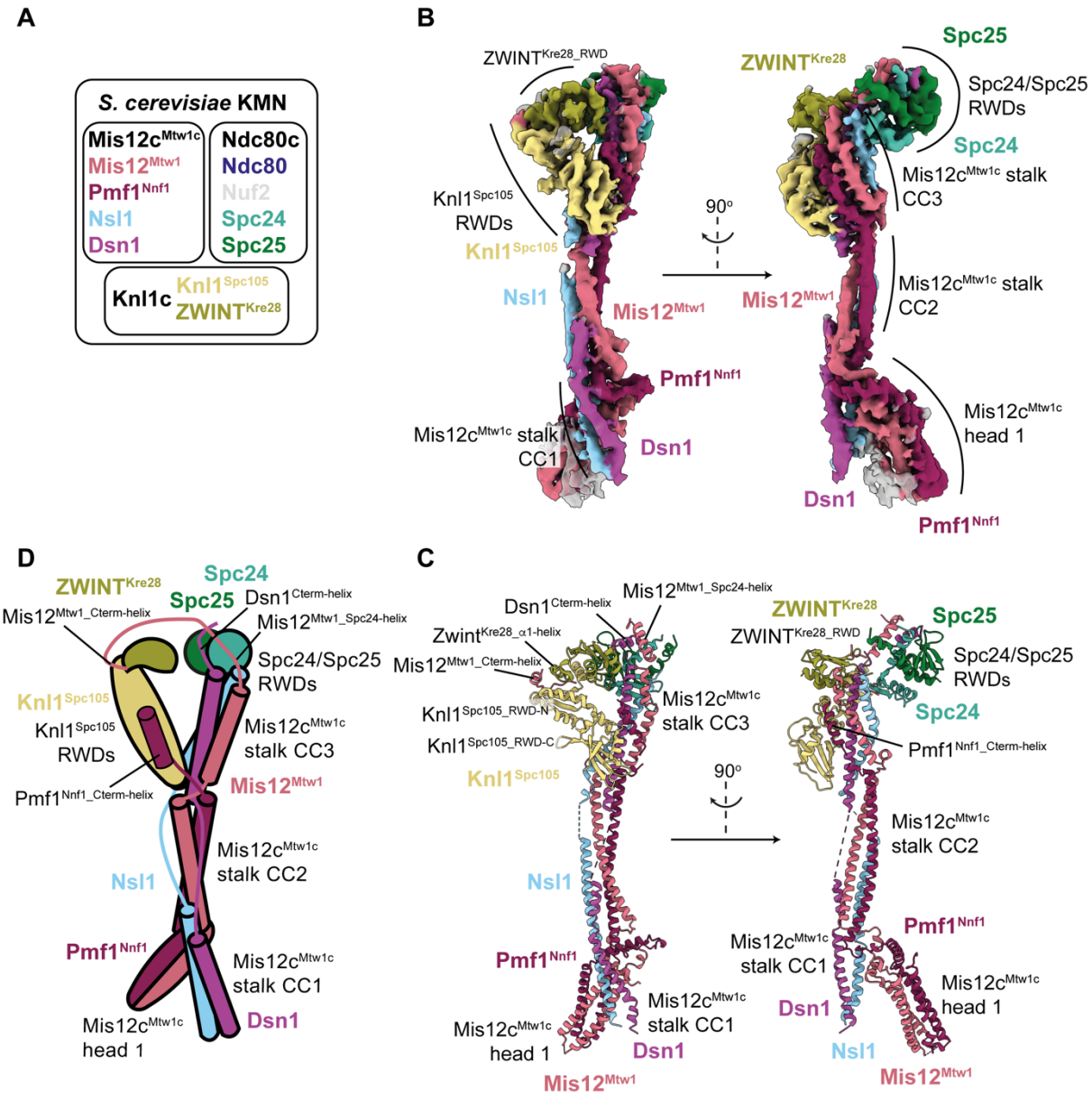

Figure 1: Overall organisation of the *S. cerevisiae* KMN junction complex

A) Subcomplex and subunit composition of the *S. cerevisiae* KMN complex. **B)** Composite cryo-EM density map of the *S. cerevisiae* KMN junction complex derived from docking the apex and base bodies (Figure S2Diii) into the consensus density map. **C)** Model of the KMN junction complex, highlighting the motifs that mediate the interactions between Mis12c^{Mtw1c} and Knl1c or Ndc80c. **D)** Schematic representation of the KMN junction complex, portraying the organisation of protein domains and the motifs that mediate interactions between Mis12c^{Mtw1c} and Knl1c or Ndc80c.

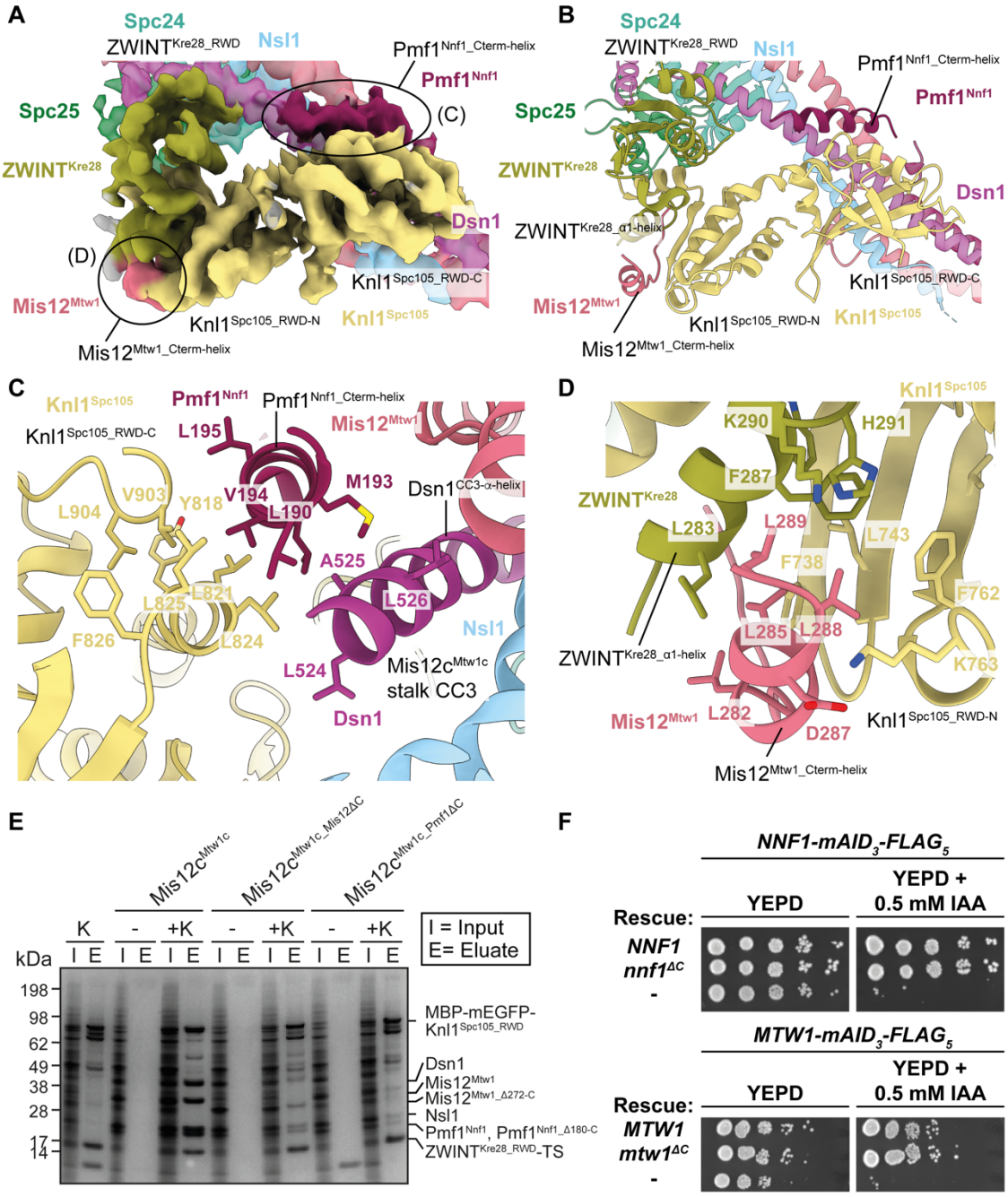

Figure 2: Structural details of the interactions between Mis12c^{Mtw1c} and Knl1c

Cryo-EM density map (Figure S2Diii) highlighting the interactions between Mis12c^{Mtw1c} and Knl1c. (C) and (D) highlight regions of the map that are shown close up in panels **C** and **D**. **B)** Model of Knl1c engaging in interactions with motifs from Mis12c^{Mtw1c}, highlighting the Mis12$^{Mtw1_Cterm\text{-}helix}$ and Pmf1$^{Nnf1_Cterm\text{-}helix}$ motifs from Mis12c^{Mtw1c} that interact with the Knl1$^{Spc105_RWD\text{-}N}$ and Knl1$^{Spc105_RWD\text{-}C}$ domains, respectively. **C)** Structural details of the interaction between the Pmf1$^{Nnf1_Cterm\text{-}helix}$ helix, the hydrophobic patch on the Knl1$^{Spc105_RWD\text{-}C}$ domain, and the Dsn1$^{CC3_\alpha\text{-}helix}$. **D)** Structural details of the interaction between the Mis12$^{Mtw1_Cterm\text{-}helix}$ and the interface formed by the ZWINT^{Kre28_RWD} and Knl1$^{Spc105_RWD\text{-}N}$ domains. **E)** Pulldown experiment to investigate the role of the Mis12$^{Mtw1_Cterm\text{-}helix}$ and Pmf1$^{Nnf1_Cterm\text{-}helix}$ helical motifs in mediating the interaction between Knl1c and Mis12c^{Mtw1c}. Knl1c composed of Knl1^{Spc105_RWD} and ZWINT^{Kre28_RWD} containing a C-terminal twin-strep-tag II (K^{RWD}) was coexpressed with Mis12c^{Mtw1c} in insect cells. I = input, E = eluate, K = K^{RWD} complex present, - = K^{RWD} complex absent, Mis12$^{Mtw1_\Delta C}$ = Mis12$^{Mtw1_\Delta 272\text{-}C}$, Pmf1$^{Nnf1_\Delta C}$ = Pmf1$^{Nnf1_\Delta 180\text{-}C}$.

Experimental details are provided in Materials and methods. **F)** Analysis of *mtw1*$^{\Delta C}$ and *nnf1*$^{\Delta C}$ mutants in yeast strain backgrounds with endogenous *MTW1* and *NNF1* gene products translationally fused to mAID$_3$-FLAG$_5$ tag. Cell growth was investigated by plating 1:9 serial dilutions onto either YEPD plates or YEPD plates supplemented with 0.5 mM Indole-3-acetic acid (IAA). - = no rescue allele was expressed. mAID = monomeric auxin inducible degron.

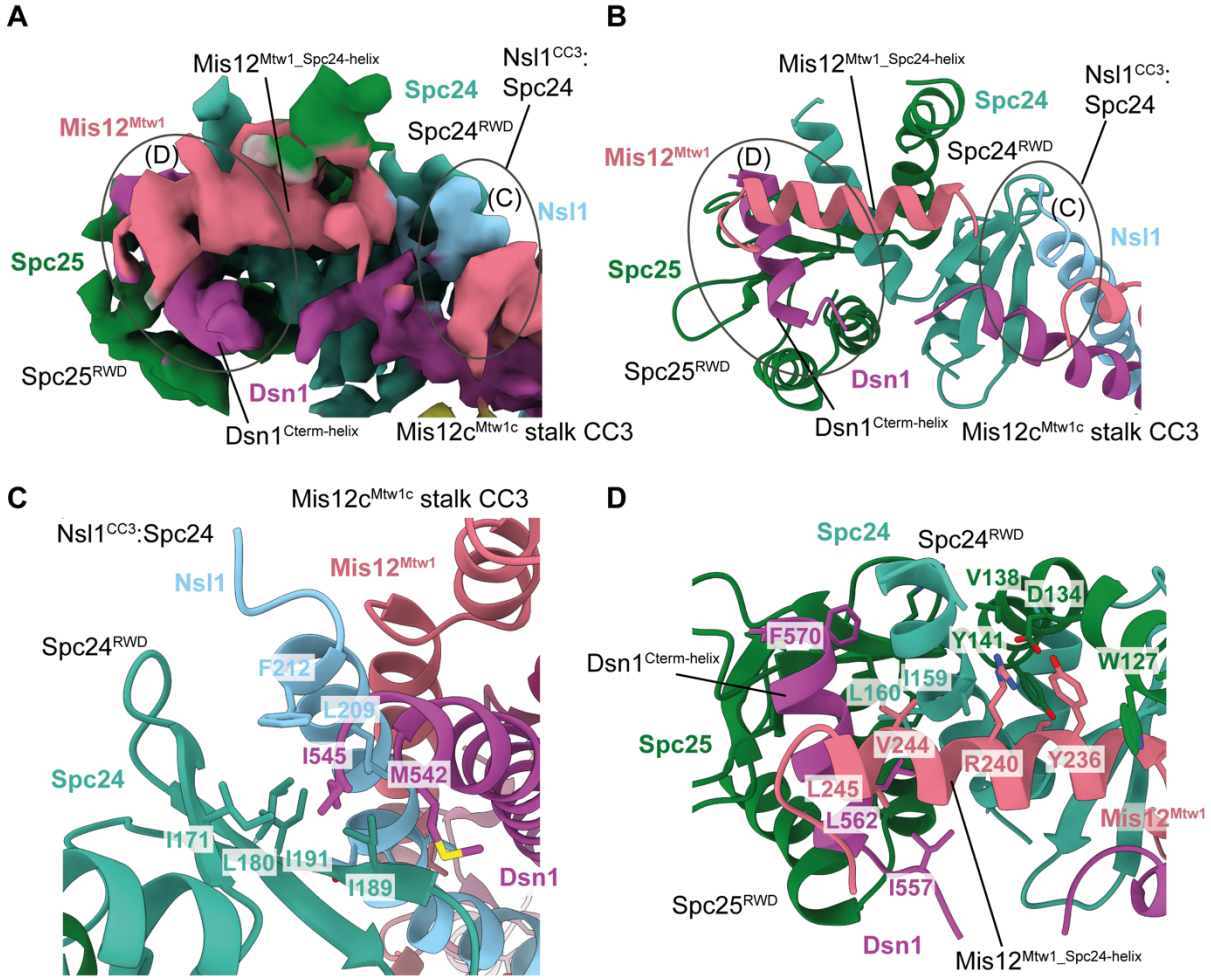

Figure 3: Structural details of interactions between Ndc80c and Mis12c^{Mtw1c}

A) Cryo-EM density map (Figure S2Diii) highlighting the interactions between Mis12c^{Mtw1c} and Spc24 and Spc25 RWD domains. (C) and (D) highlight regions of the map that are shown close up in panels C and D. **B)** Model of Spc24 and Spc25 RWD domains interacting with motifs from Mis12c^{Mtw1c} , highlighting the Mis12$^{Mtw1_Spc24\text{-}helix}$ and Dsn1$^{Cterm\text{-}helix}$ helical motifs from Mis12c^{Mtw1c} that interact with Spc24 and Spc25 RWD domains. The interaction between the CC3 region of the Mis12c^{Mtw1c} stalk domain and the Spc24 RWD domain is also featured. **C)** Structural details of the interactions between the CC3 region of the Mis12c^{Mtw1c} stalk domain and the solvent exposed hydrophobic patch on the Spc24 RWD domain. **D)** Structural details of the interactions between Dsn1$^{Cterm\text{-}helix}$ and Mis12$^{Mtw1_Spc24\text{-}helix}$ motifs and the Spc24 and Spc25 RWD domains.

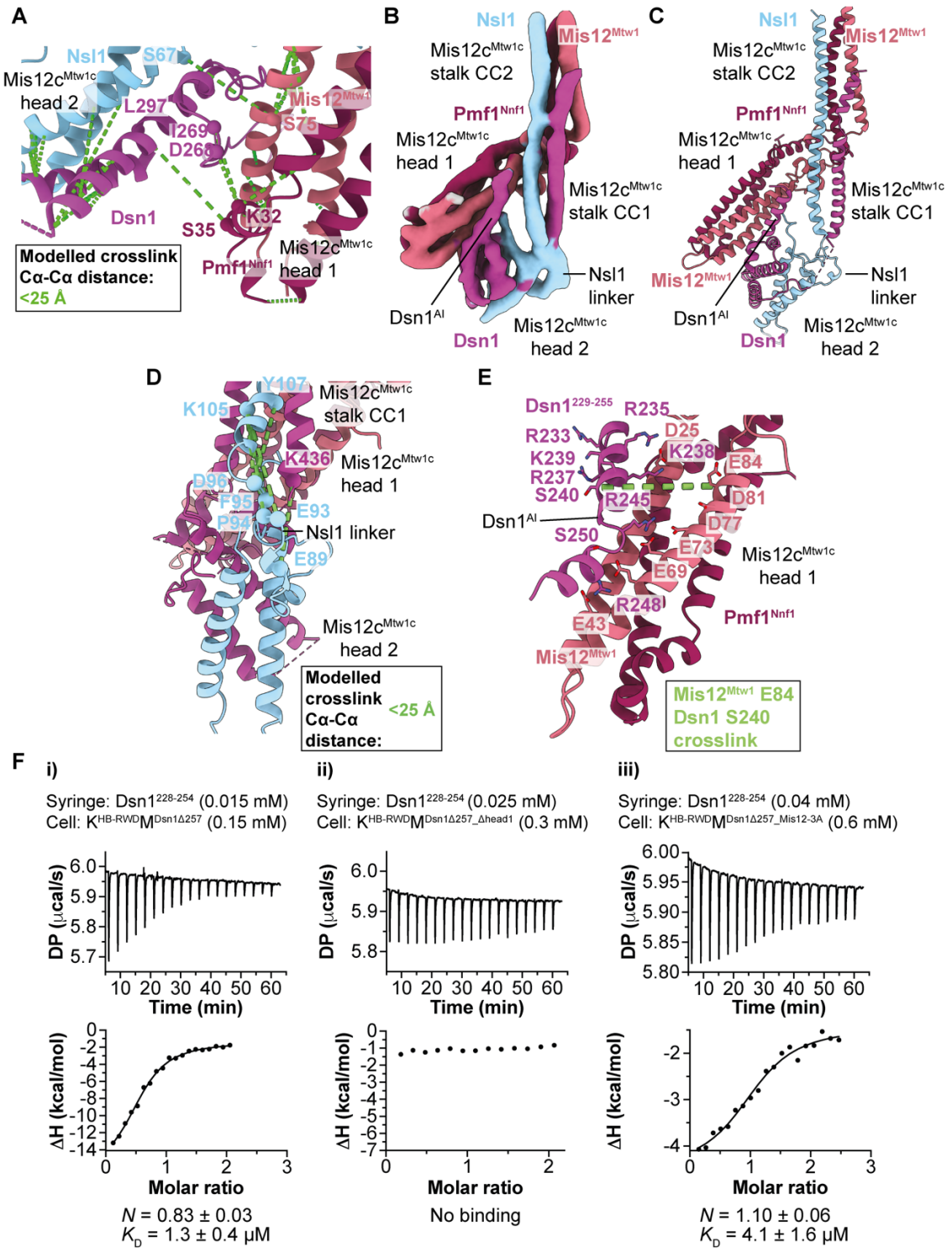

Figure 4: Interactions between the Mis12c^{Mtw1c} head 1 and head 2 domains

A) Observed CL-MS crosslinks on the K^{HB-RWD}M complex, visualised using the molecular model from **Figure S8B.** Inter-subunit crosslinks between residues in the Mis12c^{Mtw1c} head 1 and head 2 domains are highlighted, and relevant Cα atoms of crosslinked residues are shown as spheres. Crosslinks shown are between residues that satisfy the physical distance constraint of the chemical crosslinker. Crosslinks between two residues are only displayed if both residues are visible in the panel. **B)** Cryo-EM density map with improved occupancy for the Mis12c^{Mtw1c} head 2 domain (Figure S7), interpreted and colour-coded according to experimental model of *Sc*Mis12c^{Mtw1c}. **C)**

Experimental model of *Sc*Mis12c^{Mtw1c} head 1 and head 2 domains with Dsn1 auto-inhibitory region (Dsn1^{AI}) at the base of the *Sc*Mis12c^{Mtw1c} stalk domain. **D)** CL-MS cross-links from the *Sc*Mis12c^{Mtw1} dataset that satisfy the physical distance constraint of the chemical crosslinker, indicated in green, mapped onto *Sc*Mis12c^{Mtw1c} head 1, head 2 and stalk domains and Dsn1^{AI}. **E)** Molecular model showing the interaction between the *Sc*Mis12c^{Mtw1c} head 1 domain and Dsn1^{AI} (residues 229-255). *Sc*Mis12c^{Mtw1c} head 2 domain is hidden. **F)** Isothermal titration calorimetry experiments to determine the identity of the unassigned α-helical-like density. K_D and n values are an average from **i)** three experiments, or **ii)** from two experiments. **i)** Titration of Dsn1$^{228-254}$ peptide to Knl1c:Mis12c^{Mtw1c} complex (K^{HB-RWD}M$^{Dsn1\Delta257}$) with Knl1^{Spc105} residues 1-444 and Dsn1 residues 1-257 deleted. **ii)** Titration of Dsn1$^{228-254}$ peptide to a head 1 deleted Knl1c:Mis12c^{Mtw1c} complex (K^{HB-RWD}M$^{Dsn1\Delta257_\Delta head1}$): Knl1^{Spc105} residues 1-444, Dsn1 residues 1-257, Mis12^{Mtw1} residues 1-106, and Pmf1^{Nnf1} residues 1-104 deleted. **iii)** Titration of Dsn1$^{228-254}$ peptide to K^{HB-RWD}M$^{Dsn1\Delta257}$ complex (K^{HB-RWD}M$^{Dsn1\Delta257_Mis12-3A}$) containing mutant Mis12^{Mtw1_E69A,E73A,E77A}.

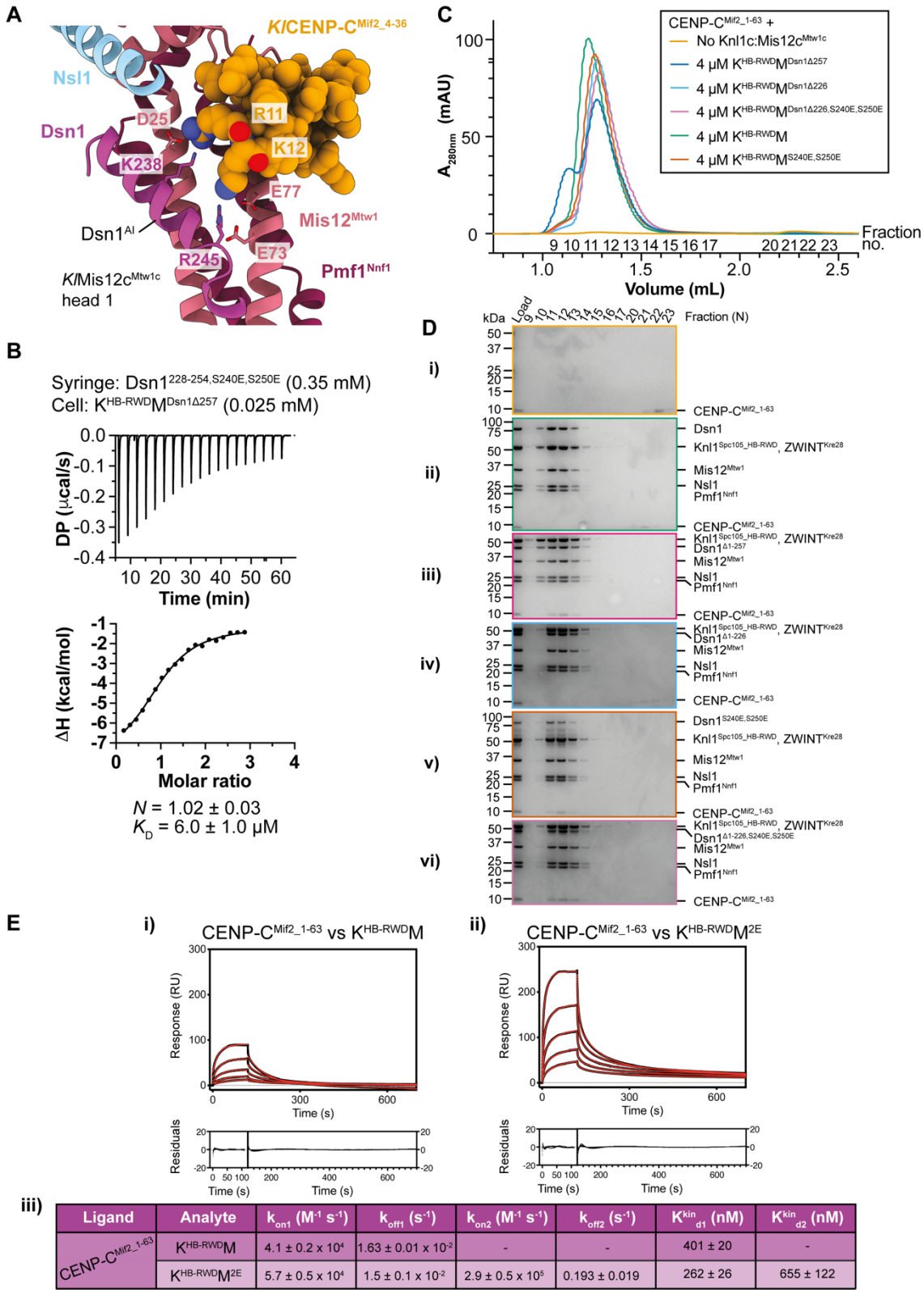

Ligand	Analyte	k_{on1} (M^{-1} s^{-1})	k_{off1} (s^{-1})	k_{on2} (M^{-1} s^{-1})	k_{off2} (s^{-1})	K^{kin}_{d1} (nM)	K^{kin}_{d2} (nM)
CENP-CMif2_1-63	KHB-RWDM	4.1 ± 0.2 x 10^4	1.63 ± 0.01 x 10^{-2}	-	-	401 ± 20	-
	KHB-RWDM2E	5.7 ± 0.5 x 10^4	1.5 ± 0.1 x 10^{-2}	2.9 ± 0.5 x 10^5	0.193 ± 0.019	262 ± 26	655 ± 122

Figure 5: Regulation of Mis12c^{Mtw1c} auto-inhibition by Aurora B kinase and its effect on the interaction with CENP-C^{Mif2}

A) Structural alignment of the crystal structure of *Kluyvermoces lactis* CENP-C^{Mif2} residues 4-36 (*Kl*CENP-C$^{Mif2_4-36}$) bound to the *Kl*Mis12c^{Mtw1c} head 1 domain (PDB 5T59) (Dimitrova et al., 2016) to the experimental model of *Sc*Mis12c^{Mtw1c} (this study). The models are coloured by chain; Mis12^{Mtw1} and Pmf1^{Nnf1} are coloured identically in 5T59 and our experimentally determined model. *Kl*CENP-

$C^{Mif2_4\text{-}36}$ is shown in space filling representation to highlight lack of steric clash, and overlapping binding site, with $Dsn1^{AI}$. **B)** Isothermal titration calorimetry data for phosphomimetic mutations at Aurora B sites in $Dsn1^{228\text{-}254}$. K_D and n values are an average from two experiments. Titration of $Dsn1^{228\text{-}254}$ peptide with S240E and S250E phosphomimetic mutations ($Dsn1^{228\text{-}254,S240E,S250E}$) to Knl1c:Mis12c^{Mtw1c} complex ($K^{HB\text{-}RWD}M^{Dsn1\Delta257}$) with $Knl1^{Spc105}$ residues 1-444 and Dsn1 residues 1-257 deleted. **C)** SEC elution chromatograms of attempts to reconstitute the interaction between Knl1c:Mis12c^{Mtw1c} complexes containing different Dsn1 N-terminal truncation and/or phosphomimetic mutants and CENP-C^{Mif2} residues 1-63 (CENP-$C^{Mif2_1\text{-}63}$). **D)** Coomassie brilliant blue stained SDS-PAGE gels of the chromatograms shown in panel **C**. **C-D)** $K^{HB\text{-}RWD}M$ = Full-length Dsn1. $K^{HB\text{-}RWD}M^{2E}$ = Full-length Dsn1 containing $Dsn1^{S240E}$ and $Dsn1^{S250E}$ phosphomimetic mutations. $K^{HB\text{-}RWD}M^{Dsn1\Delta257}$ = Dsn1 residues 1-257 are deleted ($Dsn1^{\Delta1\text{-}257}$). $K^{HB\text{-}RWD}M^{Dsn1\Delta226}$ = Dsn1 residues 1-226 are deleted ($Dsn1^{\Delta1\text{-}226}$). $K^{HB\text{-}RWD}M^{Dsn1\Delta226\text{-}2E}$ = Dsn1 residues 1-226 are deleted and $Dsn1^{S240E}$ and $Dsn1^{S250E}$ phosphomimetic mutations ($Dsn1^{\Delta1\text{-}226,S240E,S250E}$). **E)** Surface plasmon resonance (SPR) measurements of the association and dissociation kinetic rate constants for interactions between Knl1c:Mis12c^{Mtw1c} complexes and CENP-$C^{Mif2_1\text{-}63}$. SPR sensorgrams for **i)** $K^{HB\text{-}RWD}M$ (containing full-length, wildtype Dsn1), and **ii)** $K^{HB\text{-}RWD}M^{2E}$ (containing full-length Dsn1 with $Dsn1^{S240E}$ and $Dsn1^{S250E}$ phosphomimetic mutations) binding to CENP-$C^{Mif2_1\text{-}63}$. **iii)** Table summarising $K^{HB\text{-}RWD}M$ and $K^{HB\text{-}RWD}M^{2E}$ association (k_{on}) and dissociation constants (k_{off}) for CENP-$C^{Mif2_1\text{-}63}$, where K^{kin}_d, kinetic dissociation constant = k_{on}/k_{off}.

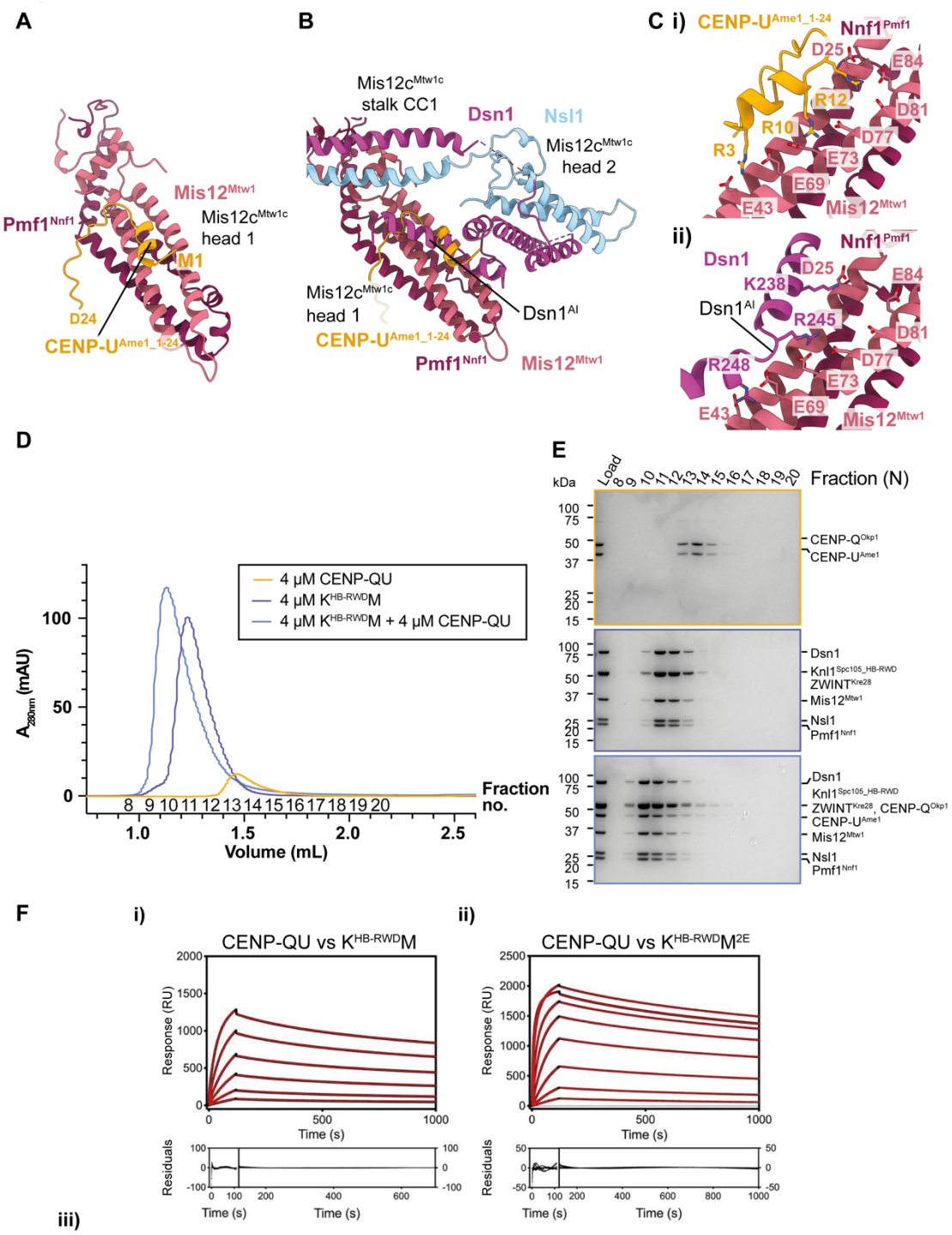

Ligand	Analyte	k_{on1} (M^{-1} s^{-1})	k_{off1} (s^{-1})	k_{on2} (M^{-1} s^{-1})	k_{off2} (s^{-1})	K^{kin}_{d1} (nM)	K^{kin}_{d2} (nM)
CENP-QU	K^{HB-RWD}M	2.3 ± 0.2 x 10^4	2.5 ± 0.1 x 10^{-4}	1.3 ± 0.2 x 10^5	3.2 ± 0.2 x 10^{-3}	10.9 ± 1.0	23.8 ± 3.6
	K^{HB-RWD}M^{2E}	3.2 ± 0.2 x 10^5	1.9 ± 0.2 x 10^{-4}	4.6 ± 0.5 x 10^4	2.4 ± 0.2 x 10^{-3}	0.59 ± 0.13	52.6 ± 6.6

Figure 6: Effect of Mis12c^{Mtw1c} auto-inhibition on the interaction with CENP-QU

A) AF2 structure prediction of the interaction between *S. cerevisiae* Mis12c^{Mtw1c} and CENP-QU coloured by chain, showing only the Mis12c^{Mtw1c} head 1 domain and residues 1-24 of CENP-U^{Ame1}. The structure prediction was performed using full-length and wildtype proteins apart from Dsn1, from which Dsn1 residues 1-257 were excluded to avoid Mis12c^{Mtw1c} auto-inhibition. **B)** Superimposition of the AF2 model presented in Figure 6A onto the experimental model of *Sc*Mis12c^{Mtw1c} (this study). The subunits are coloured by chain; Mis12^{Mtw1} and Pmf1^{Nnf1} are coloured identically in both the AF2 model and in the experimentally determined model. The apparent steric clash between CENP-U^{Ame1}

residues 1-24 and Dsn1^{AI} is highlighted. **C)** Comparison of the AF2 model of CENP-U^{Ame1} bound to *Sc*Mis12c^{Mtw1c} (top panel) and Dsn1^{AI} of *Sc*Mis12c^{Mtw1c} (bottom panel). Both CENP-U^{Ame1} and Dsn1^{AI} form basic α-helices that engage the acid patch of head 1. **D)** SEC elution chromatograms of CENP-QU alone, Knl1c:Mis12c^{Mtw1c} complexes that lack residues 1–444 of Knl1^{Spc105} alone (K^{HB-RWD}M), or after reconstitution of the interaction between CENP-QU and K^{HB-RWD}M. **E)** Coomassie brilliant blue stained SDS-PAGE gels of the experiments of the experiments in panel **D**. **F)** Measurement of the association and dissociation kinetic rate constants for interactions between Knl1c:Mis12c^{Mtw1c} complexes and CENP-QU using surface plasmon resonance (SPR). SPR sensorgrams for **i)** K^{HB-RWD}M (containing full-length, wildtype Dsn1), and **ii)** K^{HB-RWD}M^{2E} (containing full-length Dsn1 with Dsn1^{S240E} and Dsn1^{S250E} phosphomimetic mutations) binding to CENP-QU. **iii)** Table summarising K^{HB-RWD}M and K^{HB-RWD}M^{2E} association (k_{on}) and dissociation constants (k_{off}) for CENP-QU, where K^{kin}_{d}, kinetic dissociation constant = k_{on}/k_{off}.

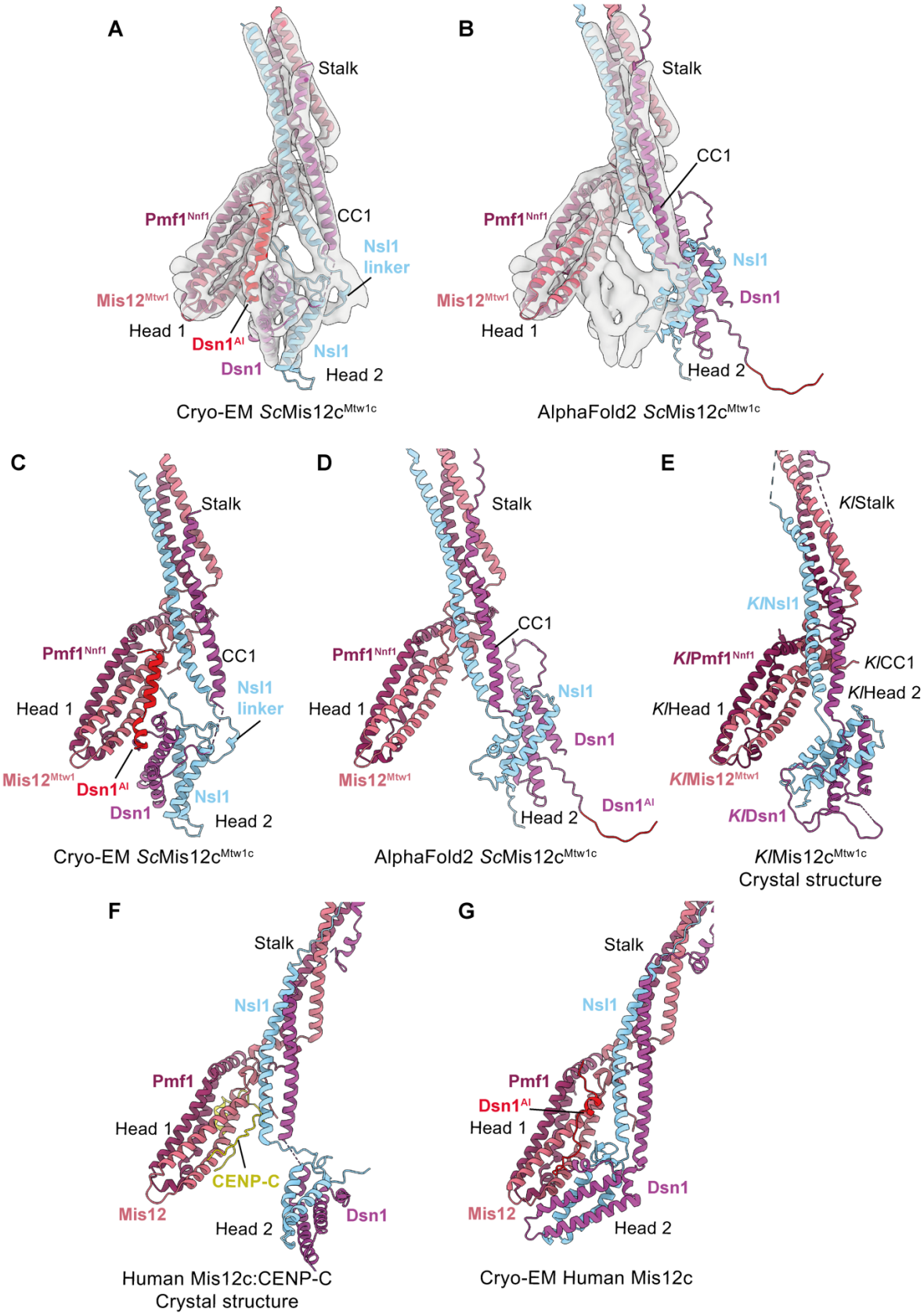

Figure 7: Predicted conformational change of Dsn1^{AI} and head 2 accompanying *Sc*Mis12c^{Mtw1c} activation of by Dsn1^{AI} phosphorylation.

A) Fit of *S. cerevisiae* Mis12c^{Mtw1c} (*Sc*Mis12c^{Mtw1c}) base region (heads 1 and 2 and stalk) into cryo-EM map with head 2 (base body 2, Figure S7A). Dsn1^{AI} is shown in red. **B)** In the AF2 model of

*Sc*Mis12c^{Mtw1c}, head 2 is rotated and displaced from head 1 relative to the cryo-EM structure. **C)** *Sc*Mis12c^{Mtw1c} without cryo-EM density. **D)** AF2 model of *Sc*Mis12c^{Mtw1c} without cryo-EM density. **E)** Crystal structure of the heads and stalk region of *K. lactis* Mis12c^{Mtw1c} (PDB: 5T58). Head 2 adopts a similar conformation to head 2 of the AF2 model of *Sc*Mis12c^{Mtw1c} (panel D). **F)** Crystal structure of the heads and stalk region of activated human Mis12c in complex with CENP-C (residues 1-48) (PDB: 5LSK). **G)** Cryo-EM structure of the heads and stalk region of human Mis12c (PDB: 8PPR) in the inactive unphosphorylated conformation.

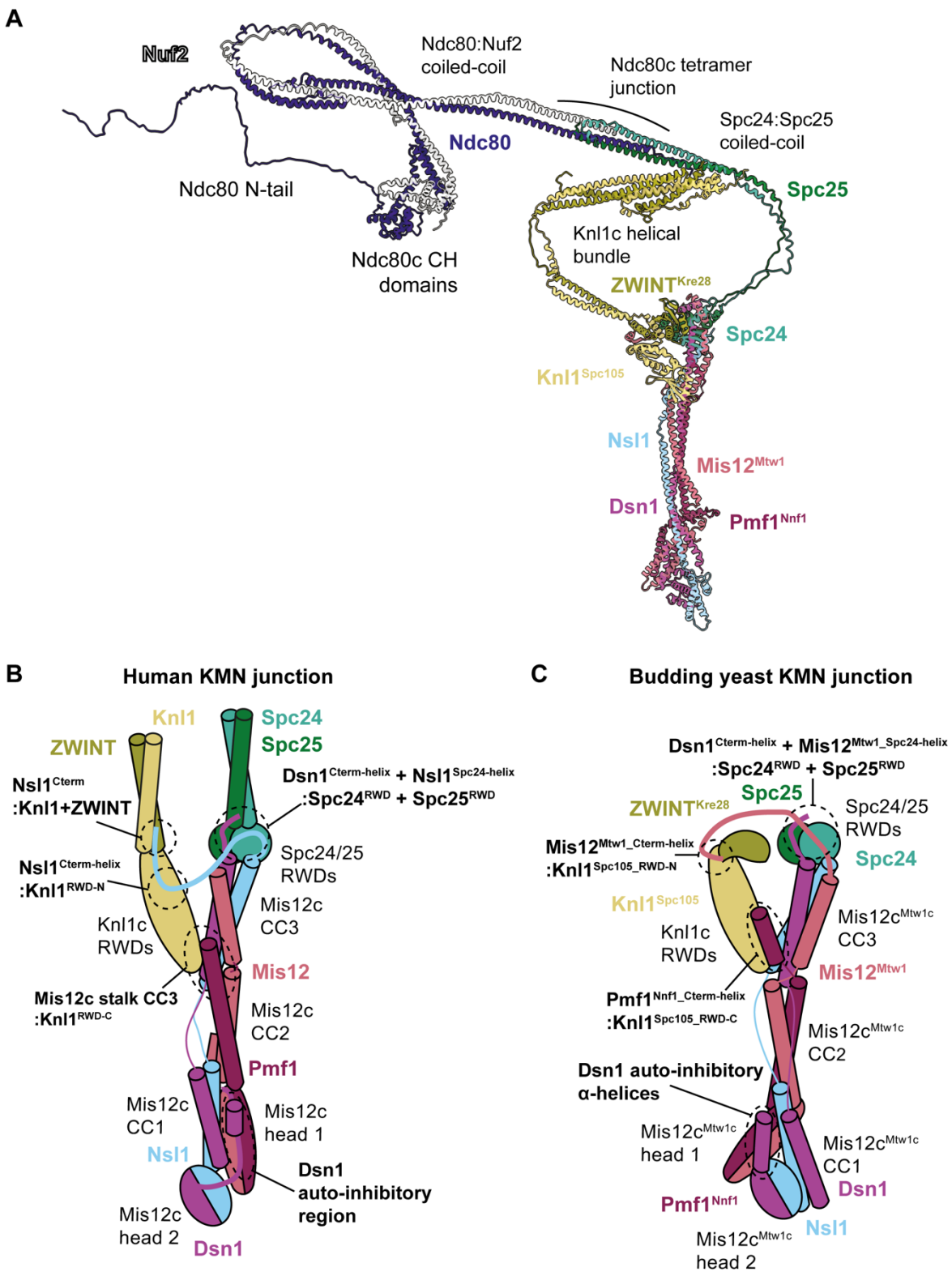

Figure 8: Hypothetical model of the entire *S. cerevisiae* KMN complex and comparison to humans

A) Model of the entire *S. cerevisiae* KMN complex based on the structures determined experimentally in this study and AF2 models of Knl1c (Figure S10A and S10B) and Ndc80c (Figure S10C and S10D). Flexibility of Ndc80c has been previously demonstrated (Scarborough et al., 2019; Wang et al., 2008), and flexibility of the Knl1c helical bundle is inferred from AF2 models shown in Figure

S10A and S10B. CH: calponin homology. N-tail: N-terminal tail. **B)** Cartoon schematic of the human KMN junction complex, based on the structures determined in Yatskevich *et al*., 2024 (PDB: 8PPR). Interactions between $Nsl1^{Cterm}$ and Knl1c; Mis12c stalk CC3 region and $Knl1^{RWD\text{-}C}$; $Dsn1^{Cterm\text{-}helix}$ and $Nsl1^{Spc24\text{-}helix}$ and the Spc24 and 25 RWD domains, and Mis12c head 1 and $Dsn1^{AI}$, are highlighted. **C)** Cartoon schematic of the *S. cerevisiae* KMN junction complex, based on the structures determined in this study. The interactions between $Mis12^{Mtw1_Cterm\text{-}helix}$ and $Knl1^{Spc105_RWD\text{-}N}$; $Pmf1^{Nnf1_Cterm_helix}$ and $Knl1^{Spc105_RWD\text{-}C}$; $Dsn1^{Cterm\text{-}helix}$ and $Mtw1^{Spc24\text{-}helix}$ and the Spc24 and 25 RWD domains, and $Mis12c^{Mtw1c}$ and the two auto-inhibitory α-helices in Dsn^{AI}, are highlighted.

Supplementary Figures

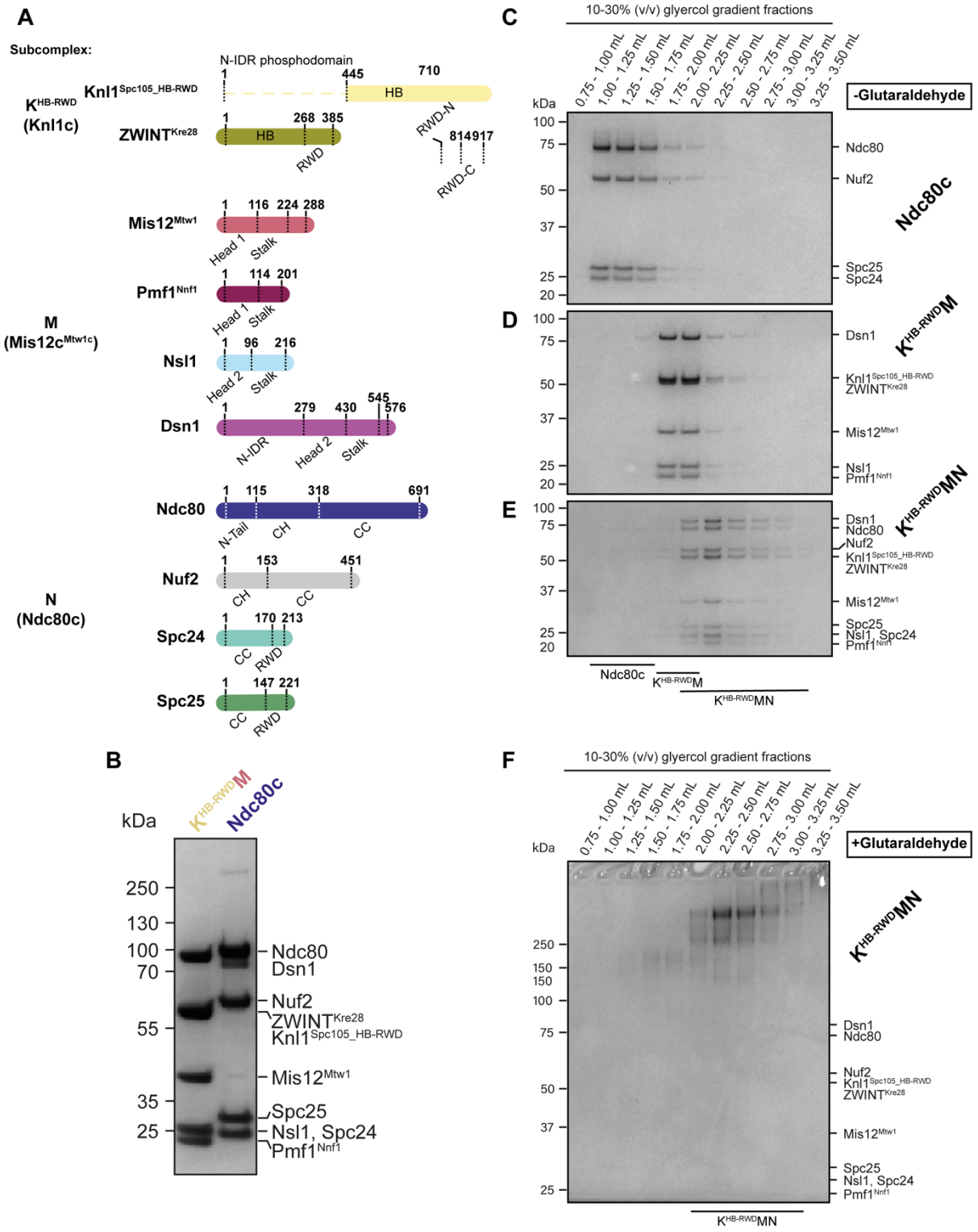

Figure S1: Preparation of *S. cerevisiae* KMN complex sample for Cryo-EM

A) Subcomplex and subunit domain organisation of the *S. cerevisiae* KMN complex proteins. Coiled-coil (CC), calponin homology (CH), helical bundle (HB), N-terminal intrinsically disordered region (N-IDR) and RING-WD40-DEAD box helicase (RWD) domains are highlighted. **B)** Coomassie brilliant blue stained SDS-PAGE gels of the purified KMN subcomplexes. **C-E)** Coomassie brilliant blue stained SDS-PAGE gels of isolated **C)** N and **D)** $K^{HB\text{-}RWD}M$ subcomplexes, or **E)** reconstituted

$K^{HB\text{-}RWD}$MN complexes after separation using 10-30% glycerol gradients. **F)** Coomassie brilliant blue stained SDS-PAGE gels of the reconstituted $K^{HB\text{-}RWD}$MN complex crosslinked with a 0.0–0.2% glutaraldehyde gradient over the course of a 10–30% glycerol gradient using the GraFix methodology (Stark, 2010). Crosslinking was repeated twice with identical results. Fractions corresponding to the glycerol gradient volume 2.00 – 2.75 mL were pooled for cryo-EM sample preparation. Fractions corresponding to the glycerol gradient volume 2.00 – 2.75 mL were pooled for cryo-EM sample preparation.

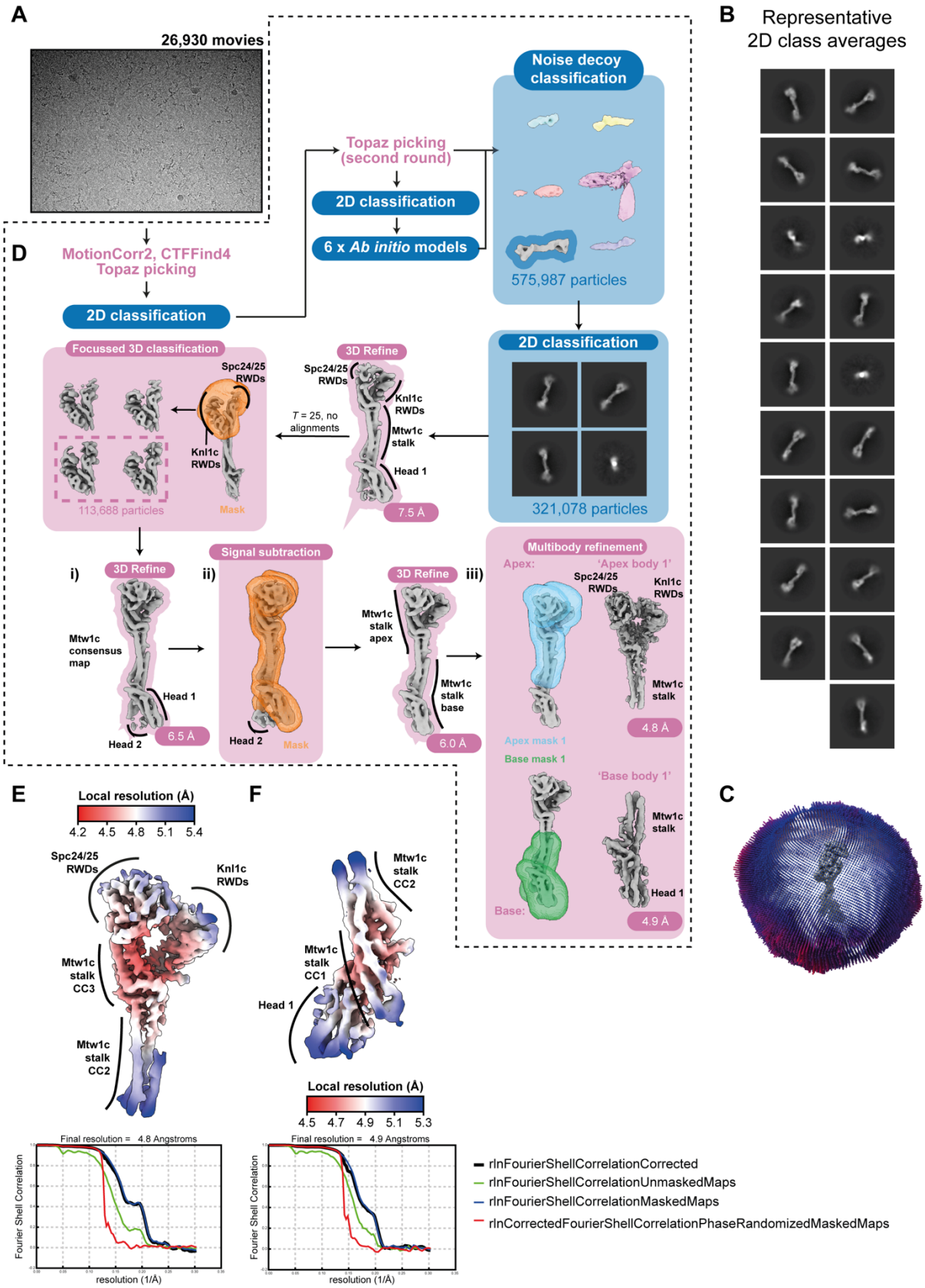

Figure S2: Cryo-EM data processing to reconstruct the KMN junction complex

A) Representative motion corrected cryo-EM movie obtained after data acquisition. A total of 26,390 cryo-EM movies were obtained after data acquisition. **B)** Representative 2D class averages generated using CryoSparc during the 2D classification step following noise decoy classification. **C)** Angular

distribution of views plot of the particles that contributed to the 'apex body 1' and 'base body 1' reconstructions. **D)** Cryo-EM data processing scheme used to reconstruct higher resolution cryo-EM density maps for the KMN junction complex, as described in the Materials and methods section. **E-F)** Cryo-EM density maps coloured according to local resolution of the **E)** 'apex body 1' and **F)** 'base body 1' multibody derived reconstructions that were used to build molecular models (top). Fourier shell correlation (FSC) plot of the **E)** 'apex body 1' and **F)** 'base body 1' multibody derived reconstructions that were used to build the model of the KMN junction complex (bottom).

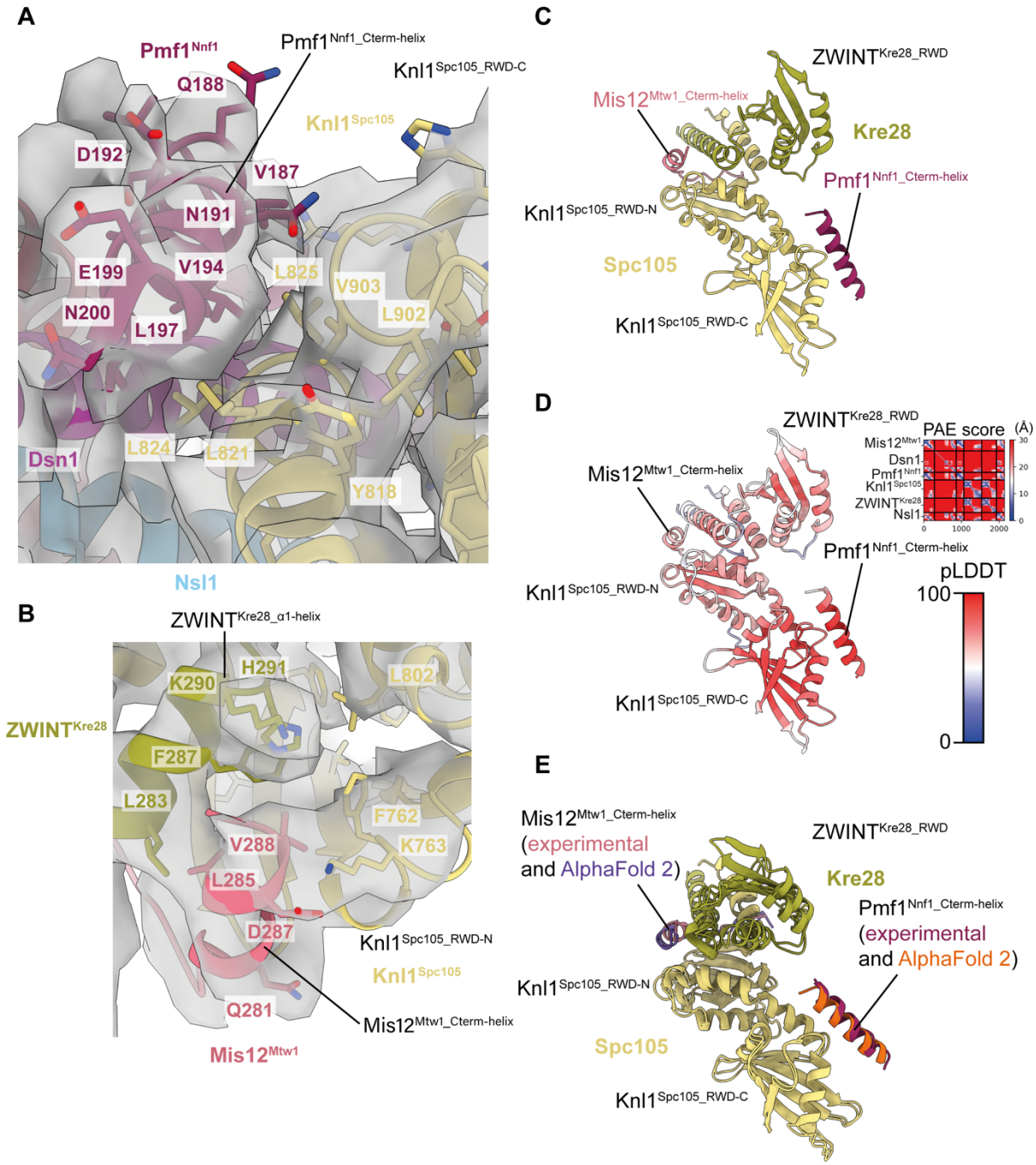

Figure S3: Modelling of interactions between Mis12c^{Mtw1c} and Knl1c

A) Molecular model of the interaction between Pmf1$^{Nnf1_Cterm\text{-}helix}$ and Knl1c docked into the cryo-EM density map, showing density for amino acid side chains relevant to the interaction. **B)** Molecular model of the interaction between Mis12$^{Mtw1_Cterm\text{-}helix}$ and Knl1c docked into the cryo-EM density map, showing density for amino acid side chains relevant to the interaction. **C)** AF2 structure prediction of the Knl1c:Mis12c^{Mtw1c} interaction. The prediction was performed using full-length protein sequences apart from Knl1^{Spc105}, for which residues 1–444 were excluded. The structure prediction is coloured by chain. **D)** AF2 structure prediction presented in panel **C** with the model coloured by residue pLDDT score and with the predicted alignment error (PAE) score shown as an inset in the top right corner of the panel. **E)** Structural alignment of the Knl1c:Mis12c^{Mtw1c} AF2 model with the Mis12c^{Mtw1c} and Knl1c experimental molecular model generated in this study. The predicted and

experimentally modelled Knl1^{Spc105} and ZWINT^{Kre28} subunits are coloured identically, whereas the Pmf1$^{Nnf1_Cterm\text{-}helix}$ and Mis12$^{Mtw1_Cterm\text{-}helix}$ are coloured distinctly according to whether they derive from the AF2 model or the experimental molecular model,

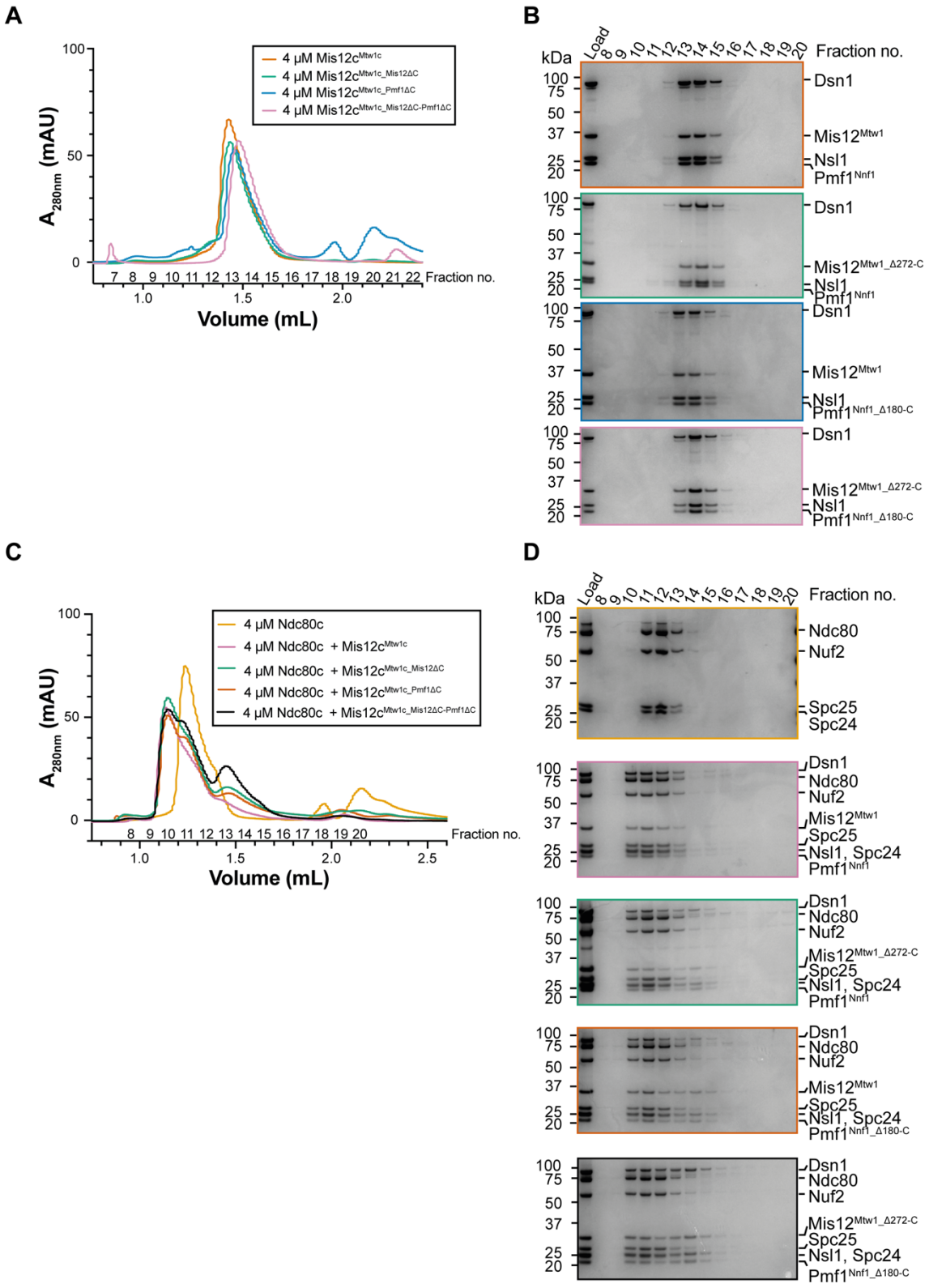

Figure S4: Biochemical analysis of Mis12$^{Mtw1_Cterm\text{-}helix}$ and Pmf1$^{Nnf1_Cterm\text{-}helix}$ function

A) SEC elution chromatograms of Mis12c^{Mtw1c} containing either full-length and wild-type proteins, or with full-length and wild-type proteins apart from deletion of Mis12^{Mtw1} residues 272-289 (Mis12$^{Mis12_\Delta272\text{-}C}$: Mis12c$^{Mtw1c_Mis12\Delta C}$), deletion of Pmf1^{Nnf1} residues 180-201 (Pmf1$^{Nnf1_\Delta180\text{-}C}$: Mis12c$^{Mtw1c_Pmf1\Delta C}$), or deletion of both Mis12^{Mtw1} residues 272-289 and Pmf1^{Nnf1} residues 180-201

(Mis12c$^{Mtw1c_Mis12\Delta C\text{-}Pmf1\Delta C}$). **B)** Coomassie brilliant blue stained SDS-PAGE gels of all of the experiments presented in panel **A**. **C)** SEC elution chromatograms of the Mtw1c:Ndc80c interaction reconstitutions. Attempts at reconstituting Mis12c^{Mtw1c} , Mis12c$^{Mtw1c_Mis12\Delta C}$, Mis12c$^{Mtw1c_Pmf1\Delta C}$, and Mis12c$^{Mtw1c_Mis12\Delta C\text{-}Pmf1\Delta C}$ with full-length, unmodified Ndc80c are presented alongside the elution profile of Ndc80c alone. **D)** Coomassie brilliant blue stained SDS-PAGE gels of the experiments in panel **C**.

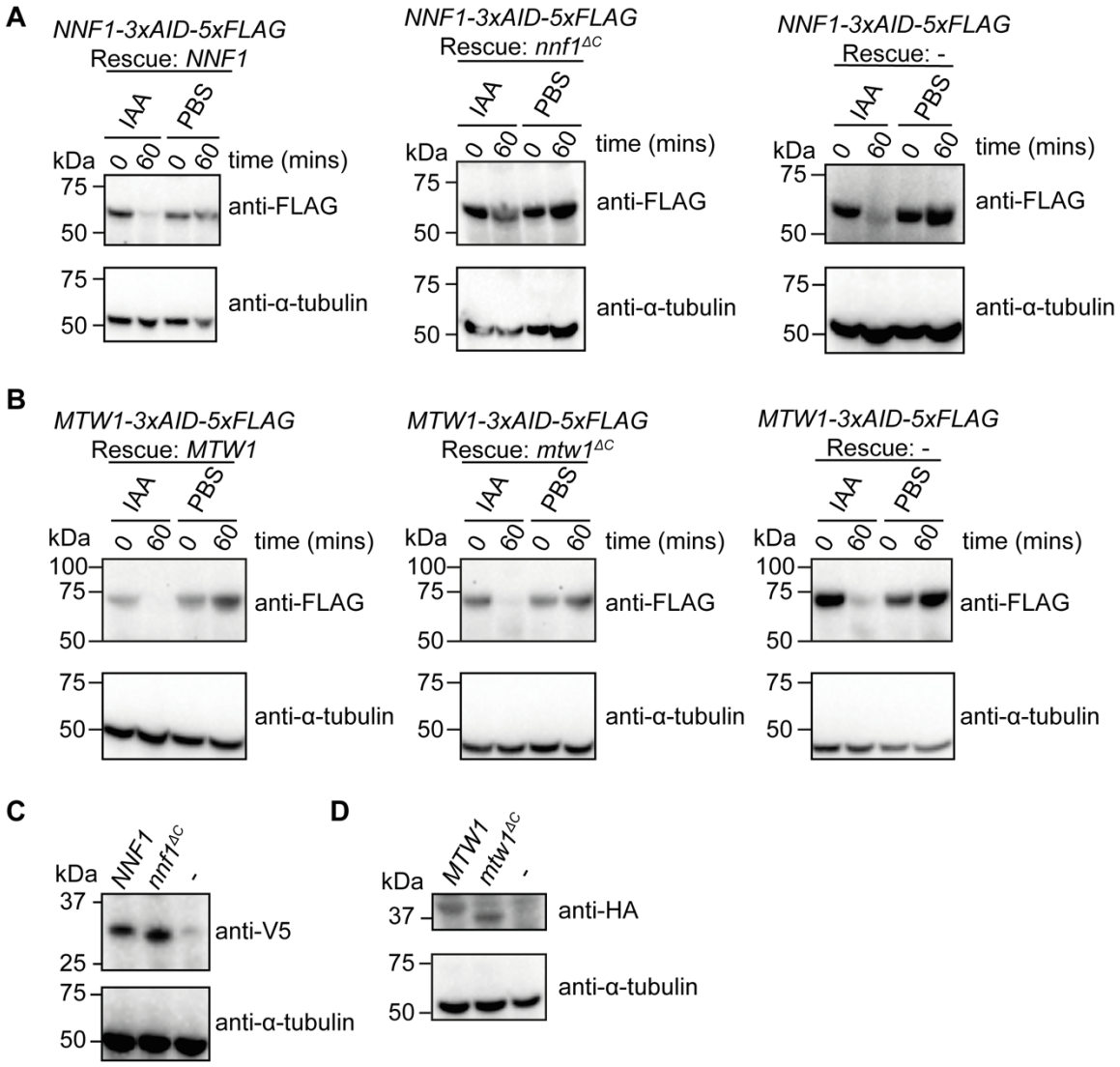

Figure S5: Validation of *in vivo* protein depletion and *in vivo* rescue allele expression

A) Immunoblots of whole cell extracts (WCEs) of the indicated yeast strains treated for the indicated duration with PBS or 0.5 mM Indole-3-acetic acid (IAA). Membranes were blotted with anti-FLAG primary antibody to detect Pmf1^{Nnf1}-mAID$_3$-FLAG$_5$ (top panel) or anti-α-tubulin primary antibody as a loading control (bottom panel). **B)** Immunoblots of WCEs of the indicated yeast strains treated for the indicated duration with PBS or 0.5 mM Indole-3-acetic acid (IAA). Membranes were blotted with anti-FLAG primary antibody to detect Mis12^{Mtw1}-mAID$_3$-FLAG$_5$ (top panel) or anti-α-tubulin primary antibody as a loading control (bottom panel). **C)** Immunoblots of WCEs of the indicated yeast strains. Membranes were blotted with anti-V5 primary antibodies to detect the gene products expressed from the *NNF1* or *nnf1$^{\Delta C}$* variant alleles (top panel), or with anti-α-tubulin primary antibody as a loading control (bottom panel). **D)** Immunoblots of WCEs of the indicated yeast strains. Membranes were blotted with anti-HA primary antibodies to detect the gene products expressed from the indicated *MTW1* or *mtw1$^{\Delta C}$* variant alleles (top panel), or with anti-α-tubulin primary antibody as a loading control (bottom panel).

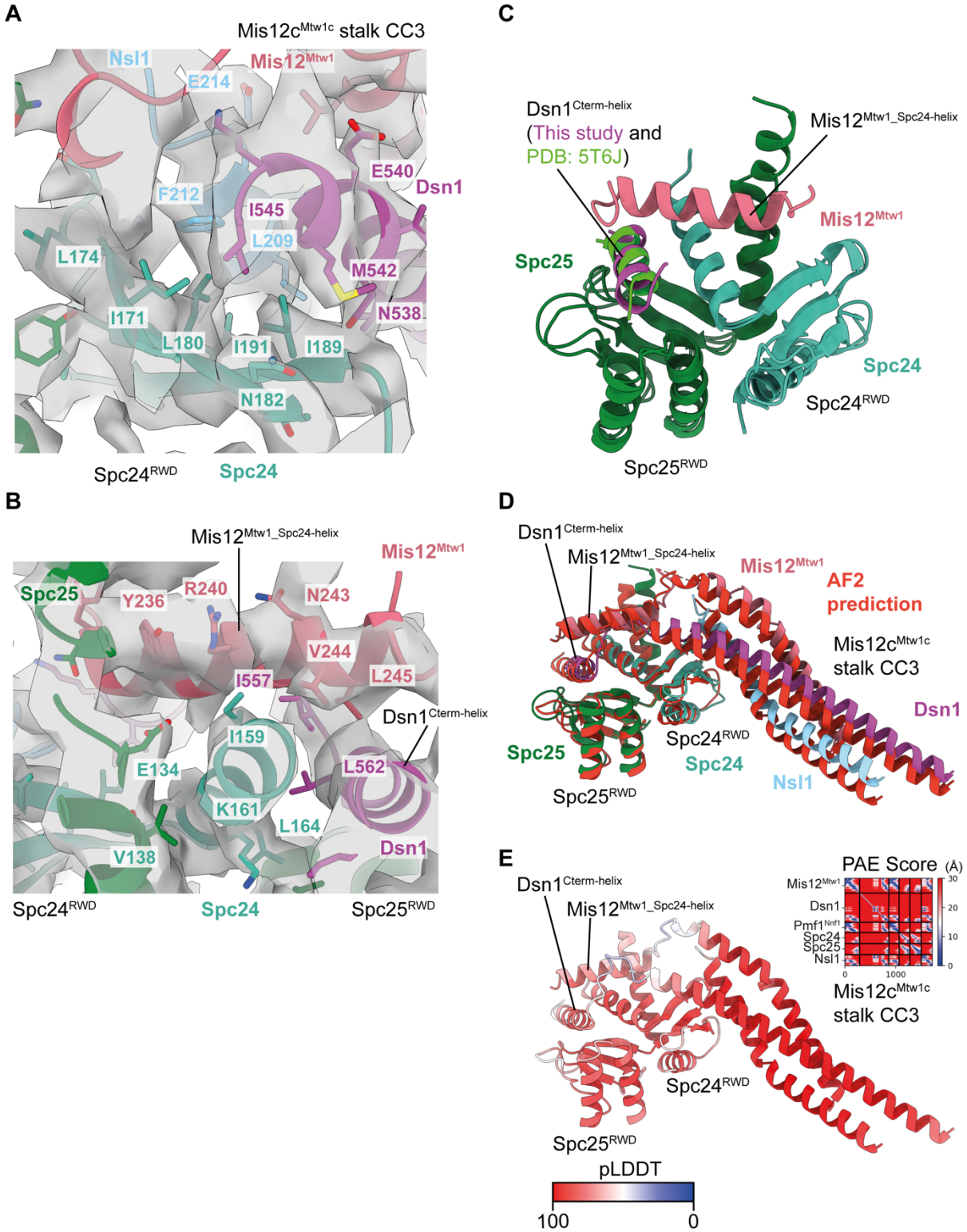

Figure S6: Modelling of interactions between Mis12c^{Mtw1c} and Ndc80c

A) Molecular model of the interactions between the CC3 region of the Mis12c^{Mtw1c} stalk domain and the Spc24 and Spc25 RWD domains docked into the cryo-EM density map, showing density for select amino acid side chains relevant to the interaction. **B)** Molecular model of the interactions between Mis12$^{Mtw1_Spc24\text{-}helix}$ and Dsn1$^{Cterm\text{-}helix}$ motifs with the Spc24 and Spc25 RWD domains docked into the cryo-EM density map, showing density for select amino acid side chains relevant to the interaction.

C) Structural alignment of the crystal structure of Spc24 and Spc25 RWD domains bound to Dsn1$^{560-576}$ peptide (PDB: 5T6J) (Dimitrova et al., 2016) onto the Mis12c^{Mtw1c} and Spc24 and Spc25 experimental molecular models (this study). The Spc24 and Spc25 chains derived from 5T6J and this study are coloured identically, whilst Dsn1$^{Cterm\text{-}helix}$ is coloured distinctly according to whether it derives from 5T6J or this study. **D)** AF2 model of the interaction between Spc24, Spc25, and Mis12c^{Mtw1c} (coloured in red), structurally aligned against the Spc24, Spc25, and Mis12c^{Mtw1c} molecular models produced in this study (coloured by chain). The prediction was performed using full-length and wild-type protein sequences for Spc24, Spc25, and Mis12c^{Mtw1c} subunits. **E)** AF2 structure prediction presented in panel **D** coloured by residue pLDDT score, with the predicted alignment error (PAE) score plot shown in inset in the top right corner.

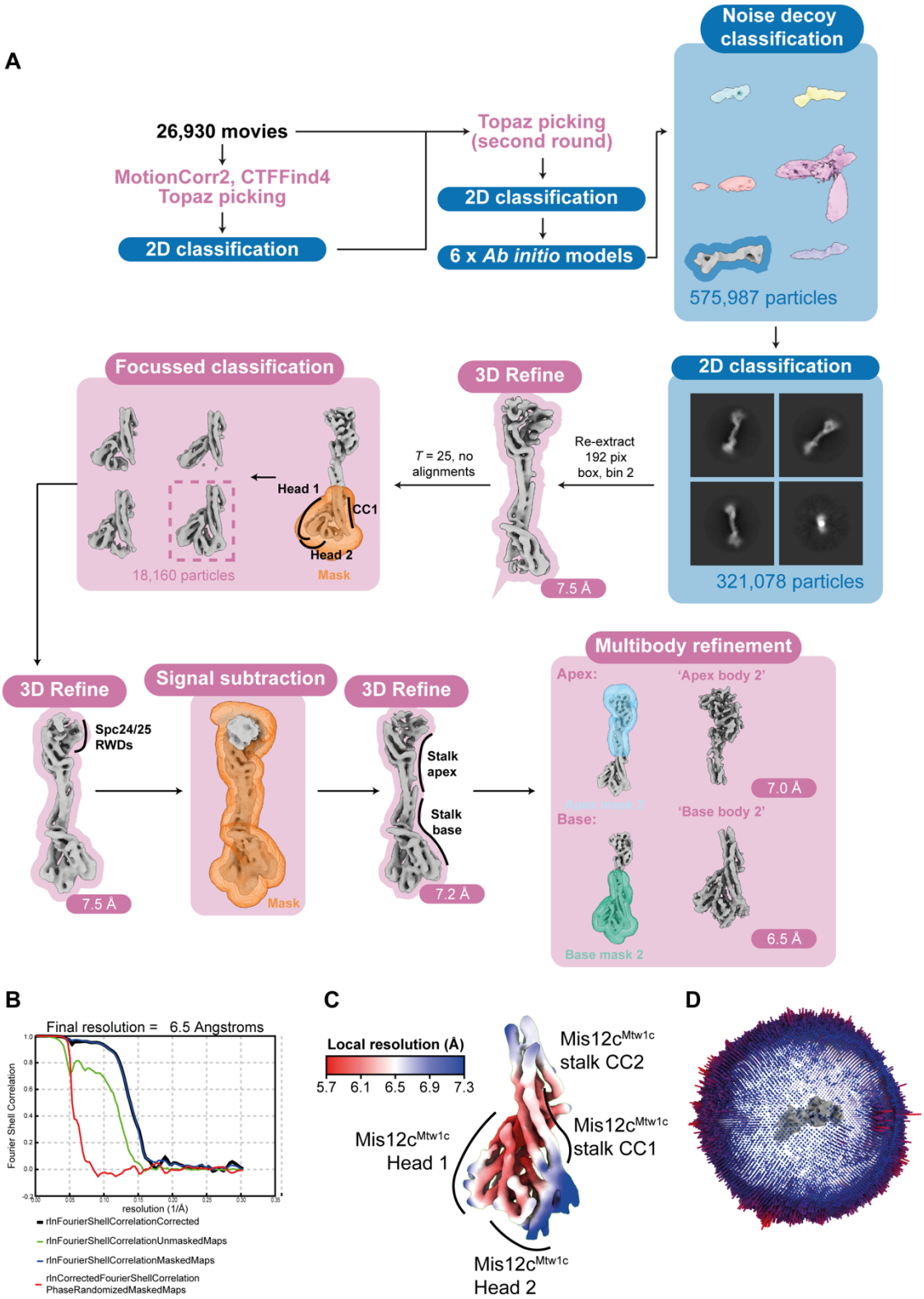

Figure S7: Cryo-EM data processing to reconstruct Mis12c^{Mtw1c} head 2 domain

A) Cryo-EM data processing scheme used to reconstruct cryo-EM density maps containing continuous density for the Mis12c^{Mtw1c} head 2 domain, as described in the Materials and methods section. **B)** Fourier shell correlation (FSC) plot for 'base body 2'. **C)** Cryo-EM density map for 'base body 2' that was used to model the Mis12c^{Mtw1c} head 2 domain coloured according to local resolution. **D)** Angular distribution of views plot for the particles that contributed to the reconstruction of 'base body 2'.

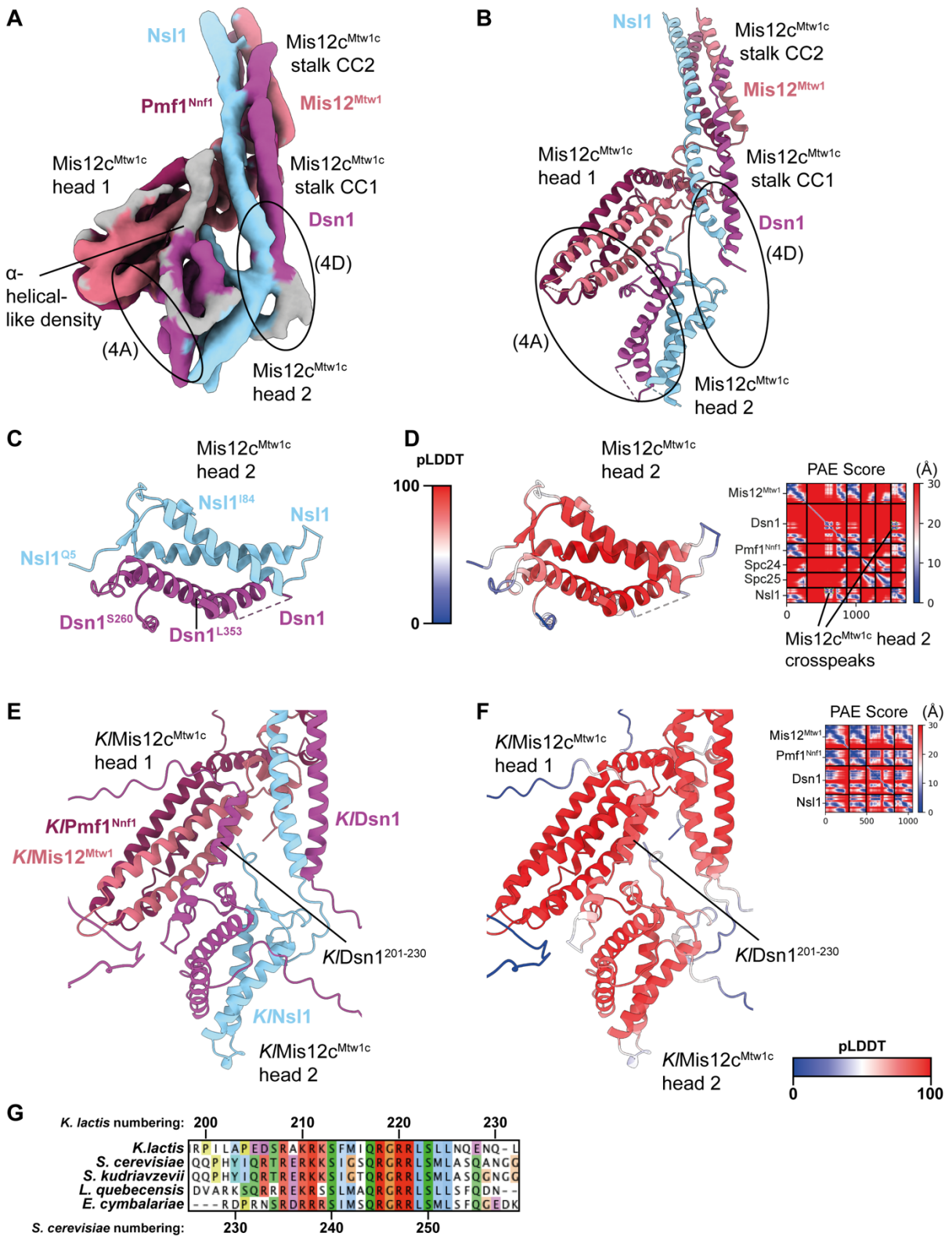

Figure S8: Modelling of contacts between Mis12c^{Mtw1c} head 1, head 2 and Dsn1$^{N\text{-}IDR}$ domains

A) Cryo-EM density map with improved occupancy for the Mis12c^{Mtw1c} head 2 domain (Figure S7) interpreted using the model of Mis12c^{Mtw1c} stalk and head 1 domains built in this study and the AF2 model of *S. cerevisiae* head 2 presented in panels **C** and **D**. (4A) and (4D) highlight regions of the map that are shown in close up in **Figure 4A** and **Figure 4D**, respectively. **B)** Experimental model of *S. cerevisiae* Mis12c^{Mtw1c} head 1 and head 2 domains interacting at the base of the *S. cerevisiae*

Mis12c^{Mtw1c} stalk domain. **C)** AF2 structure prediction of the *S. cerevisiae* Mis12c^{Mtw1c} head 2 domain from the Mis12c^{Mtw1c}:Spc24:Spc25 prediction coloured by chain. Mis12c^{Mtw1c} head 1 and stalk domains, and Spc24:Spc25 are not shown. **D)** AF2 model presented in panel **C** coloured by residue pLDDT score. The predicted alignment error (PAE) score plot is shown on the right of the panel. **E)** AF2 structure prediction of the *K. lactis* Mis12c^{Mtw1c} (*Kl*Mis12c^{Mtw1c}) coloured by chain. The prediction was performed using all full-length and wild-type protein sequences apart from *K. lactis* Dsn1 (*Kl*Dsn1), for which residues 1-149 were excluded to obtain predictions for the interaction between *Kl*Dsn1$^{201-230}$ and *Kl*Mis12c^{Mtw1c} head 1 domain. **F)** AF2 model presented in panel **E** coloured by residue pLDDT score. The predicted alignment error (PAE) score plot is shown on the right of the panel. **G)** Multiple sequence alignment of Dsn1 protein from distantly related budding yeast demonstrates that the *Kl*Dsn1$^{201-230}$ segment of the Dsn1 N-terminal intrinsically disordered region is conserved.

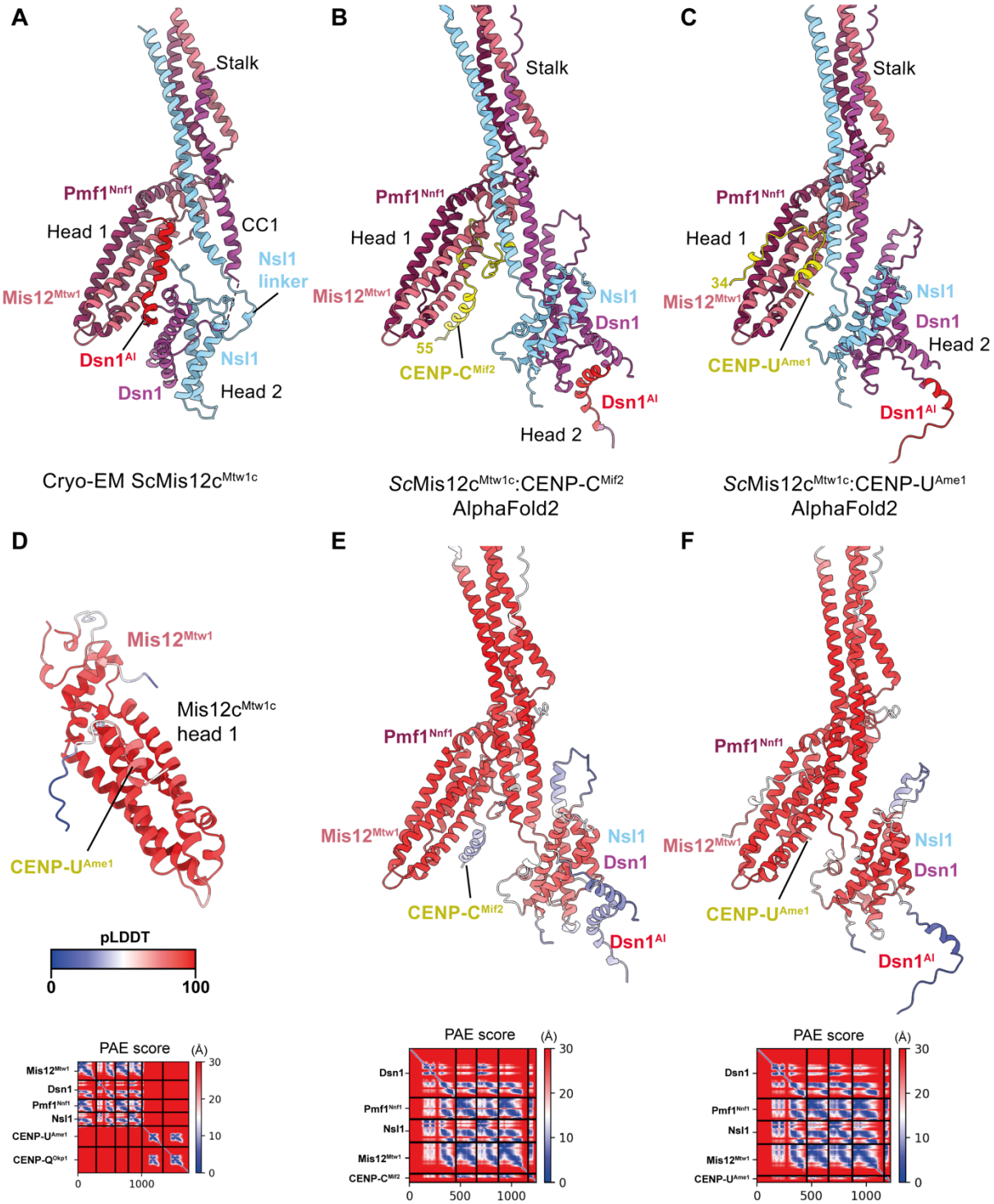

Figure S9: Comparison of cryo-EM structure of *Sc*Mis12c^{Mtw1c} with AF2 models of *Sc*Mis12c^{Mtw1c} in complex with CENP-C^{Mif2} and CENP-U^{Ame1}.

A) Structure of *Sc*Mis12c^{Mtw1c} showing the head 1, head 2 and stalk domains from the cryo-EM structure of the KMN junction complex (base body, Figure S7A). The Dsn1 auto-inhibitory segment (Dsn1^{AI}) in red occludes binding of CENP-C^{Mif2} and CENP-U^{Ame1}, shown in panels B and C. **B)** AF2 models of *Sc*Mis12c^{Mtw1c} in complex with CENP-C^{Mif2} (residues of 1-55) and **C)** CENP-U^{Ame1} (residues 1-34 of CENP-U^{Ame1}). In both AF2 models, head 2 is predicted to rotate by 180° about two orthogonal axes relative to head 2 of the inactive *Sc*Mis12c^{Mtw1c} structure in panel A. **D-F** The AF2 Multimer structure prediction of (D) CENP-U^{Ame1} (residues 1-24) bound to head 2 (Figure 6A) coloured by residue pLDDT score. The predicted alignment error (PAE) score plot is shown below,

(E) *Sc*Mis12c^{Mtw1c} in complex with CENP-C^{Mif2} (residues of 1-55) and **(F)** *Sc*Mis12c^{Mtw1c} in complex with CENP-U^{Ame1} (residues 1-34 of CENP-U^{Ame1}).

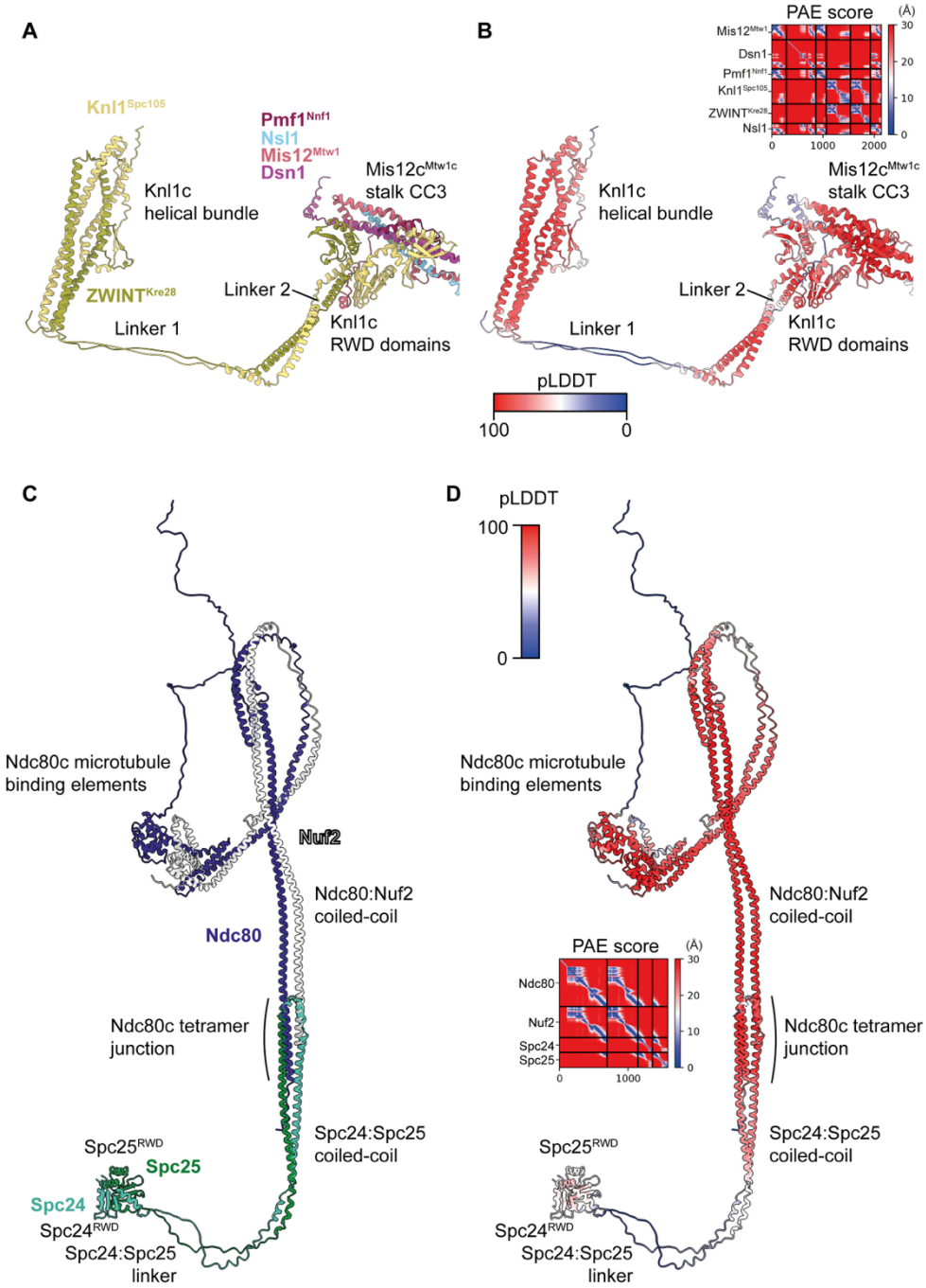

Figure S10: AF2 models of Knl1c helical bundle and Ndc80c

A) AF2 structure prediction of Knl1c:Mis12c^{Mtw1c} coloured by chain, showing the Knl1c helical bundle domain, Knl1c RWD domains, and Mis12c^{Mtw1c} stalk CC3 region. The structure was predicted using full-length, wildtype protein sequences. **B)** AF2 model presented in panel **A,** coloured by residue pLDDT score with the predicted alignment error (PAE) score plot shown as an inset in the top right corner. **C)** AF2 structure prediction of Ndc80c coloured by chain. The structure was predicted using full-length, wildtype protein sequences. **D)** The structure prediction shown in panel **C**, coloured by residue pLDDT score. The predicted alignment error (PAE) score plot of the AF2 Ndc80c model is shown as an inset in the top right corner of this panel.

Data collection and processing						
Microscope	FEI Titan Krios 1					
Voltage (keV)	300					
Magnification	105,000					
Detector	Gatan K3					
Electron dose (e^-/Å^2)	40					
Pixel size (Å/pixel)	0.825					
Exposure rate (e^-/pixel/s)	15.6					
Frames/micrograph (N)	40					
Automation software	EPU					
Micrographs collected (N)	26,930					
Micrographs used (N)	26,930					
Defocus (μm)	-1.4 to -3.0					
Magnification	105,000					
Total extracted particles (N)	2,592,458					
Cryo-EM reconstructions						
	KMN junction consensus map	KMN junction composite map	KMN junction apex body 1	KMN junction base body 1	KMN junction consensus map (head 2)	KMN junction base body 2
Figure	S2Dii	S2Dii	S2E	S2F	S7A	S7C
Accession codes	EMDB N/A	EMDB PDB	EMDB N/A	EMDB N/A	EMDB PDB	EMDB PDB
Final particles (N)	113,688	113,688	113,688	113,688	18,160	18,160
Point group	C1	C1	C1	C1	C1	C1
Resolution global (Å)	6.0	4.8-4.9	4.8	4.9	7.2	6.5
Resolution range local (Å)	ND	ND	4.2-5.4	4.7-5.3	ND	5.7-7.3
FSC threshold	0.143	0.143	0.143	0.143	0.143	0.143
Map sharpening method	RELION					
Refinement						
Software	Phenix					
Resolution limit (Å)	N/A	4.9	N/A	N/A	7.2	6.5
Protein atoms (N)		19,480			21,005	8,388
RMSD bond length (Å)		0.019			0.018	0.027
RMSD bond angle (°)		0.567			0.446	0.596
Model to map fit						
CC mask	N/A	0.6770	N/A	N/A	0.8221	0.8419
CC volume		0.6899			0.8186	0.8423
Validation						
All-atom clash score	N/A	9.81	N/A		15.77	34.52
Ramachandran plot						
Preferred (%)	N/A	95.04	N/A	N/A	96.02	95.66
Allowed (%)		4.88			3.91	4.17
Outliers (%)		0.09			0.07	0.17

Table S1: Cryo-EM data collection, refinement and validation statistics

Strain	Genotype
BY26972 (The Yeast Resource Genetic Resource Center, Japan)	*MAT **a** ade2-1 his3-11,15 trp1-1 leu2-3,112 can1-100 ura3-1::ADH1 OsTIR1(Pmk200, URA3)*
Ynnt001	*MAT **a** ade2-1 his3-11,15 trp1-1 leu2-3,112 can1-100 ura3-1::ADH1 OsTIR1(Pmk200, URA3) MTW1-mAID$_3$-FLAG$_5$::G418*
Ynnt002	*MAT **a** ade2-1 his3-11,15 trp1-1 leu2-3,112 can1-100 ura3-1::ADH1 OsTIR1(Pmk200, URA3) NNF1-mAID$_3$-5Xflag$_5$*
MTW1	*MAT **a** ade2-1 his3-11,15 trp1-1 leu2-3,112 can1-100 ura3-1::ADH1 OsTIR1(Pmk200, URA3), MTW1-mAID$_3$-FLAG$_5$, HA$_3$-MTW1::LEU2*
Mtw1$^{\Delta C}$	*MAT **a** ade2-1 his3-11,15 trp1-1 leu2-3,112 can1-100 ura3-1::ADH1 OsTIR1(Pmk200, URA3), MTW1-mAID$_3$-FLAG$_5$, HA$_3$-MTW1(Δ272-C)::LEU2*
Empty vector (LEU2)	*MAT **a** ade2-1 his3-11,15 trp1-1 leu2-3,112 can1-100 ura3-1::ADH1 OsTIR1(Pmk200, URA3) MTW1-mAID$_3$-FLAG$_5$, Pleu2::LEU2*
NNF1	*MAT **a** ade2-1 his3-11,15 trp1-1 leu2-3,112 can1-100 ura3-1::ADH1 OsTIR1(Pmk200, URA3), NNF1-mAID$_3$-FLAG$_5$, V5$_3$-NNF1::TRP1*
Nnf1$^{\Delta C}$	*MAT **a** ade2-1 his3-11,15 trp1-1 leu2-3,112 can1-100 ura3-1::ADH1 OsTIR1(Pmk200, URA3), NNF1-mAID$_3$-FLAG$_5$, V5$_3$-NNF1(Δ180-C)::TRP1*
Empty vector (TRP1)	*MAT **a** ade2-1 his3-11,15 trp1-1 leu2-3,112 can1-100 ura3-1::ADH1 OsTIR1(Pmk200, URA3), NNF1-mAID$_3$-FLAG$_5$, Ptrp1::TRP1*

Table S2: Genotypes of *S. cerevisiae* strains used within this study.

1162 **Supplementary Video Captions**

1163 **Video S1. Overview of the *S. cerevisiae* KMN junction complex.**

1164 Video shows the molecular details of the *S. cerevisiae* KMN junction complex as shown in
1165 Figures 1-3, detailing the overall architecture of the complex (Figure 1); details of the
1166 Mis12c^{Mtw1c} interface with Knl1c^{Spc105c} (Figure 2); and details of the Mis12c^{Mtw1c} interface
1167 with Ndc80c (Figure 3).

1168 **Video S2. Predicted conformational change of Dsn1^{AI} and head 2 accompanying**
1169 ***Sc*Mis12c^{Mtw1c} activation by Dsn1^{AI} phosphorylation.**

1170 Video shows proposed conformational change of Dsn1^{AI} and head 2 caused by Aurora B^{Ipl1}-
1171 phosphorylation of Ser240 and Ser250 (Figure 7). Phospho-Ser240 would cause electrostatic
1172 repulsion with the negatively-charged surface of Mis12c^{Mtw1c} head 1 as well as steric clashes
1173 with Nsl1 of head 2. Displacement of Dsn1^{AI} and head 2 releases the CENP-C^{Mif2}-binding
1174 site on Mis12c^{Mtw1c} mainly mediated through head 1. The Mis12c^{Mtw1c}-CENP-C ^{Mif2} complex
1175 is based on an AF2 model.

References

Akiyoshi, B., C.R. Nelson, and S. Biggins. 2013. The Aurora B Kinase Promotes Inner and Outer Kinetochore Interactions in Budding Yeast. *Genetics*. 194:785-789.

Akiyoshi, B., K.K. Sarangapani, A.F. Powers, C.R. Nelson, S.L. Reichow, H. Arellano-Santoyo, T. Gonen, J.A. Ranish, C.L. Asbury, and S. Biggins. 2010. Tension directly stabilizes reconstituted kinetochore-microtubule attachments. *Nature*. 468:576-579.

Alushin, G.M., V. Musinipally, D. Matson, J. Tooley, P.T. Stukenberg, and E. Nogales. 2012. Multimodal microtubule binding by the Ndc80 kinetochore complex. *Nature Structural & Molecular Biology*. 19:1161-1167.

Alushin, G.M., V.H. Ramey, S. Pasqualato, D.A. Ball, N. Grigorieff, A. Musacchio, and E. Nogales. 2010. The Ndc80 kinetochore complex forms oligomeric arrays along microtubules. *Nature*. 467:805-810.

Aravamudhan, P., I. Felzer-Kim, K. Gurunathan, and A.P. Joglekar. 2014. Assembling the Protein Architecture of the Budding Yeast Kinetochore-Microtubule Attachment using FRET. *Current Biology*. 24:1437-1446.

Ariyoshi, M., and T. Fukagawa. 2023. An updated view of the kinetochore architecture. *Trends in Genetics*. 39:941-953.

Ariyoshi, M., F. Makino, R. Watanabe, R. Nakagawa, T. Kato, K. Namba, Y. Arimura, R. Fujita, H. Kurumizaka, E.I. Okumura, M. Hara, and T. Fukagawa. 2021. Cryo-EM structure of the CENP-A nucleosome in complex with phosphorylated CENP-C. *The EMBO Journal*. 40. 40(5):e105671. doi: 10.15252/embj.2020105671

Batth, T.S., M.X. Tollenaere, P. Rüther, A. Gonzalez-Franquesa, B.S. Prabhakar, S. Bekker-Jensen, A.S. Deshmukh, and J.V. Olsen. 2019. Protein Aggregation Capture on Microparticles Enables Multipurpose Proteomics Sample Preparation*. *Molecular & Cellular Proteomics*. 18:1027a-1035.

Bepler, T., A. Morin, M. Rapp, J. Brasch, L. Shapiro, A.J. Noble, and B. Berger. 2019. Positive-unlabeled convolutional neural networks for particle picking in cryo-electron micrographs. *Nature Methods*. 16:1153-1160.

Buvelot, S.P., S.Y. Tatsutani, D. Vermaak, and S. Biggins. 2003. The budding yeast Ipl1/Aurora protein kinase regulates mitotic spindle disassembly. *The Journal of Cell Biology*. 160:329-339.

Campbell, C.S., and A. Desai. 2013. Tension sensing by Aurora B kinase is independent of survivin-based centromere localization. *Nature*. 497:118-121.

Chambers, M.C., B. Maclean, R. Burke, D. Amodei, D.L. Ruderman, S. Neumann, L. Gatto, B. Fischer, B. Pratt, J. Egertson, K. Hoff, D. Kessner, N. Tasman, N. Shulman, B. Frewen, T.A. Baker, M.-Y. Brusniak, C. Paulse, D. Creasy, L. Flashner, K. Kani, C. Moulding, S.L. Seymour, L.M. Nuwaysir, B. Lefebvre, F. Kuhlmann, J. Roark, P. Rainer, S. Detlev, T. Hemenway, A. Huhmer, J. Langridge, B. Connolly, T. Chadick, K. Holly, J. Eckels, E.W. Deutsch, R.L. Moritz, J.E. Katz, D.B. Agus, M. Maccoss, D.L. Tabb, and P. Mallick. 2012. A cross-platform toolkit for mass spectrometry and proteomics. *Nature Biotechnology*. 30:918-920.

Cheeseman, I.M., J.S. Chappie, E.M. Wilson-Kubalek, and A. Desai. 2006. The Conserved KMN Network Constitutes the Core Microtubule-Binding Site of the Kinetochore. *Cell*. 127:983-997.

Cieslinski, K., Y.-L. Wu, L. Nechyporenko, S.J. Hörner, D. Conti, M. Skruzny, and J. Ries. 2023. Nanoscale structural organization and stoichiometry of the budding yeast kinetochore. *Journal of Cell Biology*. 222.

Ciferri, C., J. De Luca, S. Monzani, K.J. Ferrari, D. Ristic, C. Wyman, H. Stark, J. Kilmartin, E.D. Salmon, and A. Musacchio. 2005. Architecture of the Human Ndc80-Hec1

Complex, a Critical Constituent of the Outer Kinetochore. *Journal of Biological Chemistry*. 280:29088-29095.

Ciferri, C., S. Pasqualato, E. Screpanti, G. Varetti, S. Santaguida, G. Dos Reis, A. Maiolica, J. Polka, J.G. De Luca, P. De Wulf, M. Salek, J. Rappsilber, C.A. Moores, E.D. Salmon, and A. Musacchio. 2008. Implications for Kinetochore-Microtubule Attachment from the Structure of an Engineered Ndc80 Complex. *Cell*. 133:427-439.

Clarke, L., and J. Carbon. 1980. Isolation of a yeast centromere and construction of functional small circular chromosomes. *Nature*. 287:504-509.

Clarke, L., and J. Carbon. 1983. Genomic substitutions of centromeres in Saccharomyces cerevisiae. *Nature*. 305:23-28.

Combe, C.W., M. Graham, L. Kolbowski, L. Fischer, and J. Rappsilber. 2024. xiVIEW: Visualisation of Crosslinking Mass Spectrometry Data. *Journal of Molecular Biology*. 436:168656.

Croll, T.I. 2018. *ISOLDE*: a physically realistic environment for model building into low-resolution electron-density maps. *Acta Crystallographica Section D Structural Biology*. 74:519-530.

Deluca, J.G., W.E. Gall, C. Ciferri, D. Cimini, A. Musacchio, and E.D. Salmon. 2006. Kinetochore Microtubule Dynamics and Attachment Stability Are Regulated by Hec1. *Cell*. 127:969-982.

Dendooven, T., Z. Zhang, J. Yang, S.H. McLaughlin, J. Schwab, S.H.W. Scheres, S. Yatskevich, and D. Barford. 2023. Cryo-EM structure of the complete inner kinetochore of the budding yeast point centromere. *Science Advances*. 9.

Dhatchinamoorthy, K., M. Shivaraju, J.J. Lange, B. Rubinstein, J.R. Unruh, B.D. Slaughter, and J.L. Gerton. 2017. Structural plasticity of the living kinetochore. *Journal of Cell Biology*. 216:3551-3570.

Dimitrova, Y.N., S. Jenni, R. Valverde, Y. Khin, and S.C. Harrison. 2016. Structure of the MIND Complex Defines a Regulatory Focus for Yeast Kinetochore Assembly. *Cell*. 167:1014-1027.e1012.

Dudziak, A., J. Schmidt, F. Hamm, S. Tendulkar, K. Jänen, I.R. Vetter, S. Singh, J. Fischböck, F. Herzog, and S. Westermann. 2024. The Spc105^{Knl1}/Kre28^{Zwint} complex promotes mitotic error correction by outer kinetochore recruitment of the Ipl1$^{Aurora\ B}$ kinase. EMBO J. 2025 Apr 25. doi: 10.1038/s44318-025-00437-w. Online ahead of print.

Edgerton, H.D., S. Mukherjee, M. Johansson, J. Bachant, M.K. Gardner, and D.J. Clarke. 2023. Low tension recruits the yeast Aurora B protein Ipl1 to centromeres in metaphase. *Journal of Cell Science*. 136.

Emanuele, M.J., W. Lan, M. Jwa, S.A. Miller, C.S.M. Chan, and P.T. Stukenberg. 2008. Aurora B kinase and protein phosphatase 1 have opposing roles in modulating kinetochore assembly. *The Journal of Cell Biology*. 181:241-254.

Emsley, P., B. Lohkamp, W.G. Scott, and K. Cowtan. 2010. Features and development of *Coot*. *Acta Crystallographica Section D Biological Crystallography*. 66:486-501.

Euskirchen, G.M. 2002. Nnf1p, Dsn1p, Mtw1p, and Nsl1p: a New Group of Proteins Important for Chromosome Segregation in *Saccharomyces cerevisiae*. *Eukaryotic Cell*. 1:229-240.

Fischböck-Halwachs, J., S. Singh, M. Potocnjak, G. Hagemann, V. Solis-Mezarino, S. Woike, M. Ghodgaonkar-Steger, F. Weissmann, L.D. Gallego, J. Rojas, J. Andreani, A. Köhler, and F. Herzog. 2019. The COMA complex interacts with Cse4 and positions Sli15/Ipl1 at the budding yeast inner kinetochore. *eLife*. 8.

Fischer, E.S. 2023. Kinetochore-catalyzed MCC formation: A structural perspective. *IUBMB Life*. 75:289-310.

Fitzgerald-Hayes, M., L. Clarke, and J. Carbon. 1982. Nucleotide sequence comparisons and functional analysis of yeast centromere DNAs. *Cell*. 29:235-244.

Frigola, J., D. Remus, A. Mehanna, and J.F.X. Diffley. 2013. ATPase-dependent quality control of DNA replication origin licensing. *Nature*. 495:339-343.

García-Rodríguez, L.J., T. Kasciukovic, V. Denninger, and T.U. Tanaka. 2019. Aurora B-INCENP Localization at Centromeres/Inner Kinetochores Is Required for Chromosome Bi-orientation in Budding Yeast. *Current Biology*. 29:1536-1544.e1534.

Ghodgaonkar-Steger, M., M. Potocnjak, T. Zimniak, J. Fischböck-Halwachs, V. Solis-Mezarino, S. Singh, T. Speljko, G. Hagemann, D.J. Drexler, G. Witte, and F. Herzog. 2020. C-Terminal Motifs of the MTW1 Complex Cooperatively Stabilize Outer Kinetochore Assembly in Budding Yeast. *Cell Reports*. 32:108190.

Gietz, R.D., and R.H. Schiestl. 2007. High-efficiency yeast transformation using the LiAc/SS carrier DNA/PEG method. *Nature Protocols*. 2:31-34.

Goddard, T.D., C.C. Huang, E.C. Meng, E.F. Pettersen, G.S. Couch, J.H. Morris, and T.E. Ferrin. 2018. UCSF ChimeraX: Meeting modern challenges in visualization and analysis. *Protein Science*. 27:14-25.

Helgeson, L.A., A. Zelter, M. Riffle, M.J. Maccoss, C.L. Asbury, and T.N. Davis. 2018. Human Ska complex and Ndc80 complex interact to form a load-bearing assembly that strengthens kinetochore–microtubule attachments. *Proceedings of the National Academy of Sciences*. 115:2740-2745.

Hornung, P., M. Maier, G.M. Alushin, G.C. Lander, E. Nogales, and S. Westermann. 2011. Molecular Architecture and Connectivity of the Budding Yeast Mtw1 Kinetochore Complex. *Journal of Molecular Biology*. 405:548-559.

Hornung, P., P. Troc, F. Malvezzi, M. Maier, Z. Demianova, T. Zimniak, G. Litos, F. Lampert, A. Schleiffer, M. Brunner, K. Mechtler, F. Herzog, T.C. Marlovits, and S. Westermann. 2014. A cooperative mechanism drives budding yeast kinetochore assembly downstream of CENP-A. *Journal of Cell Biology*. 206:509-524.

Hughes, C.S., S. Moggridge, T. Müller, P.H. Sorensen, G.B. Morin, and J. Krijgsveld. 2019. Single-pot, solid-phase-enhanced sample preparation for proteomics experiments. *Nature Protocols*. 14:68-85.

Huis In 'T Veld, P.J., S. Jeganathan, A. Petrovic, P. Singh, J. John, V. Krenn, F. Weissmann, T. Bange, and A. Musacchio. 2016. Molecular basis of outer kinetochore assembly on CENP-T. *eLife*. 5.

Huis In 'T Veld, P.J., V.A. Volkov, I.D. Stender, A. Musacchio, and M. Dogterom. 2019. Molecular determinants of the Ska-Ndc80 interaction and their influence on microtubule tracking and force-coupling. *eLife*. 8.

Hyman, A.A., and P.K. Sorger. 1995. Structure and Function of Kinetochores in Budding Yeast. *Annual Review of Cell and Developmental Biology*. 11:471-495.

Joglekar, A.P., D.C. Bouck, J.N. Molk, K.S. Bloom, and E.D. Salmon. 2006. Molecular architecture of a kinetochore–microtubule attachment site. *Nature Cell Biology*. 8:581-585.

Johnston, K., A. Joglekar, T. Hori, A. Suzuki, T. Fukagawa, and E.D. Salmon. 2010. Vertebrate kinetochore protein architecture: protein copy number. *Journal of Cell Biology*. 189:937-943.

Jumper, J., R. Evans, A. Pritzel, T. Green, M. Figurnov, O. Ronneberger, K. Tunyasuvunakool, R. Bates, A. Žídek, A. Potapenko, A. Bridgland, C. Meyer, S.A.A. Kohl, A.J. Ballard, A. Cowie, B. Romera-Paredes, S. Nikolov, R. Jain, J. Adler, T. Back, S. Petersen, D. Reiman, E. Clancy, M. Zielinski, M. Steinegger, M. Pacholska, T. Berghammer, S. Bodenstein, D. Silver, O. Vinyals, A.W. Senior, K. Kavukcuoglu,

P. Kohli, and D. Hassabis. 2021. Highly accurate protein structure prediction with AlphaFold. *Nature*. 596:583-589.
Kato, H., J. Jiang, B.-R. Zhou, M. Rozendaal, H. Feng, R. Ghirlando, T.S. Xiao, A.F. Straight, and Y. Bai. 2013. A Conserved Mechanism for Centromeric Nucleosome Recognition by Centromere Protein CENP-C. *Science*. 340:1110-1113.
Kern, D.M., J.K. Monda, K.-C. Su, E.M. Wilson-Kubalek, and I.M. Cheeseman. 2017. Astrin-SKAP complex reconstitution reveals its kinetochore interaction with microtubule-bound Ndc80. *eLife*. 6.
Killinger, K., M. Böhm, P. Steinbach, G. Hagemann, M. Blüggel, K. Jänen, S. Hohoff, P. Bayer, F. Herzog, and S. Westermann. 2020. Auto-inhibition of Mif2/CENP-C ensures centromere-dependent kinetochore assembly in budding yeast. *The EMBO Journal*. 39.
Kim, S., and H. Yu. 2015. Multiple assembly mechanisms anchor the KMN spindle checkpoint platform at human mitotic kinetochores. *Journal of Cell Biology*. 208:181-196.
Kimanius, D., L. Dong, G. Sharov, T. Nakane, and S.H.W. Scheres. 2021. New tools for automated cryo-EM single-particle analysis in RELION-4.0. *Biochemical Journal*. 478:4169-4185.
Kimanius, D., K. Jamali, M.E. Wilkinson, S. Lövestam, V. Velazhahan, T. Nakane, and S.H.W. Scheres. 2024. Data-driven regularization lowers the size barrier of cryo-EM structure determination. *Nature Methods*. 21:1216-1221.
Kitamura, E., K. Tanaka, Y. Kitamura, and T.U. Tanaka. 2007. Kinetochore–microtubule interaction during S phase in *Saccharomyces cerevisiae*. *Genes & Development*. 21:3319-3330.
Kiyomitsu, T., C. Obuse, and M. Yanagida. 2007. Human Blinkin/AF15q14 Is Required for Chromosome Alignment and the Mitotic Checkpoint through Direct Interaction with Bub1 and BubR1. *Developmental Cell*. 13:663-676.
Lampert, F., P. Hornung, and S. Westermann. 2010. The Dam1 complex confers microtubule plus end–tracking activity to the Ndc80 kinetochore complex. *Journal of Cell Biology*. 189:641-649.
Lampert, F., C. Mieck, G.M. Alushin, E. Nogales, and S. Westermann. 2013. Molecular requirements for the formation of a kinetochore–microtubule interface by Dam1 and Ndc80 complexes. *Journal of Cell Biology*. 200:21-30.
Lang, J., A. Barber, and S. Biggins. 2018. An assay for de novo kinetochore assembly reveals a key role for the CENP-T pathway in budding yeast. *eLife*. 7.
Li, S., L.J. Garcia-Rodriguez, and T.U. Tanaka. 2023. Chromosome biorientation requires Aurora B's spatial separation from its outer kinetochore substrates, but not its turnover at kinetochores. *Current Biology*. 33:4557-4569.e4553.
Li, Y., J. Bachant, A.A. Alcasabas, Y. Wang, J. Qin, and S.J. Elledge. 2002. The mitotic spindle is required for loading of the DASH complex onto the kinetochore. *Genes & Development*. 16:183-197.
Liebschner, D., P.V. Afonine, M.L. Baker, G. Bunkóczi, V.B. Chen, T.I. Croll, B. Hintze, L.-W. Hung, S. Jain, A.J. McCoy, N.W. Moriarty, R.D. Oeffner, B.K. Poon, M.G. Prisant, R.J. Read, J.S. Richardson, D.C. Richardson, M.D. Sammito, O.V. Sobolev, D.H. Stockwell, T.C. Terwilliger, A.G. Urzhumtsev, L.L. Videau, C.J. Williams, and P.D. Adams. 2019. Macromolecular structure determination using X-rays, neutrons and electrons: recent developments in *Phenix*. *Acta Crystallographica Section D Structural Biology*. 75:861-877.

Malvezzi, F., G. Litos, A. Schleiffer, A. Heuck, K. Mechtler, T. Clausen, and S. Westermann. 2013. A structural basis for kinetochore recruitment of the Ndc80 complex via two distinct centromere receptors. *The EMBO Journal*. 32:409-423.

Maskell, D.P., X.-W. Hu, and M.R. Singleton. 2010. Molecular architecture and assembly of the yeast kinetochore MIND complex. *Journal of Cell Biology*. 190:823-834.

McAinsh, A.D., and G.J.P.L. Kops. 2023. Principles and dynamics of spindle assembly checkpoint signalling. *Nature Reviews Molecular Cell Biology*. 24:543-559.

McAinsh, A.D., and A.L. Marston. 2022. The Four Causes: The Functional Architecture of Centromeres and Kinetochores. *Annual Review of Genetics*. 56:279-314.

Mendes, M.L., L. Fischer, Z.A. Chen, M. Barbon, F.J. O'Reilly, S.H. Giese, M. Bohlke-Schneider, A. Belsom, T. Dau, C.W. Combe, M. Graham, M.R. Eisele, W. Baumeister, C. Speck, and J. Rappsilber. 2019. An integrated workflow for crosslinking mass spectrometry. *Molecular Systems Biology*. 15.

Mirdita, M., K. Schütze, Y. Moriwaki, L. Heo, S. Ovchinnikov, and M. Steinegger. 2022. ColabFold: making protein folding accessible to all. *Nature Methods*. 19:679-682.

Muir, K.W., C. Batters, T. Dendooven, J. Yang, Z. Zhang, A. Burt, and D. Barford. 2023. Structural mechanism of outer kinetochore Dam1-Ndc80 complex assembly on microtubules. *Science*. 382:1184-1190.

Musacchio, A., and A. Desai. 2017. A Molecular View of Kinetochore Assembly and Function. *Biology*. 6:5.

Nekrasov, V.S., M.A. Smith, S. Peak-Chew, and J.V. Kilmartin. 2003. Interactions between Centromere Complexes in *Saccharomyces cerevisiae*. *Molecular Biology of the Cell*. 14:4931-4946.

Nerusheva, O.O., S. Galander, J. Fernius, D. Kelly, and A.L. Marston. 2014. Tension-dependent removal of pericentromeric shugoshin is an indicator of sister chromosome biorientation. *Genes & Development*. 28:1291-1309.

Nishino, T., F. Rago, T. Hori, K. Tomii, I.M. Cheeseman, and T. Fukagawa. 2013. CENP-T provides a structural platform for outer kinetochore assembly. *The EMBO Journal*. 32:424-436.

Pagliuca, C., V.M. Draviam, E. Marco, P.K. Sorger, and P. De Wulf. 2009. Roles for the Conserved Spc105p/Kre28p Complex in Kinetochore-Microtubule Binding and the Spindle Assembly Checkpoint. *PLoS ONE*. 4:e7640.

Parnell, E.J., E.E. Jenson, and M.P. Miller. 2024. A conserved site on Ndc80 complex facilitates dynamic recruitment of Mps1 to yeast kinetochores to promote accurate chromosome segregation. *Current Biology*. 34:2294-2307.e2294.

Petrovic, A., J. Keller, Y. Liu, K. Overlack, J. John, Y.N. Dimitrova, S. Jenni, S. Van Gerwen, P. Stege, S. Wohlgemuth, P. Rombaut, F. Herzog, S.C. Harrison, I.R. Vetter, and A. Musacchio. 2016. Structure of the MIS12 Complex and Molecular Basis of Its Interaction with CENP-C at Human Kinetochores. *Cell*. 167:1028-1040.e1015.

Petrovic, A., S. Mosalaganti, J. Keller, M. Mattiuzzo, K. Overlack, V. Krenn, Anna, S. Wohlgemuth, V. Cecatiello, S. Pasqualato, S. Raunser, and A. Musacchio. 2014. Modular Assembly of RWD Domains on the Mis12 Complex Underlies Outer Kinetochore Organization. *Molecular Cell*. 53:591-605.

Petrovic, A., S. Pasqualato, P. Dube, V. Krenn, S. Santaguida, D. Cittaro, S. Monzani, L. Massimiliano, J. Keller, A. Tarricone, A. Maiolica, H. Stark, and A. Musacchio. 2010. The MIS12 complex is a protein interaction hub for outer kinetochore assembly. *Journal of Cell Biology*. 190:835-852.

Pettersen, E.F., T.D. Goddard, C.C. Huang, E.C. Meng, G.S. Couch, T.I. Croll, J.H. Morris, and T.E. Ferrin. 2021. UCSF ChimeraX: Structure visualization for researchers, educators, and developers. *Protein Science*. 30:70-82.

Pleuger, R., C. Cozma, S. Hohoff, C. Denkhaus, A. Dudziak, F. Kaschani, M. Kaiser, A. Musacchio, I.R. Vetter, and S. Westermann. 2024. Microtubule end-on attachment maturation regulates Mps1 association with its kinetochore receptor. *Current Biology*. 34:2279-2293.e2276.

Polley, S., T. Raisch, S. Ghetti, M. Körner, M. Terbeck, F. Gräter, S. Raunser, C. Aponte-Santamaría, I.R. Vetter, and A. Musacchio. 2024. Structure of the human KMN complex and implications for regulation of its assembly. *Nature Structural & Molecular Biology*. 31:861-873.

Przewloka, M.R., Z. Venkei, V.M. Bolanos-Garcia, J. Debski, M. Dadlez, and D.M. Glover. 2011. CENP-C Is a Structural Platform for Kinetochore Assembly. *Current Biology*. 21:399-405.

Punjani, A., J.L. Rubinstein, D.J. Fleet, and M.A. Brubaker. 2017. cryoSPARC: algorithms for rapid unsupervised cryo-EM structure determination. *Nature Methods*. 14:290-296.

Rago, F., K.E. Gascoigne, and I.M. Cheeseman. 2015. Distinct Organization and Regulation of the Outer Kinetochore KMN Network Downstream of CENP-C and CENP-T. *Current Biology*. 25:671-677.

Rieder, C.L., R.W. Cole, A. Khodjakov, and G. Sluder. 1995. The checkpoint delaying anaphase in response to chromosome monoorientation is mediated by an inhibitory signal produced by unattached kinetochores. *The Journal of Cell Biology*. 130:941-948.

Rohou, A., and N. Grigorieff. 2015. CTFFIND4: Fast and accurate defocus estimation from electron micrographs. *Journal of Structural Biology*. 192:216-221.

Roy, B., J. Sim, S.J.Y. Han, and A.P. Joglekar. 2022. Kre28–Spc105 interaction is essential for Spc105 loading at the kinetochore. *Open Biology*. 12.

Scarborough, E.A., T.N. Davis, and C.L. Asbury. 2019. Tight bending of the Ndc80 complex provides intrinsic regulation of its binding to microtubules. *eLife*. 8.

Screpanti, E., A. De Antoni, G.M. Alushin, A. Petrovic, T. Melis, E. Nogales, and A. Musacchio. 2011. Direct Binding of Cenp-C to the Mis12 Complex Joins the Inner and Outer Kinetochore. *Current Biology*. 21:391-398.

Shimogawa, M.M., P.O. Widlund, M. Riffle, M. Ess, and T.N. Davis. 2009. Bir1 Is Required for the Tension Checkpoint. *Molecular Biology of the Cell*. 20:915-923.

Sievers, F., A. Wilm, D. Dineen, T.J. Gibson, K. Karplus, W. Li, R. Lopez, H. McWilliam, M. Remmert, J. Söding, J.D. Thompson, and D.G. Higgins. 2011. Fast, scalable generation of high-quality protein multiple sequence alignments using Clustal Omega. *Molecular Systems Biology*. 7:539.

Stark, H. 2010. GraFix: Stabilization of Fragile Macromolecular Complexes for Single Particle Cryo-EM. *Methods in Enzymology*. 481:109-126.

Takenoshita, Y., M. Hara, R. Nakagawa, M. Ariyoshi, and T. Fukagawa. 2024. Molecular details and phosphoregulation of the CENP-T-Mis12 complex interaction during mitosis in DT40 cells. *iScience*. 27:111295.

Tanaka, K., E. Kitamura, Y. Kitamura, and T.U. Tanaka. 2007. Molecular mechanisms of microtubule-dependent kinetochore transport toward spindle poles. *The Journal of Cell Biology*. 178:269-281.

Tanaka, K., N. Mukae, H. Dewar, M. Van Breugel, E.K. James, A.R. Prescott, C. Antony, and T.U. Tanaka. 2005. Molecular mechanisms of kinetochore capture by spindle microtubules. *Nature*. 434:987-994.

Tanaka, S., M. Miyazawa-Onami, T. Iida, and H. Araki. 2015. iAID: an improved auxin-inducible degron system for the construction of a 'tight' conditional mutant in the budding yeast *Saccharomyces cerevisiae*. *Yeast*. 32:567-581.

Tien, J.F., N.T. Umbreit, D.R. Gestaut, A.D. Franck, J. Cooper, L. Wordeman, T. Gonen, C.L. Asbury, and T.N. Davis. 2010. Cooperation of the Dam1 and Ndc80 kinetochore complexes enhances microtubule coupling and is regulated by aurora B. *Journal of Cell Biology*. 189:713-723.

Tromer, E.C., J.J.E. Van Hooff, G.J.P.L. Kops, and B. Snel. 2019. Mosaic origin of the eukaryotic kinetochore. *Proceedings of the National Academy of Sciences*. 116:12873-12882.

Valverde, R., J. Ingram, and S.C. Harrison. 2016. Conserved Tetramer Junction in the Kinetochore Ndc80 Complex. *Cell Reports*. 17:1915-1922.

Van Hooff, J.J.E., B. Snel, and G.J.P.L. Kops. 2017. Unique Phylogenetic Distributions of the Ska and Dam1 Complexes Support Functional Analogy and Suggest Multiple Parallel Displacements of Ska by Dam1. *Genome Biology and Evolution*. 9:1295-1303.

Walstein, K., A. Petrovic, D. Pan, B. Hagemeier, D. Vogt, I.R. Vetter, and A. Musacchio. 2021. Assembly principles and stoichiometry of a complete human kinetochore module. *Science Advances*. 7:eabg1037.

Wang, H.-W., S. Long, C. Ciferri, S. Westermann, D. Drubin, G. Barnes, and E. Nogales. 2008. Architecture and Flexibility of the Yeast Ndc80 Kinetochore Complex. *Journal of Molecular Biology*. 383:894-903.

Waterhouse, A.M., J.B. Procter, D.M.A. Martin, M. Clamp, and G.J. Barton. 2009. Jalview Version 2—a multiple sequence alignment editor and analysis workbench. *Bioinformatics*. 25:1189-1191.

Wei, R.R., J. Al-Bassam, and S.C. Harrison. 2007. The Ndc80/HEC1 complex is a contact point for kinetochore-microtubule attachment. *Nature Structural & Molecular Biology*. 14:54-59.

Wei, R.R., J.R. Schnell, N.A. Larsen, P.K. Sorger, J.J. Chou, and S.C. Harrison. 2006. Structure of a Central Component of the Yeast Kinetochore: The Spc24p/Spc25p Globular Domain. *Structure*. 14:1003-1009.

Wei, R.R., P.K. Sorger, and S.C. Harrison. 2005. Molecular organization of the Ndc80 complex, an essential kinetochore component. *Proceedings of the National Academy of Sciences*. 102:5363-5367.

Wells, W.A., and A.W. Murray. 1996. Aberrantly segregating centromeres activate the spindle assembly checkpoint in budding yeast. *The Journal of Cell Biology*. 133:75-84.

Westermann, S., I.M. Cheeseman, S. Anderson, J.R. Yates, D.G. Drubin, and G. Barnes. 2003. Architecture of the budding yeast kinetochore reveals a conserved molecular core. *The Journal of Cell Biology*. 163:215-222.

Wigge, P.A., O.N. Jensen, S. Holmes, S. Souès, M. Mann, and J.V. Kilmartin. 1998. Analysis of the *Saccharomyces* Spindle Pole by Matrix-assisted Laser Desorption/Ionization (MALDI) Mass Spectrometry. *The Journal of Cell Biology*. 141:967-977.

Xiao, H., F. Wang, J. Wisniewski, A.K. Shaytan, R. Ghirlando, P.C. Fitzgerald, Y. Huang, D. Wei, S. Li, D. Landsman, A.R. Panchenko, and C. Wu. 2017. Molecular basis of CENP-C association with the CENP-A nucleosome at yeast centromeres. *Genes & Development*. 31:1958-1972.

Yan, K., J. Yang, Z. Zhang, S.H. McLaughlin, L. Chang, D. Fasci, A.E. Ehrenhofer-Murray, A.J.R. Heck, and D. Barford. 2019. Structure of the inner kinetochore CCAN complex assembled onto a centromeric nucleosome. *Nature*. 574:278-282.

Yang, Y., F. Wu, T. Ward, F. Yan, Q. Wu, Z. Wang, T. McGlothen, W. Peng, T. You, M. Sun, T. Cui, R. Hu, Z. Dou, J. Zhu, W. Xie, Z. Rao, X. Ding, and X. Yao. 2008. Phosphorylation of HsMis13 by Aurora B Kinase Is Essential for Assembly of Functional Kinetochore. *Journal of Biological Chemistry*. 283:26726-26736.

Yatskevich, S., K.W. Muir, D. Bellini, Z. Zhang, J. Yang, T. Tischer, M. Predin, T. Dendooven, S.H. McLaughlin, and D. Barford. 2022. Structure of the human inner kinetochore bound to a centromeric CENP-A nucleosome. *Science*. 376:844-852.

Yatskevich, S., J. Yang, D. Bellini, Z. Zhang, and D. Barford. 2024. Structure of the human outer kinetochore KMN network complex. *Nature Structural & Molecular Biology*. 31:874-883.

Zahm, J.A., and S.C. Harrison. 2024. A communication hub for phosphoregulation of kinetochore-microtubule attachment. *Current Biology*. 34:2308-2318.e2306.

Zhang, Z., J. Yang, and D. Barford. 2016. Recombinant expression and reconstitution of multiprotein complexes by the USER cloning method in the insect cell-baculovirus expression system. *Methods*. 95:13-25.

Zheng, S.Q., E. Palovcak, J.-P. Armache, K.A. Verba, Y. Cheng, and D.A. Agard. 2017. MotionCor2: anisotropic correction of beam-induced motion for improved cryo-electron microscopy. *Nature Methods*. 14:331-332.